A Study of Optical and Electronic Properties of Organic Thin Film Transistors Based on Naphthalenetetracarboxylic Diimide Derivatives

Dongxing Yang

A dissertation submitted to the faculty of the University of North Carolina at Chapel Hill in partial fulfillment of the requirements for the degree of Doctor of Philosophy in Curriculum in Applied and Materials Sciences.

Chapel Hill
2006

Approved by:

Advisor: Professor Eugene A. Irene

Reader: Professor Nalin Parikh

Reader: Professor Otto Zhou

Professor Joseph M. DeSimone

Professor Sergei S. Sheiko

Professor John M. Papanikolas

ABSTRACT

Dongxing Yang

A Study of Optical and Electronic Properties of Organic Thin Film Transistors Based on Naphthalenetetracarboxylic Diimide Derivative

(Under the direction of Professor Eugene A. Irene)

The optical properties of spin cast thin films of N,N'-bis(3-phenoxy-3-phenoxy-phenoxy)-1,4,5,8-naphthalene-tetracarboxylic diimide (NDA-n2) and N,N'-bis(3-phenoxy-phenoxy)-1,4,5,8-naphthalene-tetracarboxylic diimide (NDA-n1) were investigated using spectroscopic ellipsometry (SE) complimented by optical absorption spectroscopy in the visible–near UV optical range and atomic force microscopy (AFM) for surface roughness. A combination of Tauc-Lorentzian and Gaussian oscillators model was used to fit the measurements obtained from SE. Film roughness results were also evaluated in the optical model using Bruggman Effective Medium Approximation (BEMA). The effect of different spin deposit conditions including spin speed, concentration of solution and deposition ambient on the NDA's film thickness, surface roughness, optical properties and optical anisotropy have been investigated. No anisotropy has been found for the spin cast film and moderate temperature annealing in high vacuum leads to film densification.

Organic thin film transistors (OTFT's) were fabricated with NDA's as the active semiconductor layer, silicon dioxide (SiO_2) as the gate dielectric, heavily doped silicon as the

substrate, and vacuum evaporated gold lines as the source and drain contacts. The electronic properties were characterized using a custom built probe station. The custom probe station was automated with software program written in LabVIEW™.

NDA's yielded a P-channel device. From transfer characteristic and turn-on plot, the charge mobility was calculated which was in the range of about 10^{-2} cm^2 V^{-1} s^{-1}. Various post fabrication processes were carried out to optimize the device performance. Bottom contact configuration has shown higher charge mobility than top contact in this study. Moderate temperature annealing in high vacuum has improved the device mobility by several orders, yielding evidence for a hopping mechanism for charge transport in NDA's. The high mobility of NDA-n1 compared with NDA-n2 demonstrated that aryl-ether tail group hindered the charge transport in the film. Two alternate gate dielectric layers for the OTFT were also considered; while a non-polar low-K dielectric, polyethylene improved mobility; polar high-K dielectric, copolymer of vinylidene fluoride with trifluoroethylene had an adverse effect on mobility.

ACKNOWLEDGEMENTS

I am eternally grateful to Dr. Eugene Irene for his support, patience, encouragement and insight, which has helped shape the research and my research skills. His valuable feedback contributed greatly to this dissertation. Without him, this dissertation would not have been possible.

I would also like to thank my Student Advisory Committee members, Dr. Otto Zhou, Dr. Nalin Parikh, Dr. Sergei S. Sheiko, Dr. John M. Papanikolas, Dr. Edward T. Samulski, and Dr. Joseph M. DeSimone, who deserve credit or their support and their valuable feedback helped me to improve my dissertation in many different ways.

Past members our research lab, Dr. Ciro Lopez, Dr. Natalya Suvorova, Dr. Alex Mueller, Dr. Jason Brewer, and present members, Dr. Roshan Shrestha, Dr. Li Yan, and Mrs. Yuxiang Li have been helpful and knowledgeable mentors, colleagues, and friends. I am also thankful to them.

My family has made great sacrifices for my education. I am grateful to my wife Ran Jiang and my parents for their blessings and love.

TABLE OF CONTENTS

LIST OF TABLES ---------- x

LIST OF FIGURES ---------- xi

CHAPTERS

1. INTRODUCTION ---------- 1

1.1. Overview ---------- 1

1.2. Organic Thin Film Transistors ---------- 2

1.3. Motivation ---------- 6

1.4. Research Objectives and Strategy ---------- 7

1.5. Overview of Dissertation ---------- 8

1.6. References ---------- 12

2. SPECTRSCOPIC ELLIPSOMETRY ---------- 13

2.1. Introduction ---------- 13

2.2. Polarized Light ---------- 15

2.2.1. The Concept of Polarization ---------- 15

2.2.2. Jones Matrix Representation of Polarized Light ---------- 21

2.3 Hardware for Ellipsometry ---------- 22

2.3.1. Optical Components for an Ellipsometer ---------- 22

2.3.1.1. Light Sources ---------- 22

2.3.1.2. Linear Polarizers ---------- 23

2.3.1.3. Compensators ---------- 27

2.3.1.4. Detectors ---------- 27

2.3.2. Ellipsometry Configurations ---------- 28

2.3.2.1. Null Ellipsometry ---------- 28

2.3.2.2. Rotating Analyzer Ellipsometry ---------- 33

2.4. Optical Modeling ---------- 36

2.4.1. General Procedure for Ellipsometry Measurement ---------- 36

2.4.2. Optical Properties of Solids ---------- 38

2.4.3. Reflection and Refraction at the Interface of Two Isotropic Media ---------- 40

2.4.4. Reflection and Refraction at Multilayer System ---------- 43

2.4.5. Heterogeneous Systems and Effective Medium Approximation 46

2.4.6. Model Optimization ---------- 48

2.5. References ---------- 49

3. ORGANIC SEMICONDUCTORS AND ORGANIC THIN FILM TRANISTORS ---------- 50

3.1. Overview ---------- 50

3.2. Organic Semiconducting Materials ---------- 51

3.3. Charge Transport in Organic Semiconductors ---------- 54

3.4. Instrumentation of Rotating Analyzer Spectroscopic Ellipsometer ------ 57

3.3.1. Band Transport ---------- 56

3.3.2. Hopping Transport ---------- 57

3.3.3. Field-Dependent Transport ---------- 60

3.3.4. Multiple Trapping and Release ---------- 60

3.4. OTFT Operation and Modeling ---------- 63

3.4.1. OTFT Design and Geometry ---------- 63

3.4.2. Principles of Operation ---------- 65

3.4.3. Performance ---------- 70

3.4.4. Electrical Measurements ---------- 71

3.5. References. ---------- 74

4. OPTICAL CHARACTERIZATION ---------- 75

4.1. Introduction ---------- 75

4.2. Experimental Details ---------- 76

4.3. Results and Discussion ---------- 80

4.3.1. Film Preparation ---------- 80

4.3.2. Optical Modeling ---------- 81

4.3.3. Film Roughness ---------- 89

4.3.4. Optical Anisotropy ---------- 92

4.3.5. Optical Properties of NDA-n1 ---------- 95

4.3.6. Optical Properties of PE and P(VDF-TrFE) ---------- 98

4.4. Conclusions ---------- 100

4.5. References ---------- 101

5. CHARACTERIZATION AND OPTIMIZATION OF NDA'S BASED THIN FILM TRANSISTORS ---------- 102

5.1. Introduction ---------- 102
5.2. Experimental Procedures ---------- 104

5.3. Results and Discussions ---------- 109

5.3.1. OTFT with SiO_2 Gate Dielectric Layer ---------- 109

5.3.2. Top-Contact Versus Bottom-Contact OTFT's ---------- 113

5.3.3. Effect of Thermal Annealing ---------- 116

5.3.4. Effect of Gate Dielectric Layer ---------- 121

5.4. Conclusions ---------- 125

5.4. References ---------- 127

6. CONCLUSIONS AND FUTURE DIRECTIONS ---------- 129

6.1. Summary of Results ---------- 129

6.2. Future Directions ---------- 131

LIST OF TABLES

Table 2.1. Changes in Δ and Ψ as film (n = 1.5, k = 0) thickness changes; silicon substrate, He-Ne laser (λ = 632.8 nm), angle of incidence = 70° ---------- 14

Table 4.1. Concentration, spin speed, and POMA film thickness for silicon and SiO_2 substrates ---------- 82

Table 4.2. Comparison of surface energies for silicon, SiO_2, and H-terminated silicon. ---------- 82

Table 4.3. Ψ-Δ from Cauchy model and thickness from Cauchy model and Ψ-Δ trajectory ---------- 88

Table 4.4. Parameters of Tauc-Lorentz oscillator and Gaussian oscillators used for the oscillator model ---------- 88

Table 5.1. Mobilities for NDA's based OTFT with SiO_2 gate dielectric ---------- 110

Table 5.2. Mobilities for NDA-n1 based OTFT with bottom and top contact structure ---------- 113

Table 5.3. Mobilities of NDA-n1 based OTFT with different dielectrics---------- 122

LIST OF FIGURES

Figure 1.1. Schematic structures of (a) N-channel MOSFET, and (b) OTFT. ------- 3

Figure 1.2. N-channel MOSFET in (a) accumulation, (b) depletion, (c) inversion mode, and (d) drain current (I_d) vs. gate voltage (V_g). ---------- 4

Figure 1.3. Molecular structure of (a) Naphthalenetetracarboxylic diimide compounds (used by Katz group) and (b) NDA where n=1, NDA-n1; n=2, NDA-n2. ---------- 9

Figure 2.1. Light wave represented as an electromagnetic transverse plane wave. - 18

Figure 2.2. Plane of incidence in ellipsometry. ---------- 19

Figure 2.3. (a) Elliptically polarized light, (b) linearly polarized light along s-axis, and (c) right-handed circularly polarized light. ---------- 20

Figure 2.4. Total polarization by reflection at the Brewster's angle. ---------- 25

Figure 2.5. Glan-Taylor prism polarizer with total internal reflection of the ordinary component vibration E_o which leaves only the extraordinary component E_e to be transmitted (from reference 5). ---------- 26

Figure 2.6. PCSA null ellipsometry schematic (from reference 7).---------- 29

Figure 2.7. Rotating analyzer ellipsometer (RAE) schematic (from reference 9) --- 34

Figure 2.8. Representation of modeling procedure (courtesy J.A.Woollam)--------- 37

Figure 2.9. Geometry of reflection and refraction when light is incident from medium with refractive index n_1 into a substrate with refractive index n_2. ---------- 39

Figure 2.10. Geometry of reflection and refraction when a monochromatic polarized light is incident between two isotropic media $\tilde{N}_1$ and $\tilde{N}_2$. ---------- 41

Figure 2.11. Geometry of reflection and refraction when a monochromatic polarized light is incident on a film-covered substrate with the complex index of refraction $\tilde{N}_1$, $\tilde{N}_2$ and $\tilde{N}_3$.---------- 44

Figure 3.1. Schematic diagrams of different classes of organic semiconducting materials. (a) molecular crystalline e.g. pentacene at low temperature, (b) molecular amorphous e.g. NDA-N1, (c) conjugated polymer e.g POMA, (d) polymer with pendant active group e.g. PVK polyvinyl carbazole, and (e) molecularly doped polymer e.g. POMA doped with cresol of HCl. ---------- 45

Figure 3.2. Illustration of bonding and anti-bonding orbital interaction of HOMO and LUMO orbitals of a segment of polyethylene molecule. -- 53

Figure 3.3 Examples of some well-known organic semiconducting materials. ----- 55

Figure 3.4. Delocalized charge in a crystal lattice, and charge scattering due to lattice vibration.---------- 59

Figure 3.5. Phonon assisted hopping of charges between localized sites. ---------- 59

Figure 3.6. Schematic illustration of (a) single trap, and (b) multiple traps in organic semiconducting materials.---------- 62

Figure 3.7. Common configurations of OTFT designs with (a) bottom-contact and (b) top-contact designs. ---------- 64

Figure 3.8. Schematic illustration of OTFT operation when applying (a) zero gate voltage, (b) negative gate voltage, and (c) drain voltage together with negative gate voltage. ---------- 66

Figure 3.9. Typical drain-current-voltage characteristic of OTFT's---------- 68

Figure 3.10. Illustration of different regimes during an OTFT operation. (a) linear region, (b) pinch-off region, and (c) saturation.---------- 69

Figure 3.11. Schematic diagram of a vacuum enabled chuck (a) top view of brass plate with 0.5 mm holes drilled, (b) cross-section view of the brass chuck showing 0.5 mm hole and a cavity, and (c) Teflon base bored in the center, an outlet drilled to for vacuum tubing, and an o-ring ensuring the tight fit between the brass top and Teflon base. ---------- 73

Figure 4.1. Flow chart of experimental procedures. ---------- 77

Figure 4.2. UV-Vis Absorption Spectrum of NDA-n2 thin film. ---------- 83

Figure 4.3. Optical properties (*n* and *k*) of NDA-n2 thin film obtained from the Cauchy model in the transparent region along with results from the oscillator model over the entire range ---------- 85

Figure 4.4. Calculated Δ,ψ film thickness trajectory ($\phi = 70^{o}$, 1.96 eV light, $n = 1.72$, $k = 0$ from transparent region of Figure 4) with data (filled squares) from null Ellipsometry ---------- 86

Figure 4.5. Fit of NDA-n2 thin film on single crystal silicon substrate data to the oscillator model for NDA-n2. The inset displays the film structure and thickness obtained from the fit. ---------- 90

Figure 4.6. AFM image of (a) SiO_2 substrate prior deposition, RMS roughness = 0.14 nm, and (b) NDA-n2 thin film, RMS roughness = 0.25 nm ---------- 91

Figure 4.7. NDA-n2 thin film on SiO_2 substrate using oscillator model (a) with and (b) without BEMA layer. The insets display the film structure and thickness obtained from the fit. ---------- 93

Figure 4.8. Schematic of uniaxial anisotropic polymer film: OA is the optic axis, $n_{\perp}$ and $n_{//}$ are the out of plane and in plane refractive indices, respectively. ---------- 94

Figure 4.9. Results of in plane sample rotation at 0°, 60°, 150°. ---------- 94

Figure 4.10. Calculated Ψ-Δ trajectory for NDA-n2 of varying thickness on a Si substrate at multiple angles at 1.96 eV with *n*, *k* values supplied from the oscillator model ---------- 96

Figure 4.11. Optical properties (*n* and *k*) for NDA-n2 at multiple incident angles. The inset displays the film structure and thickness obtained from the fit. ---------- 96

Figure 4.12. UV-Vis spectrum of NDA-n1 and NDA-n2 film on fused quartz substrate. ---------- 97

Figure 4.13. Refractive index (*n* & *k*) of NDA-n1 and NDA-n2 extracted from SE measurement. ---------- 97

Figure 4.14. Extracted optical properties (here refractive index *n*) of (a) PE where extinction coefficient *k* = 0, and

(b) P(VDF-TrFE) where k = 0. ---------- 99

Figure 5.1. Molecular structures of (a) NDA, where n=1, called NDA-n1, n=2, called NDA-n2, (b) polyethylene (PE), and (c) P(VDF-TrFE). ---------- 106

Figure 5.2. (a) Cross section view of the bottom-contact OTFT, (b) cross section view of top-contact OTFT, and (c) top view of gold line patterns used in this study where L is the channel Length 75 μm and W is the channel width 5 mm. ---------- 107

Figure 5.3. Custom built vacuum chamber with *in-situ* ellipsometer for annealing experiments. ---------- 108

Figure 5.4. Transfer characteristics for device with (a) NDA-n2 film, and (b) NDA-n1 film as organic semiconductor layer and SiO_2 as gate dielectric. All measurements were carried out at ambient condition. The data shown are taken in ascending V_G mode with an integration time of 1 s by averaging 5 points. --------- 111

Figure 5.5. Transfer characteristics for device with (a) NDA-n2 film, and (b) NDA-n1 film as organic semiconductor layer and SiO_2 as gate dielectric after 10-6 Torr 60 °C 3 hr annealing. ---------- 112

Figure 5.6. Transfer characteristics for top contact OTFT based on NDA-n1 as organic semiconductor layer and SiO_2 as gate dielectric (a) as-deposit, and (b) after 10^{-6} Torr 80 °C 3 hr annealing. ---------- 115

Figure 5.7. TGA Thermograph of NDA-n1 from 30-300 ºC at 10 ºC/minute. ------- 118

Figure 5.8. Densification of NDA-n1 film on SiO2 substrate under annealing (a) NDA-n1 film thickness obtained from in-situ SE, and (b) NDA-n1 refractive index where solid line is for as-deposit film and dashed line is for annealing at 100 ºC. ---------- 119

Figure 5.9. (a) Transfer and (b) turn on characteristics for NDA-n1 based OTFT using Polyethylene as gate dielectric. All measurements were carried out at ambient condition. The data shown are taken in ascending V_G mode with an integration time of 1 s by averaging 5 points. ---------- 120

Figure 5.10 (a) Transfer and (b) turn on characteristics for NDA-n1 based OTFT using P(VDF-TrFE) as gate dielectric.

All measurements were carried out at ambient condition. The data shown are taken in ascending V_G mode with an integration time of 1 s by averaging 5 points.---------- 123

Figure 5.11 Transfer characteristics for NDA-n1 based OTFT using Polyethylene as gate dielectric after 10^{-6} Torr 80 ºC 3 hr annealing. All measurements were carried out at ambient condition. The data shown are taken in ascending V_G mode with an integration time of 1 s by averaging 5 points---------- 126

CHAPTER 1 – INTRODUCTION

1.1. Overview

Since the invention of transistor by Bardeen, Brattain[1] and Shockley[2] in 1947, the electronic industry has advanced into the era of microelectronics. Under the driving pace of Moore's Law, integrated circuits progressed from the early 1960's "Small-Scale-Integration" to the present "Ultra-Large-Scale-Integration" and inorganic silicon based semiconductors have become the foundation of the industry due to their superior properties and compatibility.[3] However, in recent years there has been growing interest in improving the semiconducting and light emitting properties of organic materials.[4] The high level of interest comes from their potential use for large-area thin-film electronics and low-cost fabrication of devices with acceptable performance.[5] In addition the mechanical flexibility of organic semiconductors makes them more compatible for use with plastic substrates for lightweight and foldable applications.[6]

Compared with traditional inorganic semiconductor devices, organic semiconductor based devices have low charge carrier mobilities. For example, the highest mobility for organic thin film transistors (OTFT's) is in the range of several $cm^2V^{-1}s^{-1}$, which is 3 orders of magnitude lower than crystal Si.[5] Low carrier mobility means sluggish response time and low switching speed, which is not suitable for current high speed logic circuits. However,

OTFT has niches in novel thin film transistor applications requiring structural flexibility, low temperature processing, large area coverage, and lower cost e.g. sensors, low-end smart cards, and radio-frequency identification tags (RFIDs).[4] Ever since 1990 when researchers at Cambridge University demonstrated electroluminescence in poly(*para*-phenylene vinylene) (PPV), organic semiconductors have attracted rapid growth in the application of displays.[7] The global market for organic electronics is set to expand from $650 million in 2005 to $30 billion by 2015, according to a recent report from IDTechEx.

1.2. Organic Thin Film Transistors

It is necessary to mention the structure of metal oxide semiconductor field effect transistors (MOSFET's) before the details of OTFT's are discussed. After the MOSFET's initial introduction in 1950's, research has led to significant decrease in MOSFET size and increase in its performance and complexity that has made the MOSFET the heart of the modern microprocessor. A schematic of an N-channel MOSFET is shown in Figure 1.1a. It is a three-terminal device consisting of source, gate, and drain. In this example, the silicon substrate is P-type doped and possesses positively charged holes as majority charge carriers and electrons as minority carriers. The source and drain are heavily N-type doped (N^+) Si for the high conduction. The voltage applied to the gate controls the charge flows from the source to the drain. A negative gate bias will result in accumulation of holes in the channel region (a condition called "accumulation"), and no current will flow between the source and drain (Figure 1.2a). Upon application of a small positive bias, holes will be depleted from the channel (a condition called "depletion") and electrons will be attracted, however the holes still dominate the minority carriers and no current flows (Figure 1.2b).

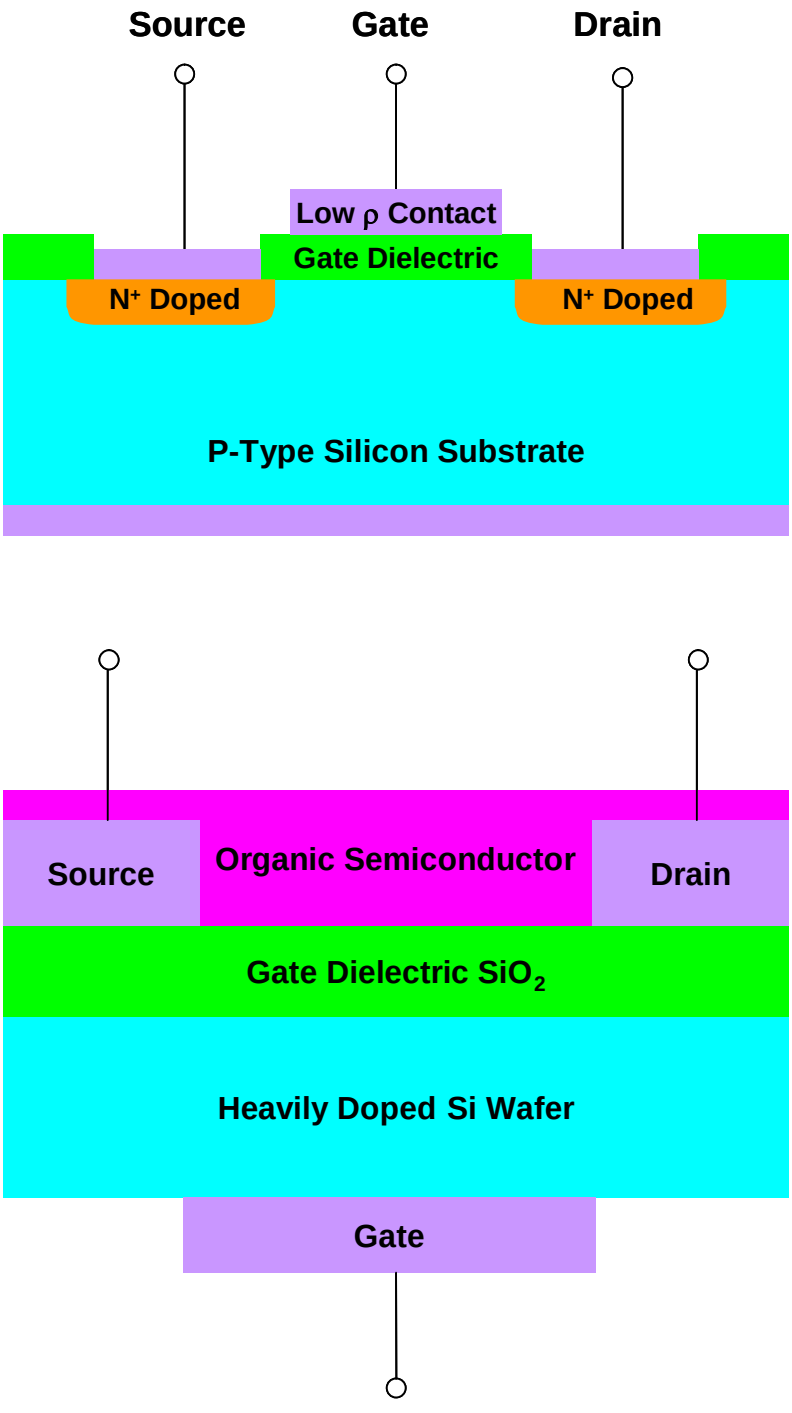

Figure 1.1 Schematic structures of (a) N-channel MOSFET, and (b) OTFT.

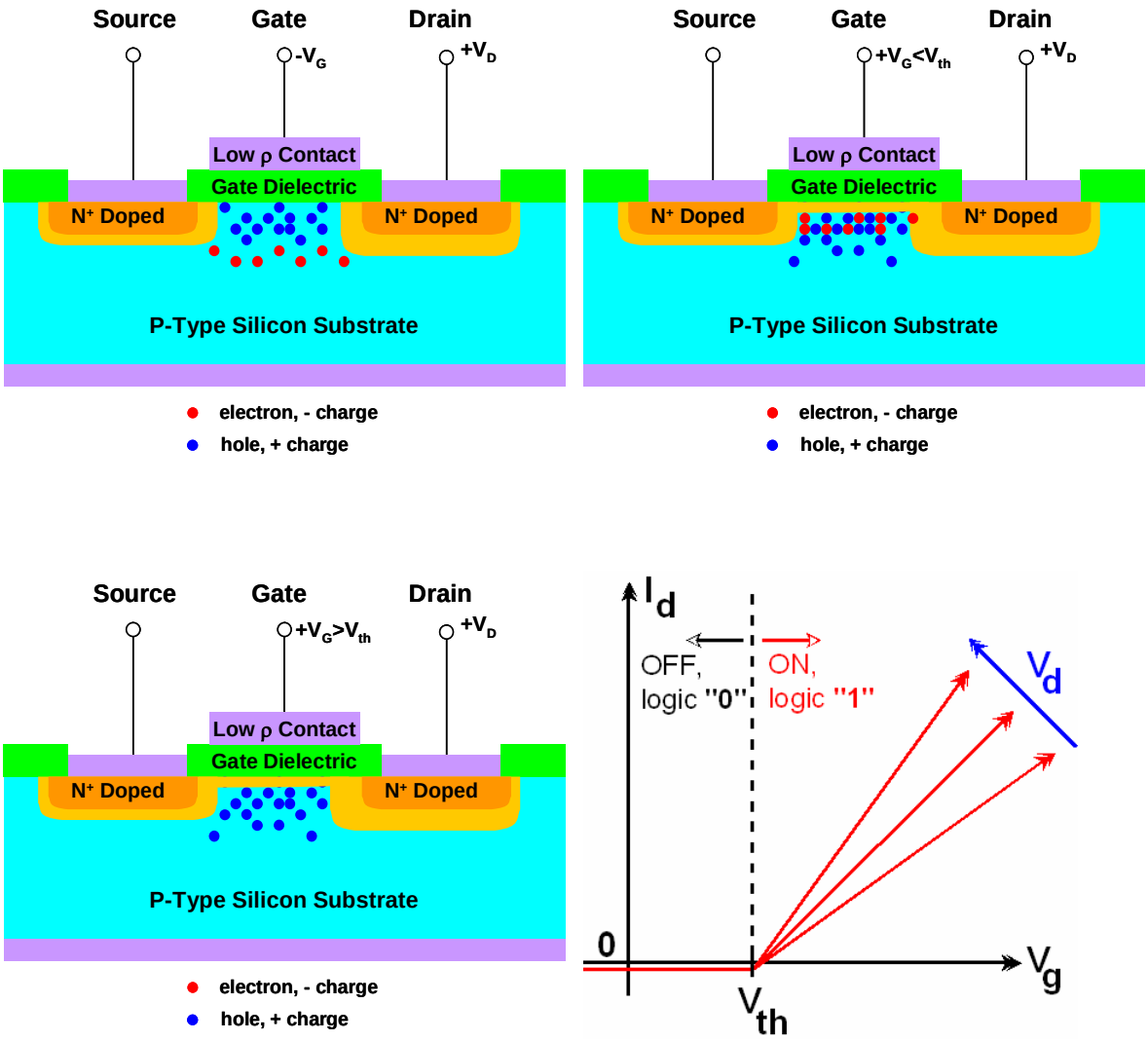

Figure 1.2 N-channel MOSFET in (a) accumulation, (b) depletion, (c) inversion mode, and (d) drain current (I_d) vs. gate voltage (V_g).

Beyond the threshold voltage (V_{th}), carrier inversion will occur and the electrons outnumber the holes allowing current to flow between source and drain (Figure 1.2c) (a condition called "inversion"). Thus, the gate acts as a switch turning the current flow between source and drain OFF (binary logic "0") and ON (binary logic "1"), as shown in Figure 1.2d. In practice, N-channel and P-channel MOSFET's are fabricated in series to create CMOS devices, which are wired to storage capacitors to form dynamic random access memory (DRAM) cells.[8]

The OTFT is also a three-terminal device, composed of gate, source, and drain. Different from the MOSFET, the OTFT is generally constructed with an inverted-gate structure, i.e. gate is at the bottom (Figure 1.1b). Here the heavily doped silicon wafer is used as a convenient conductive substrate and is not part of the active layer. The silicon substrate also provides convenience for the gate oxide/dielectric formation. Another difference between the OTFT and the MOSFET is that the charge carriers that move in an OTFT are majority carriers i.e. it operates in the accumulation mode instead, and there is no inversion mode. Therefore, for a P-channel OTFT, a negative voltage bias is required at the gate to accumulate majority carriers at the interface of the SiO_2 dielectric layer and the semiconductor layer. In this study, OTFT's were fabricated on heavily doped Si substrate, which functioned as the gate contact and thermally oxidized to prepare SiO_2 as gate dielectric layer. Au is deposited in either an interdigited Au array or in parallel lines using a shadow mask. The organic film is then deposited by spin casting from solution.

Semiconducting properties associated with organic materials usually derive from the so-called conjugation, the presence of extended π orbitals formed in carbon containing compounds that show $sp^2 + p_z$ hybridization. The carbon atoms in the backbone bind to three adjacent atoms, two carbons of the backbone and one side group, e.g. a hydrogen. The

fourth electron finds itself in the perpendicular p_z orbital, and the mutual overlap of neighboring p_z electrons causes the formation of π-bands, that consist of the delocalized electrons. The π-bands in the organic semiconductor is normally called Molecular Orbitals. The filled π-band is called the Highest Occupied Molecular Orbital (HOMO), and the empty π-band is called the Lowest Unoccupied Molecular Orbital (LUMO). Some theories that describe the electronic structure and charge transport of conjugated organic semiconductors will be discussed in Chapter 3.

1.3. Motivation

As discussed above, electronic devices based on organic semiconductors offer an attractive alternative to conventional inorganic devices and have already made progress in commercial market. However, only stable organic P-type semiconductors are readily available while practically useful N-type semiconductors have been difficult to develop. Poly(ether-imide)'s (PEI's) are a well-known class of engineering plastics with outstanding mechanical properties, high thermal stability and excellent chemical resistance towards a wide range of solvents. PEI films are used extensively in a variety of electronic applications, i.e. insulating layers, circuit boards and low dielectric constant coatings. Recently, Katz *et al* reported[9] that low molecular weight naphthalenetetracarboxylic diimide derivatives were suitable as stable N-type organic semiconductors even in the presence of air. Their naphthalene based imides with terminal fluorinated tails (Figure 1.3a) showed high electron mobilities (> 0.1 $cm^2V^{-1}s^{-1}$) and excellent on/off current ratios (> 10^5). Based on these results we have selected a compound recently prepared that has the suitable electronic groups indicated by Katz et al but also has groups that should further enhance the compounds stability. The molecular structures are shown in Figure 1.3b. If n is 2, it is called N,N'-

bis(3-phenoxy-3-phenoxy-phenoxy)-1,4,5,8-naphthalene-tetracarboxylic diimide, in short NDA-n2, and if n is 1, it is called N,N'-bis(3-phenoxy-phenoxy)-1,4,5,8-naphthalene-tetracarboxylic diimide or NDA-n1. The compounds show high solubility in various solvents and are suitable candidates for the fabrication of OTFT's.

Interface between the active and the dielectric layers play an important role for device performance and reliability because the operation is based on the control of the charge carriers at the interface. Therefore, it is essential to electronically characterize the interface. To approach this problem, it is also important to understand the optical properties of NDA's and NDA's film-substrate interface. Once the optical properties are determined, film thickness can be extracted using non-destructive techniques that will also aid fabrication process.

1.4. Research Objectives and Strategy

The main objective of this research is to determine, establish and understand the optical and electronic properties of NDA-n1 and NDA-n2 films for their use in OTFT's. Also, the effects of the interface on the device performance are investigated.

Thin films of NDA-n1 and NDA-n2 were prepared from solution using the spin cast technique. The resulting nature of NDA's films due to various spin speed and substrates was examined. In order to obtain the optical properties of NDA's films, UV-Vis spectroscopy and Spectroscopic Ellipsometry (SE) were applied. Once the optical properties of NDA's film were determined, its thickness could be derived and its morphology information could be obtained with the combination of SE and Atomic Force Microscopy (AFM). Then OTFT's based on NDA's were fabricated to test the electronic properties. The performance of an OTFT is gauged by several measures—mainly the electronic mobility and turn on/off

ratio. The electronic mobility, μ is defined as the proportionality coefficient in the dependence of drift velocity on the applied field and describes how easily charge carriers can move within the active layer under the influence of the electric field, while turn on/off ratio is indicative of the switching performance of OTFT's.

Once an understanding between the interface and the opto-electronic properties is developed, improvements or modification of OTFT's devices was investigated in order to optimize device performance. With spin cast NDA's films, there might be residual solvents and disordered molecular arrangements, which would affect the device performance. The devices were then annealed in a high vacuum system and the effects monitored as well as any OTFT improvements. Another major effort was focused on the gate dielectric. High capacitance dielectric is normally desirable as it reduces the operating voltage required to turn the OTFT device on.[10] However, Veres *et al*. have reported improvement in device performance with the use of non-polar low-*K* gate dielectric.[11] In order to resolve this controversy about the choice of low-*K* or high-*K* dielectric for use as gate material in OTFT, polyethylene ($K = 2.3$), and a copolymer of polyvinyledene fluoride copolymer P(VDF-TrFE) ($K = 7.5$) were investigated. These measures will be described in detail in the following chapters.

1.5. Overview of the Dissertation

The dissertation is composed of three sections: background information about the surface analysis techniques, electronic device physics and characterization techniques (Chapters 2 and 3), experimental results and discussions (Chapter 4 and 5), and summary and directions for future study (Chapter 6).

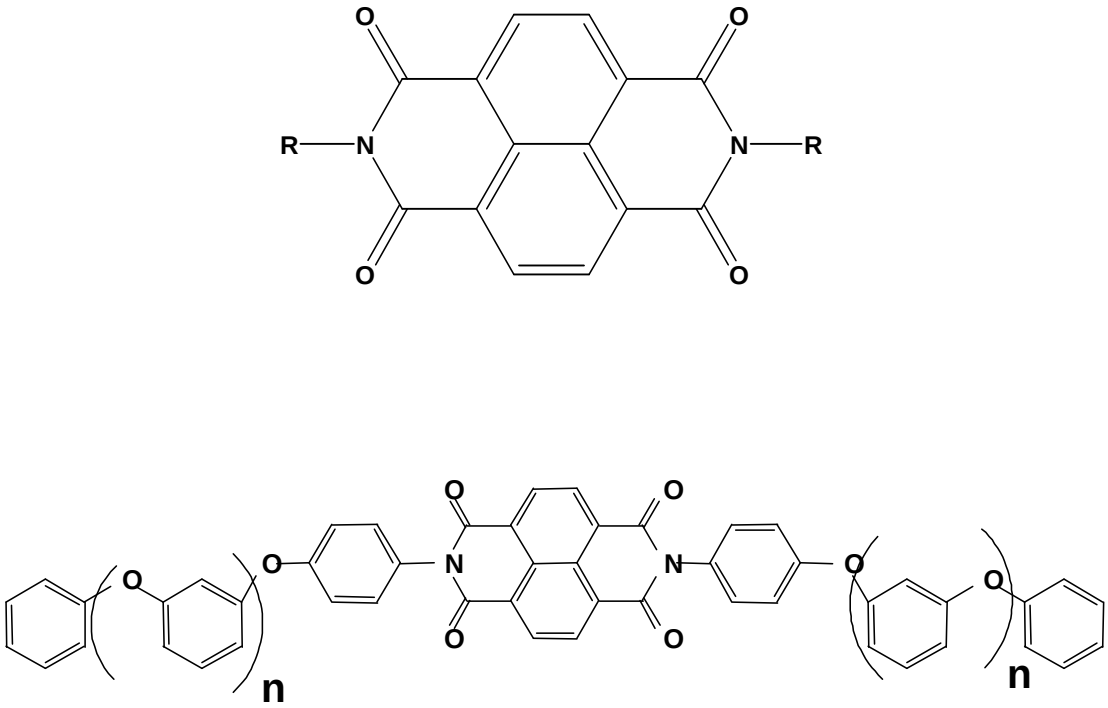

Figure 1.3 Molecular structure of (a) Naphthalenetetracarboxylic diimide compounds (used by Katz group) and (b) NDA where n=1, NDA-n1; n=2, NDA-n2.

Chapter 2 introduces ellipsometry, the technique widely used in this study. We start with the concept of polarized light, and show how the polarization state of light changes when passing through a series of optical elements, from which it is demonstrated what ellipsometry measures and how it makes the measurements. We then explain briefly how physical information about the system under measurement is extracted from the ellipsometric measurements with the construction of an optical model and what information we can get from the ellipsometry measurement, and how physical parameters can be extracted from the modeling of ellipsometry data.

In Chapter 3 the basic principles of charge transport in organic semiconductor based OTFT's are presented. The measurements used to gauge the electrical properties of OTFT's are also mentioned. The configuration of the custom built probe station is discussed. The strategy used for electronic measurements is also briefly introduced in Chapter 2.

Chapters 4 and 5 describe the main results and discussions generated from this research. In Chapter 4, the process used to extract the optical properties of spin-cast NDA's films is discussed in detail. A model WS-400B-6NPP-LITE instrument from Laurell Technologies Corporation was used to spin cast various thicknesses of NDA's films on Si and SiO_2 substrates by varying spin speeds. The custom ellipsometer was the primary instrument used in this study. Complimentary information necessary to build a more comprehensive optical model were also obtained from UV-Vis Spectroscopy, and Atomic Force Microscopy (AFM). In Chapter 5, the electronic characterization and optimization of NDA-OTFT's were presented. The electronic properties mainly the transfer and turn on characteristics were obtained using the custom built probe station. The NDA-OTFT's demonstrated characteristics of P-channel devices, and their positive charge carriers (holes)

mobility was measured to be of the order of 10^{-2} $cm^2V^{-1}s^{-1}$. The finding of the NDA's materials to be P-type is opposite to the Katz group's result. To optimize the device performance, annealing and replacement of SiO_2 gate dielectric are carried out.

Chapter 6 summarizes the results of this work and provides some directions for future research on this subject.

1.6. References

1. J. Bardeen, W.H. Brattain, Phys. Rev., **74**, 230 (1948).

2. W. Shockley, Bell Syst. Tech. J., **28**, 435 (1949).

3. C. Zhao, Ph.D. dissertation, University of North Carolina at Chapel Hill, 1997.

4. G. Horowitz, Adv. Mater., **10** (5), 365 (1998).

5. C.D. Dimitrakopoulos, D.J. Mascaro, IBM J. Res. & Dev., **45** (1), 11 (2001).

6. L.A.A. Pettersson, S. Ghosh, O. Inganas, Organic Electronics **3** (3-4), 143 (2002).

7. N.C. Greenham, RH. Friend, *Semiconductor Device Physics of Conjugated Polymers,* (Academic Press, 1995).

8. S.M. Sze, Physics of Semiconductor Devices, 2nd edition, (John Wiley & Sons, Inc, New York, 1981).

9. H.E. Katz, A.J. Lovinger, J. Johnson, C. Kloc, T. Siegrist, W. Li, Y.-Y. Lin, A. Dodabalapur, Nature, **404**, 478 (2000).

10. L. L. Chua, J. Zaumseil, J.F. Chang, E.C. Ou, P.K.H. Ho, H. Sirringhaus, R.H. Friend, Nature, **434**, 194 (2005).

11. J. Veres, S.D. Ogier, S.W. Leeming, D.C. Cupertino, S.M. Khaffaf, Advan. Func. Mater. **13** (3), 199 (2003).

CHAPTER 2 – SPECTROSCOPIC ELLIPSOMETRY

2.1 Introduction

Ellipsometry is a sensitive measurement technique that uses polarized light to characterize thin films, surfaces, and materials microstructure. It derives its sensitivity from the determination of the relative phase change in a beam of reflected polarized light.[1] The non-invasive, non-destructive nature of ellipsometry allows it to be used as a real-time, *in situ* optical analysis technique. The beginnings of ellipsometry should be credited to Paul Drude (1863-1906) who derived the equations of ellipsometry and made the fist studies on absorbing solids as well as Brewster, Fresnel, and Lord Rayleigh who contributed to the development of ellipsometry with their work on transparent materials.[2]

In general, ellipsometry measures the changes in polarization state of light upon its reflection from the sample. The measured values are expressed as psi (Ψ) and delta (Δ), where Ψ is the relative amplitude change and Δ is the relative phase change introduced by reflection from the surface. When a linearly polarized light of a known orientation is reflected at oblique incidence from a surface, the reflected light is elliptically polarized. The shape and orientation of the ellipse depend on the angle of incidence, the direction of the polarization of the incident light, and the reflection properties of the surface. To obtain the optical and structural information about the sample from the measured Ψ and Δ, an optical

model incorporating known and desired physical properties needs to be constructed based on the previously available knowledge about the sample. The unknown parameters of the model are then determined by regression analysis.

As ellipsometry measures the changes in light intensity not the absolute intensity as is common in other optical analytical techniques, the measurement can be highly accurate and reproducible. A manual, high precision ellipsometer is capable of measuring Δ and Ψ very sensitively, to within ~ 0.02º and ~ 0.01º, respectively.[3] Table 2.1 shows the changes in Δ and Ψ as a film with an index of refraction equal to 1.5 grows on a silicon substrate. For these particular conditions, a high precision, manual ellipsometer would be able to detect the evolution of the film after ~ 0.07 nm by monitoring the change in Δ.

Table 2.1 Changes in Δ and Ψ as film (n = 1.5, k = 0) thickness changes; silicon substrate, He-Ne laser (λ = 632.8 nm), angle of incidence = 70°

Film Thickness (nm)	Δ **(°)**	Ψ **(°)**
0.0	179.257	10.448
0.1	178.957	10.448
0.2	178.657	10.449
0.3	178.356	10.450
0.4	178.056	10.451
0.5	177.756	10.453
1.0	176.257	10.462

Change in Δ / change in film thickness = 3.0°/nm
Change in Ψ / change in film thickness = .014°/nm

The most important application of ellipsometry is to study thin films. In the context of ellipsometry a thin film is one that ranges from essentially zero thickness to several hundred nm, although this range can be extended in some cases. If a film is thin enough that it shows an interference color then it will probably be a good ellipsometric sample.

2.2 Polarized Light

2.2.1 The Concept of Polarization

Light waves are electromagnetic in nature and require four basic field vectors for their complete description: the electric-field strength $\vec{E}$, the electric-displacement density $\vec{D}$, the magnetic-field strength $\vec{H}$, and the magnetic-flux density $\vec{B}$. Of these four vectors, the electric-field strength is chosen to define the state of polarization of light waves. This choice is based on the fact that when light interacts with matter, the force exerted on the electrons by the electric field of the light wave is much greater than the force exerted on these electrons by the magnetic field of the wave.[4,5] Also due to this fact, the interaction of magnetic field with sample is ignored in ellipsometry. In general, once the polarization of $\vec{E}$ has been determined, the polarization of the other three remaining field vectors can be found as the vectors are interrelated by Maxwell's field equations and the associated constitutive/material relations. For time-varying fields, the differential form of Maxwell's equations for a non-conducting, non-dispersive medium is given below

$$\begin{aligned} \vec{\nabla} \bullet \vec{E} &= 0 \\ \vec{\nabla} \bullet \vec{B} &= 0 \\ \vec{\nabla} \times \vec{E} + \frac{1}{c}\frac{\partial \vec{B}}{\partial t} &= 0 \\ \vec{\nabla} \times \vec{B} - \frac{\mu\varepsilon}{c}\frac{\partial \vec{E}}{\partial t} &= 0 \end{aligned} \qquad (2.1)$$

where c is the speed of light, ε is the dielectric function, and μ is the permeability. These equations can be combined and give the solution for the electromagnetic plane wave,

$$\vec{E}(\vec{z},t) = \vec{E}_o \exp\left(\frac{i2\pi\tilde{N}}{\lambda}\vec{k}\cdot\vec{z}\right)\exp(-i\omega t) \qquad (2.2)$$

where $\vec{k}$ is a unit vector along the direction of propagation, $\tilde{N}$ is the complex index of refraction $n+ik$ (to be defined later), λ is the wavelength of the light in vacuum, ω is the angular frequency of the wave, and $\vec{E}_o$ is a complex vector constant specifying the amplitude and polarization state of the wave. Such a wave propagating in a medium with no absorption ($k = 0$) is shown in Figure 2.1. The electric field, magnetic field, and the direction of propagation are all orthogonal with respect to each other. Because of the relationship between the fields, only the E-field and the direction of propagation are required to completely define a plane wave. For a monochromatic transverse electric field, the electric field strength ($\vec{E}$) can be expressed as the vector sum of the components parallel ($\vec{E}_p$) and perpendicular ($\vec{E}_s$) to the plane of incidence, where the plane of incidence is defined for reflection from a surface, and contains the incident light beam and the normal to the sample surface (Figure 2.2):

$$\vec{E} = \vec{i}E_{po}e^{i(\vec{k}z-\omega t+\delta_p)} + \vec{j}E_{so}e^{i(\vec{k}z-\omega t+\delta_s)} \qquad (2.3)$$

where $\vec{i}$ and $\vec{j}$ are unit vectors, and E_{po} and E_{so} are the respective magnitudes. Elliptically polarized light is the most general case and consists of varying amplitudes of the p (E_{po}) and s (E_{so}) components, and encompasses all ranges of phase difference $\delta = \delta_p - \delta_s$, ($-\pi < \delta \le \pi$, $\delta \ne \pi/2, n\pi$) as in Equation 2.3 and Figure 2.3a. Linearly and circularly polarized light can be obtained from Equation 2.3 with the appropriate magnitudes and phase

differences. In general, linearly polarized light can be expressed as Equation 2.4 and shown in Figure 2.3b.

$$\vec{E} = [\vec{i}E_{po} + \vec{j}E_{so}]e^{i(\vec{k}z-\omega t+\delta)} \tag{2.4}$$

where the phase difference of the *p* and *s* components are integral values of π ($\delta \equiv \delta_p - \delta_s = n\pi$). Circularly polarized light consists of *p* and *s* components that are equal in magnitude ($E_o \equiv E_{po} = E_{so}$), but out of phase by $\pi/2$. If the *p* component leads the *s* component by $\pi/2$ (Equation 2.5), then right-handed circularly polarized light is obtained (Figure 2.3c). When the *s* component leads the *p* component by $\pi/2$ (Equation 2.6), left-handed circularly polarized light is obtained.

$$\vec{E} = E_o[\vec{i}e^{i(\vec{k}z-\omega t+\delta_p)} + \vec{j}e^{i(\vec{k}z-\omega t+\delta_p-\frac{\pi}{2})}] \tag{2.5}$$

$$\vec{E} = E_o[\vec{i}e^{i(\vec{k}z-\omega t+\delta_p)} + \vec{j}e^{i(\vec{k}z-\omega t+\delta_p+\frac{\pi}{2})}] \tag{2.6}$$

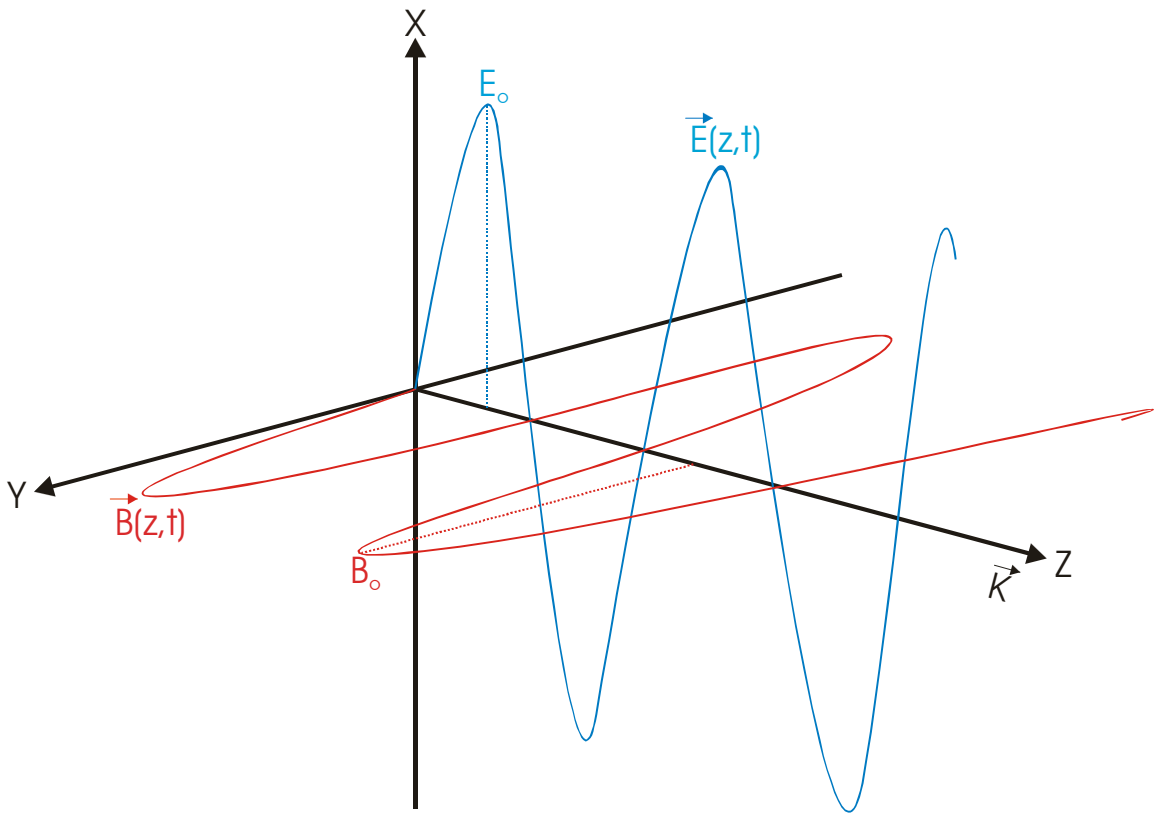

Figure 2.1 Light wave represented as an electromagnetic transverse plane wave

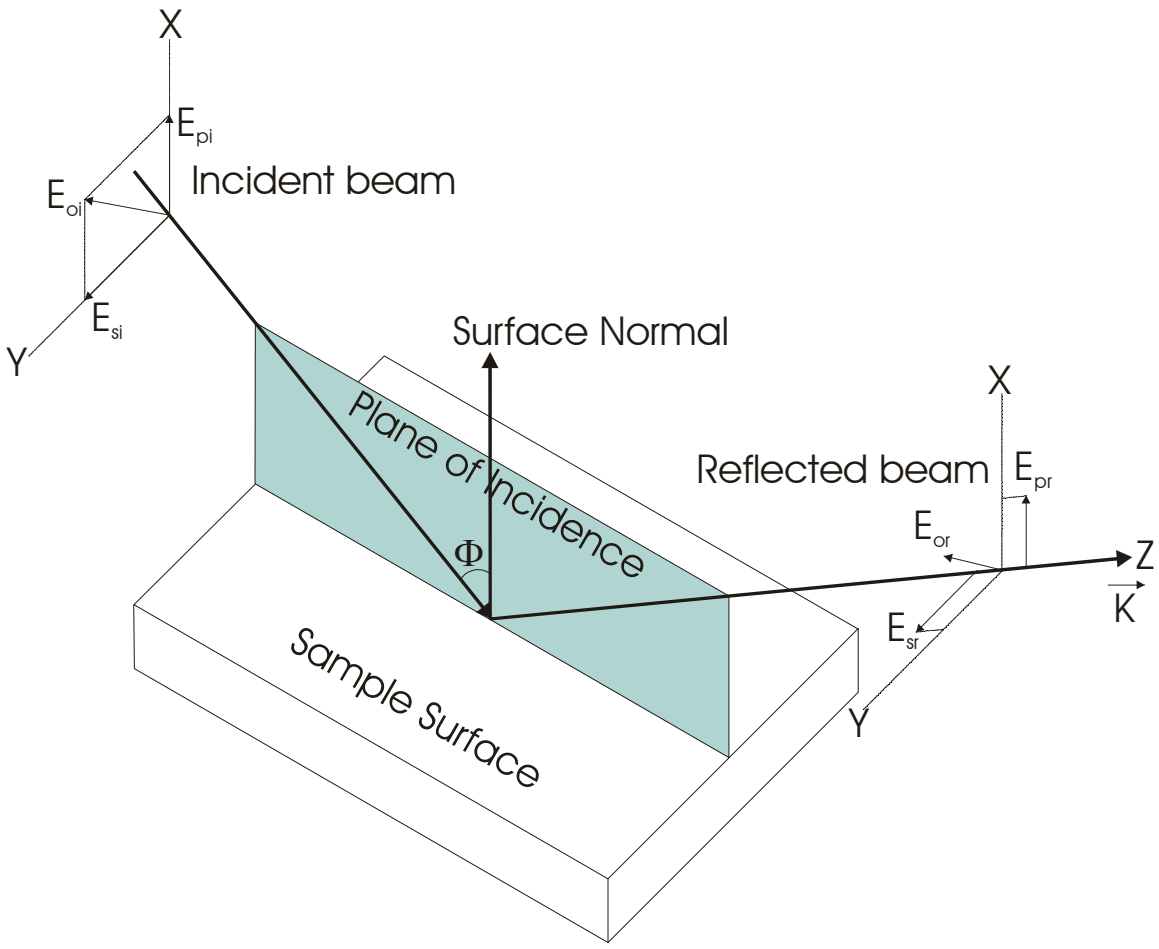

Figure 2.2 Plane of incidence in ellipsometry

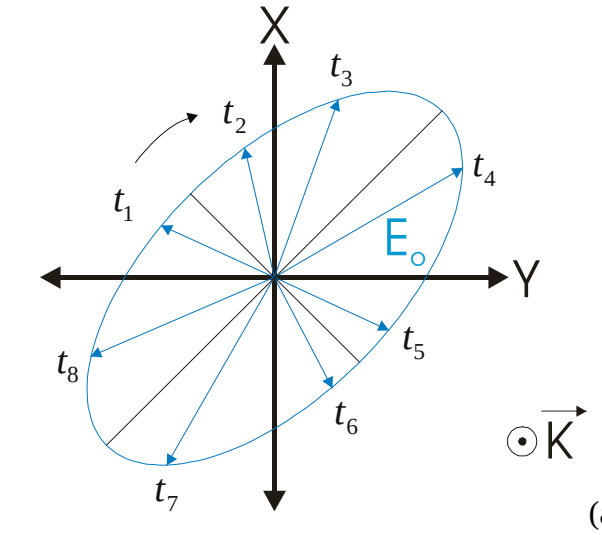

(a)

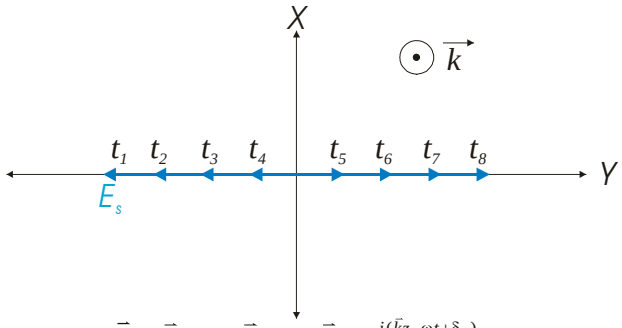

(b)

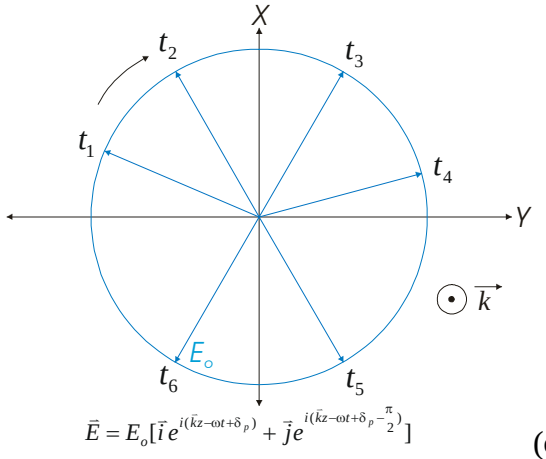

(c)

Figure 2.3 (a) Elliptically polarized light, (b) linearly polarized light along s-axis, and (c) right-handed circularly polarized light.

2.2.2 Jones-Matrix Representation of Polarized Light

Numerous mathematical formulations such as Stokes parameters, Poincare sphere, and complex plane notation have been used to describe a transverse-electric wave. The primary advantage of a mathematical description is that it allows the use of a compact matrix formalism to describe the interaction between light waves and optical devices. Here Jones matrices, a very simplified but adequate for describing polarization states, will be discussed.

As mentioned, the E-field components with space and time dependence can be written as

$$\vec{E} = \vec{i}\,E_{po}e^{i(\vec{k}z-\omega t+\delta_p)} + \vec{j}E_{so}e^{i(\vec{k}z-\omega t+\delta_s)} \tag{2.7}$$

Combining the amplitude and phase information gives

$$\vec{E} = [\vec{i}\,E_{po}e^{i\delta_p} + \vec{j}E_{so}e^{i\delta_s}]e^{i(\vec{k}z-\omega t)} = \tilde{\vec{E}}_o e^{i(\vec{k}z-\omega t)} \tag{2.8}$$

where $\tilde{\vec{E}}_o$ is the complex amplitude. Since the state of polarization of light is completely determined by the relative amplitude and phase of these components, it is only necessary to study the complex amplitude $\tilde{\vec{E}}_o$, which could be written as a two-element matrix or Jones vector.

$$\tilde{\vec{E}}_o = \begin{bmatrix} \tilde{\vec{E}}_p \\ \tilde{\vec{E}}_s \end{bmatrix} = \begin{bmatrix} E_{po}e^{i\delta_p} \\ E_{so}e^{i\delta_s} \end{bmatrix} \tag{2.9}$$

For the special case of *p*- or *s*-polarized light, the normalized Jones vectors have the simple forms, $\begin{bmatrix} 1 \\ 0 \end{bmatrix}$ (*p*-polarized) and $\begin{bmatrix} 0 \\ 1 \end{bmatrix}$ (*s*-polarized), respectively. For the left-circularly

and right-circularly polarized light beam, the normalized Jones vector is $\frac{1}{\sqrt{2}}\begin{bmatrix}1\\ i\end{bmatrix}$ and $\frac{1}{\sqrt{2}}\begin{bmatrix}1\\ -i\end{bmatrix}$, respectively.

Expressing the action of any component or sample upon the polarization state can be done by means of a 2×2 Jones matrix. The diagonal elements of the Jones matrix represent the change of amplitude and phase of the *p*- and *s*-components of the beam, while the off-diagonal elements describe the transfer of energy from the *p*-component to the *s*-component and vice-versa. The Jones matrices for some optical components will be discussed later when discussing ellipsometry instrumentation.

2.3 Hardware for Ellipsometry

2.3.1 Optical Components for an Ellipsometer

An ellipsometer consists of a light source and a detector with polarizer, compensator and analyzer in between, in a specific arrangement that depends on the kind of measurement to be performed.

2.3.1.1 Light Sources

The two most popular light sources for ellipsometer are lasers and arc lamps. A laser typically produces a monochromatic light and is used for a single wavelength ellipsometer. Lasers have the advantage of high output intensity and good collimation. He-Ne laser with 1 mW-output at 632.8 nm has gained widespread usage. For a spectroscopic ellipsometer, a light source with broad spectral and very stable output is needed. Ideally the output should be roughly constant over the necessary spectral range. For this purpose, the Xe or Hg-Xe arc

lamp is generally selected. It can be used from 190 nm in the deep ultraviolet to over 2 μm in the infrared. However, they exhibit low intensity below about 260 nm and have very strong atomic emission lines from about 880 nm to 1010 nm, which can overload the silicon detector used in the ellipsometer. High-pressure arc lamp improves the smoothness of the output spectrum and thus is employed in most current spectroscopic ellipsometry (SE) systems to achieve stable and continuous output light beam.

2.3.1.2 Linear Polarizers

The most important optical element for making ellipsometric measurements is the polarizer. An ideal linear polarizer will transmit light polarized in one direction, but will not transmit any light polarized along the perpendicular direction. When a polarizer is used to resolve the polarization state of reflected light from a sample before the detector, it is usually called an analyzer.

Numerous processes can convert an unpolarized light beam into a polarized light beam. The different physical mechanisms by which one of the two orthogonal resolved components of light could be rejected by a linear polarizer include (1) reflection, (2) dichrioism, and (3) birefringence. If an unpolarized light beam is reflected from a surface at any angles other then 0° or 90°, it will become at least partially polarized since the perpendicular and parallel components of the electric field vector are reflected differently by the surface. If the angle of incidence is such that the reflected and refracted beams are perpendicular to each other, then the reflected beam will be completely polarized (Figure 2.4).[6] This angle of incidence is defined as Brewster's angle (θ_p). Selective absorption is another process that can create polarized light. If unpolarized light travels through a material

in which electric field vectors vibrating in a given plane are transmitted, while electric field vectors vibrating in other directions are absorbed, then the transmitted light will be polarized. Materials of this nature are referred to as dichroic polarizers, an example of which is Polaroid film. Birefringence, or double refraction can create polarized light by the use of prism polarizers. When a light beam is incident from air on a planar face of a transparent uniaxially or biaxially anisotropic crystal, it is, in general, refracted into two beams in the bulk of the crystal. These two beams are spatially separated from one another and are orthogonally linearly polarized. If only one of these two beams is utilized, the double refraction mechanism can be perfectly polarizing. A large variety of polarizers have been built on this principle and Glan-Taylor prism (Figure 2.5) is one of the commonly used birefringent polarizer. It consists of two sections of calcite crystals that are separated by a narrow air gap. The optical axis of two crystals is parallel to each other and to the entrance plane and exit end face of the prism. Light perpendicularly incident on one of the end faces of the prism propagates without refraction to the interface between the two prisms. This light can be resolved into two components E_e (extraordinary) and E_o (ordinary), which are parallel and perpendicular to the optical axis, respectively. Because the two components have different refraction indexes in calcite, the incident angle ϕ at the calcite/gap interface can be adjusted by the prism dimension design, so as to satisfy the conditions that E_o is totally reflected at an incident angle greater than the critical angle, while E_e is highly transmitted by striking the interface at Brewster's angle. The internally reflected light can be absorbed by blackening the interior side of prism, while the other linear polarized light component E_e exits the end face of prism with a slight deviation, but still nearly parallel to the incident beam.

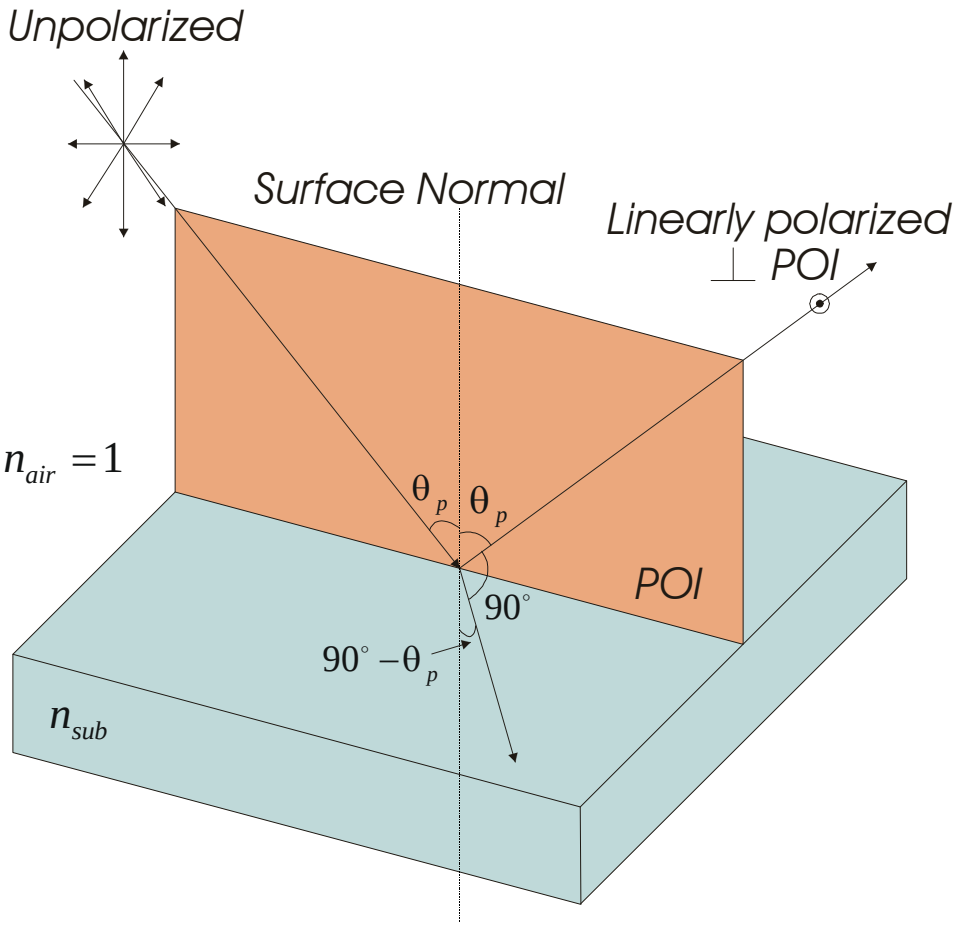

$$n_{air} \sin\theta_p = n_{sub} \sin\left(90^\circ - \theta_p\right)$$

$$n_{sub} = \frac{\sin\theta_p}{\sin\left(90^\circ - \theta_p\right)} = \frac{\sin\theta_p}{\cos\theta_p} = \tan\theta_p$$

$$\theta_p = \tan^{-1}\left(n_{sub}\right) = \text{Brewster's angle}$$

Figure 2.4 Total polarization by reflection at the Brewster's angle.

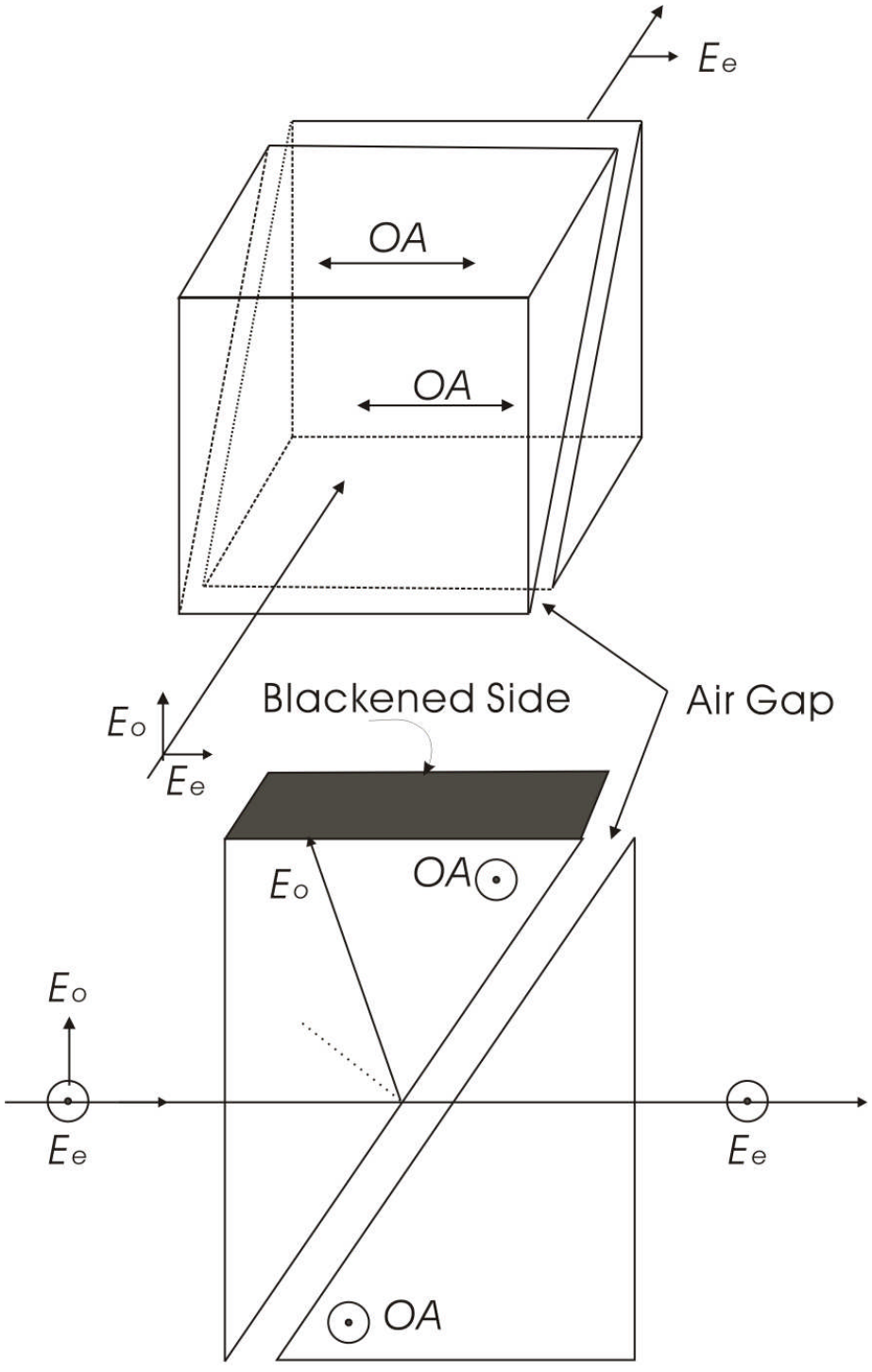

Figure 2.5 Glan-Taylor prism polarizer with total internal reflection of the ordinary component vibration E_o which leaves only the extraordinary component E_e to be transmitted (from reference 5).

2.3.1.3 Compensators

A compensator is also called a retarder which is an optical device that introduces a relative phase shift between two specific orthogonally polarized components into which light incident on the device can be resolved without affecting their relative amplitude. It can be constructed from thin plates of birefringent material or from polished crystal rhombs. Retarders used in ellipsometry are linear retarders that have two optical directions: a fast axis and a slow axis. The component of incident light parallel to the slow axis is retarded in phase relative to the component along the fast axis. When the phase retardation is $\pi/2$, π…, the retarder is called a quarter-wave, half-wave, … retarder. However, the exact retardation of such elements is a strong function of optical alignment and of the light wavelength being used.

2.3.1.4 Detectors

Three types of detectors are commonly used for ellipsometry: photomultiplier tubes (PMTs), semiconductor photodiodes, and charged coupled devices (CCD) arrays. PMT is a versatile device and has been the primary detector for ellipsometry for many years. A typical PMT consists of a photoemissive cathode (photocathode) followed by focusing electrodes, and electron multiplier and an electron collector (anode) in a vacuum tube. When light enters the photocathode, the photocathode emits photoelectrons into the vacuum. These photoelectrons are then directed by the focusing electrode voltages towards the electron multiplier where electrons are multiplied by the process of secondary emission. The multiplied electrons are collected by the anode as an output signal. Because of secondary-emission multiplication, PMTs provide extremely high sensitivity and exceptionally low

noise among the photosensitive devices currently used. The PMT also features fast time response, low noise and a choice of large photosensitive areas. Semiconductor photodiode detectors are semiconductor light sensors that generate a current or voltage when P-N junction in the semiconductor is illuminated by light. These devices feature excellent linearity with respect to incident light, have low internal noise, wide spectral response, are mechanically rugged, compact and lightweight with long life. Among semiconductor photodiode detectors, silicon photodiodes are most commonly used detectors in the UV-Vis range, while InGaAs and HgCdTe detectors are often used for NIR and IR applications. The silicon diode array allows multiple wavelengths to be detected simultaneously rather than sequentially, which increase the data acquisition speed dramatically. The third type of detector is the CCD array, which is an array of light-sensitive elements, or small electronic capacitors. These capacitors are charged by the electrons generated by the input light. The output signal is then connected to an analogue to digital converter and to store into a computer memory, so that its processing will be easy to perform.

2.3.2 Ellipsometer Configurations

All ellipsometer arrangements start with a light source and end with a detector. It is the arrangements of optical components between the source and detector that defines the type of ellipsometer being used.

2.3.2.1 Null Ellipsometry

The null ellipsometer configuration is shown in Figure 2.6[7] and is referred to as PCSA, since the light beam traverses the optical elements in the order: Polarizer,

Compensator, Sample, and Analyzer. The technique is referred to as *null* ellipsometry because the apparatus is adjusted to yield zero intensity after the analyzer. The configurations of the PCSA arrangement that yield zero intensity after the analyzer are then interpreted to yield Δ and Ψ. Since the analyzer is just a linear polarizer, the polarizer and compensator must be adjusted such that the light that is reflected from the sample is linearly polarized, otherwise the reflected light will not be completely extinguished by the analyzer. This is possible since the combination of the polarizer and compensator can yield polarized light of all polarization states. In practice, the compensator is set to 45°, and the polarizer is varied to yield linearly polarized light upon reflection from the sample.

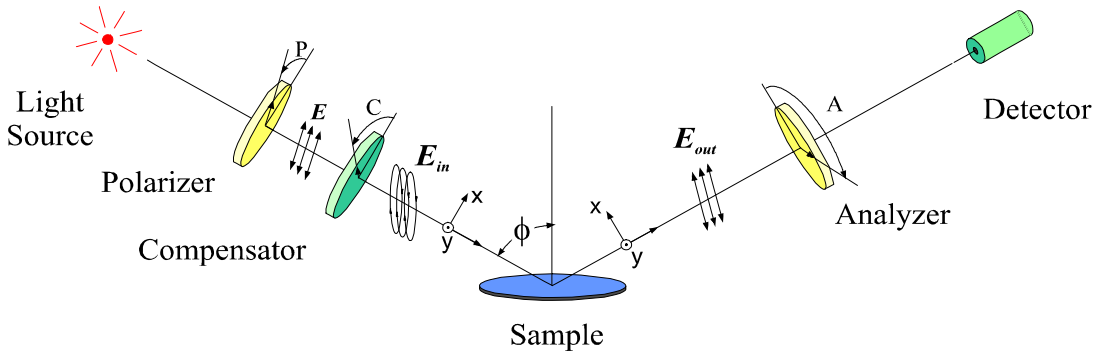

Figure 2.6 PCSA null ellipsometry schematic (from reference 7).

A He-Ne laser (λ = 632.8 nm) is used as the light source for the null ellipsometer in Figure 2.6. The laser beam first passes through the linear polarizer, which only transmits the electric field component that is of the same azimuth as the transmission axis of the polarizer (*P*), as shown in Figure 2.6. The transmission axis azimuth can be rotated from 0° to 360° relative to the plane of incidence. The resulted linearly polarized light can be represented by a Jones vector,[8]

$$\vec{E}_{PO}^{te} = A_c \begin{pmatrix} 1 \\ 0 \end{pmatrix} \tag{2.10}$$

where A_c is the amplitude attenuation constant that determines the light intensity. The subscripts index *PO* refers to the polarizer (*P*) output (*O*), and the superscript *te* refers to the transmission-extinction principal reference system of the polarizer. The linearly polarized light then passes through the compensator set to 45° relative to the plane of incidence. However, the fast-slow (*fs*) axis of the compensator in general is not aligned with that of the polarizer. Hence a rotation of coordinate system from *te* of the polarizer to *fs* of the compensator is necessary. This can be accomplished by multiplying a coordinate rotation matrix $R(\alpha)$ where α is the angle of rotation from the old system to the new one as,

$$R(\alpha) = \begin{pmatrix} \cos\alpha & \sin\alpha \\ -\sin\alpha & \cos\alpha \end{pmatrix} \tag{2.11}$$

The input wave for the compensator after rotation is then,

$$E_{CI}^{fs} = R(P-C)E_{PO}^{te} = A_c \begin{pmatrix} \cos(P-C) \\ \sin(P-C) \end{pmatrix} \tag{2.12}$$

where *P* and *C* are the azimuth angles of the polarizer and compensator, respectively. Then we can obtain the output of compensator by applying the Jones matrix, T_C^{fs}, for the compensator (Equation 2.13) to the input wave (Equation 2.14).

$$T_C^{fs} = K_C \begin{pmatrix} 1 & 0 \\ 0 & \upsilon_c \end{pmatrix}, \qquad \rho_c = T_c e^{i\delta_c} \tag{2.13}$$

$$E_{CO}^{fs} = T_C^{fs} E_{CI}^{fs} = K_C A_c \begin{pmatrix} \cos(P-C) \\ \rho_c \sin(P-C) \end{pmatrix} \tag{2.14}$$

where K_C is a constant that accounts for the common attenuation and phase shift along both the fast and slow axes of the compensator, ρ_c is the relative retardation of the compensator, T_C is the attenuated amplitude along the slow axis, and δ_C is the retarded phase. It can be seen from Equation 2.14 that light exiting the compensator is in general elliptically polarized as opposed to the linear input before the compensator, and by changing the azimuths angles of the polarizer and the compensator, all possible polarization states can be obtained. The output of the compensator then becomes the input to the sample surface, which has an *x-y* reference system, so another rotation from the *fs* system of compensator to the *x-y* system of sample is needed,

$$E_{SI}^{xy} = E_{CO}^{xy} = R(-C)E_{CO}^{fs} \tag{2.15}$$

The light will then interact with the sample under measurement, and at least part of the light will be reflected back from the sample surface. The effect of the reflection from samples surface can be expressed by a Jones matrix R_S^{xy}, as follows:

$$E_{SO}^{xy} = R_S^{xy} S_{SI}^{xy}, \quad where \quad R_S^{xy} = \begin{pmatrix} R_p & 0 \\ 0 & R_s \end{pmatrix} \tag{2.16}$$

where R_p and R_s are the reflection coefficients for the *p* and *s* components of the light wave, which are the ratios of overall reflected wave amplitudes to the incident wave amplitudes in the *p* and *s* directions, respectively, and can be derived from the Fresnel equations with known angle of incidence and refractive indices of the media involved (discussed later). The final optical element the light interacts with before reaching the photodetector is the analyzer, which is also a linear polarizer and thus has a *t-e* reference frame. The light reflected from the sample surface therefore needs to be rotated to this *t-e* reference frame (from the *x-y* system of the sample) before considering the effects of the element on the light,

$$E_{AI}^{te} = E_{SO}^{te} = R(A)E_{SO}^{xy} \tag{2.17}$$

where A is the azimuth angle of the analyzer similarly defined in the same way as P for the polarizer. The output wave from the analyzer can thus be obtained by applying the Jones matrix that is characteristic of an analyzer.

$$E_{AO}^{te} = T_A^{te} E_{AI}^{te}, \quad where \quad T_A^{te} = K_A \begin{pmatrix} 1 & 0 \\ 0 & 0 \end{pmatrix} \tag{2.18}$$

in which K_A is the attenuation constant for analyzer. To Sum it up, the wave vector that reaches the photodetector can be expressed as follows,

$$E_{AO}^{te} = T_A^{te} R(A) T_S^{xy} R(-C) T_C^{fs} R(P-C) A_c \begin{pmatrix} 1 \\ 0 \end{pmatrix} = K \begin{pmatrix} E_t \\ 0 \end{pmatrix} \tag{2.19}$$

where
$$K = K_A K_C K_P \tag{2.20}$$

and
$$\begin{aligned} E_t = {} & R_p \cos A\left[\cos C \cos(P-C) - \rho_c \sin C \sin(P-C)\right] \\ & + R_s \sin A\left[\sin A \cos(P-C) + \rho_c \cos C \sin(P-C)\right] \end{aligned} \tag{2.21}$$

Finally, the intensity of the light collected by the photodetector is,

$$I = \left| E_{AO}^{te} \right|^2 \tag{2.22}$$

This is a function of P, C, A, ρ_c, R_p, and R_s. For a null ellipsometry system, usually a quarter wave plate is chosen as the compensator, so ρ_c is known. During measurements, P, C, and A are arranged so that the light intensity detected by the photodetector becomes zero (null), which means $E_t = 0$. With this condition, we can obtain from Equation 2.21 the following relationship:

$$\rho \equiv \frac{R_p}{R_s} = -\tan A \left[\frac{\tan C + \rho_c \tan(P-C)}{1 - \rho_c \tan C \tan(P-C)} \right] \tag{2.23}$$

where ρ is called the complex reflection coefficient of the sample. The two complex amplitude reflection coefficients (R_p and R_s) can be written as:

$$R_p = |R_p| e^{i\delta_p}$$
$$R_s = |R_s| e^{i\delta_s} \tag{2.24}$$

With equation 2.24, the complex reflection coefficient can be written in the following form:

$$\rho \equiv \tan\Psi e^{i\Delta} \tag{2.25}$$

in which,

$$\Delta = \delta_p - \delta_s$$
$$\tan\Psi = \frac{|R_p|}{|R_s|} \tag{2.26}$$

The complex reflection coefficient, ρ , and the extraction of materials properties from Δ and Ψ will be discussed in next section.

2.3.2.2 Rotating Analyzer Ellipsometry

A schematic of the rotating analyzer ellipsometer used in this research is shown in Figure 2.7.[9] The set-up is similar to the null ellipsometer, except that there is no compensator and the analyzer is constantly rotated. In addition, rotating analyzer ellipsometry (RAE) does not make use of the null condition, rather the periodic intensity at the detector is used to extract Δ and Ψ . The light source is a Xenon Arc lamp powered at 70 watts, which produces unpolarized, white light over the range of 250-750 nm. This white light then passes through a calcite Glan-Taylor polarizing prism, which results in linearly polarized white light. Typically, the polarizer is set to 20° since this setting has proven to be the most sensitive for our samples.

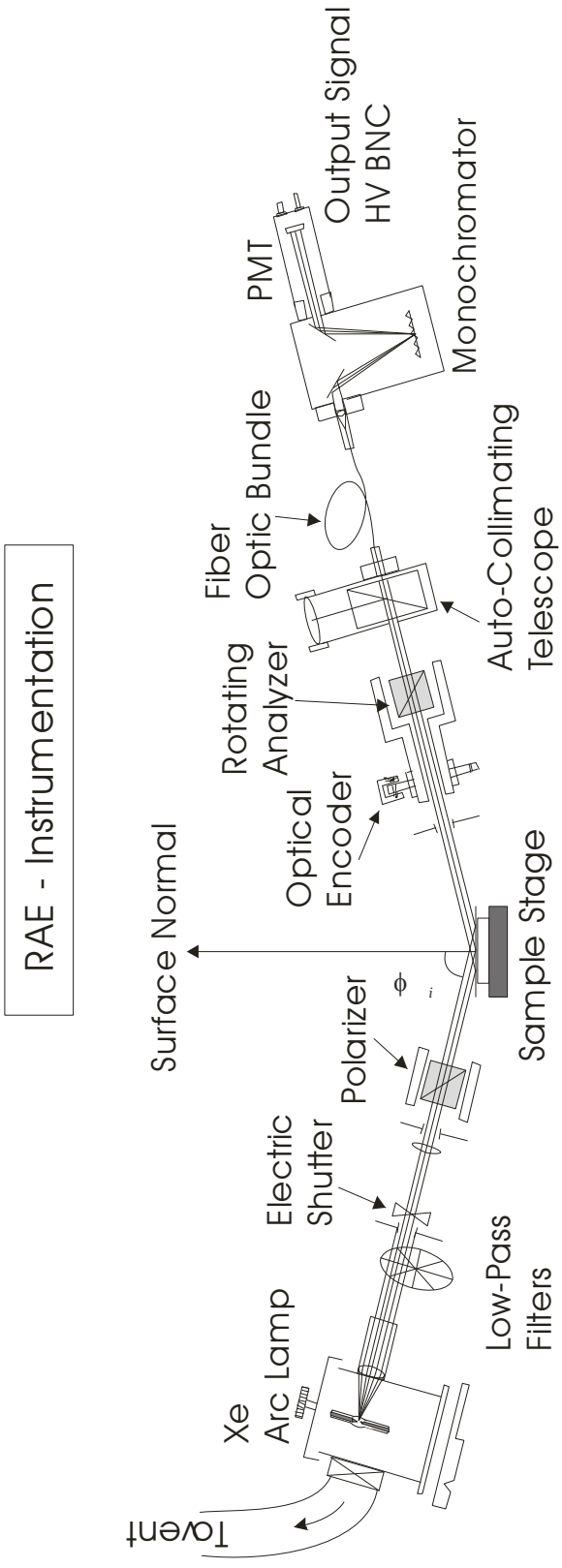

Figure 2.7 Rotating analyzer ellipsometer (RAE) schematic (from reference 9)

Next, the linearly polarized light is reflected from the sample at the chosen angle of incidence (ϕ_i, typically 70°) and enters the rotating analyzer, which is a linear polarizer. The electric field vector of the light entering the photodetecting device can be expressed similar to that for null ellipsometry discussed in the previous section:

E_{PMT} = [Analyzer][Sample][Polarizer][Input Beam]

$$E_{PMT} = E_o \begin{pmatrix} 1 & 0 \\ 0 & 0 \end{pmatrix} \begin{pmatrix} \cos A & \sin A \\ -\sin A & \cos A \end{pmatrix} \begin{pmatrix} R_p & 0 \\ 0 & R_s \end{pmatrix} \begin{pmatrix} \cos P & \sin P \\ -\sin P & \cos P \end{pmatrix} \begin{pmatrix} 1 \\ 0 \end{pmatrix} \quad (2.27)$$

where E_o is a constant. The azimuth of the rotating analyzer rotates at a frequency, ω, such that the analyzer azimuth (A) at a given time (t) is obtained from Equation 2.28.

$$A(t) = 2\pi\omega t + \delta \quad (2.28)$$

where δ is a phase constant. Equation 2.27 can be simplified as:

$$E_{PMT} = E_o (R_p \cos A \cos P + R_s \sin A \sin P) \begin{pmatrix} \cos A \\ \sin A \end{pmatrix} \quad (2.29)$$

Since the light intensity detected by PMT is $I = |E_{PMT}|^2$, by applying Equations 2.24 and 2.26, this intensity can be expressed as

$$I_d = I_o[1 + (\frac{\tan^2\Psi - \tan^2 P}{\tan^2\Psi + \tan^2 P})\cos(2A(t)) + (\frac{2\tan\Psi\cos\Delta\tan P}{\tan^2\Psi + \tan^2 P})\sin(2A(t))] \quad (2.30)$$

or

$$I_d = I_o[1 + \alpha\cos(2A(t)) + \beta\sin(2A(t))] \quad (2.31)$$

With the analyzer angle, A, being a periodic function of time, Fourier analysis can be used to determine the Fourier coefficients α and β. Solving for $\tan\Psi$ and $\cos\Delta$ from the above equation we get

$$\tan\Psi = \tan P\left(\frac{1+\alpha}{1-\alpha}\right)^{1/2} \tag{2.32}$$

$$\cos\Delta = \frac{\beta}{(1-\alpha^2)^{1/2}} \tag{2.33}$$

Therefore Fourier analysis of the detector signal will yield the Fourier coefficients α and β which can then be used to calculate Ψ and Δ. Once Ψ and Δ are determined an optical model must be constructed to calculate the desired unknown parameters.

2.4 Optical Modeling

2.4.1 General Procedure for Ellipsometry Measurement

As already discussed, ellipsometry measures Δ and Ψ, the respective changes in phase and amplitude of monochromatic polarized light as it is reflected from the sample. It is then necessary to solve the inverse problem of modeling the measured data to estimate the values of the sample parameters that yield data predicted from the model which best match the measured data. The procedure can be divided into four steps, as illustrated in Figure 2.8. After the experimental measurement, we need to construct a model from which we can accurately predict what we should measure from a sample of known properties. This model will contain the known parameters, such as the wavelength of the incident light, the incident beam polarization sate, and the angle of incidence. It will also contain some unknown physical parameters, such as layer thickness and optical constants. After a model is developed, we can vary the unknown physical parameters and generate data until a set of optimized parameters that yield calculated data that closely match our measured optical data.

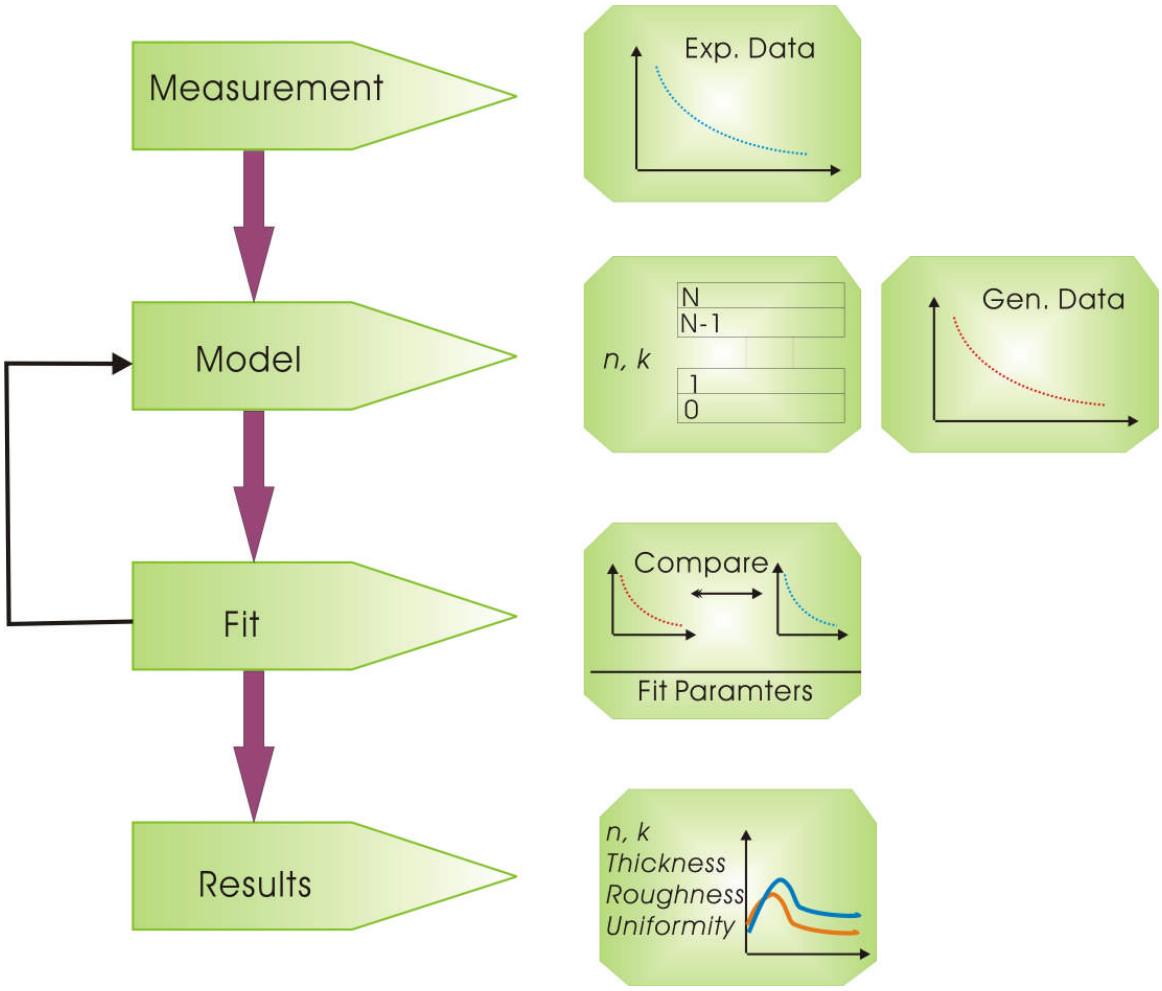

Figure 2.8 Representation of modeling procedure (courtesy J.A.Woollam)

Having found a set of physical parameters yielding calculated data which closely match the experimental optical data, we must now establish that the best-fit set of parameters is unique, physically reasonable, and not strongly correlated. It these criteria are met, we can conclude that the best-fit model probably represents the physical reality of the sample. We may also calculate a number of statistical quantities that help to evaluate the accuracy and precision of the fit results.

2.4.2 Optical Properties of Solids

When a light beam arrives at a smooth flat interface between two media, part of the wave will be reflected and part will be transmitted. The angle of reflection from the surface will be equal to the angle of incidence, while the transmitted light wave obeys the Snell's law.

$$n_1 \sin\phi_1 = n_2 \sin\phi_2 \tag{2.34}$$

where ϕ_1 is the angle of incidence and ϕ_2 is the refracted angle (see Figure 2.9). The velocity of transmitted light will undergo a change that depends on the change in permittivity (ε) and permeability (μ) of the media. The ratio of the speed of light within the media to that of it in free space is referred to as the index of refraction, *n*.

$$n = \frac{c}{v} = \sqrt{\frac{\varepsilon\mu}{\varepsilon_o \mu_o}} \tag{2.35}$$

where ε_0 and μ_0 are the permittivity and permeability of free space. The complex index of refraction can be defined as

$$\tilde{\mathrm{N}} = \mathrm{n} - \mathrm{ik} \tag{2.36}$$

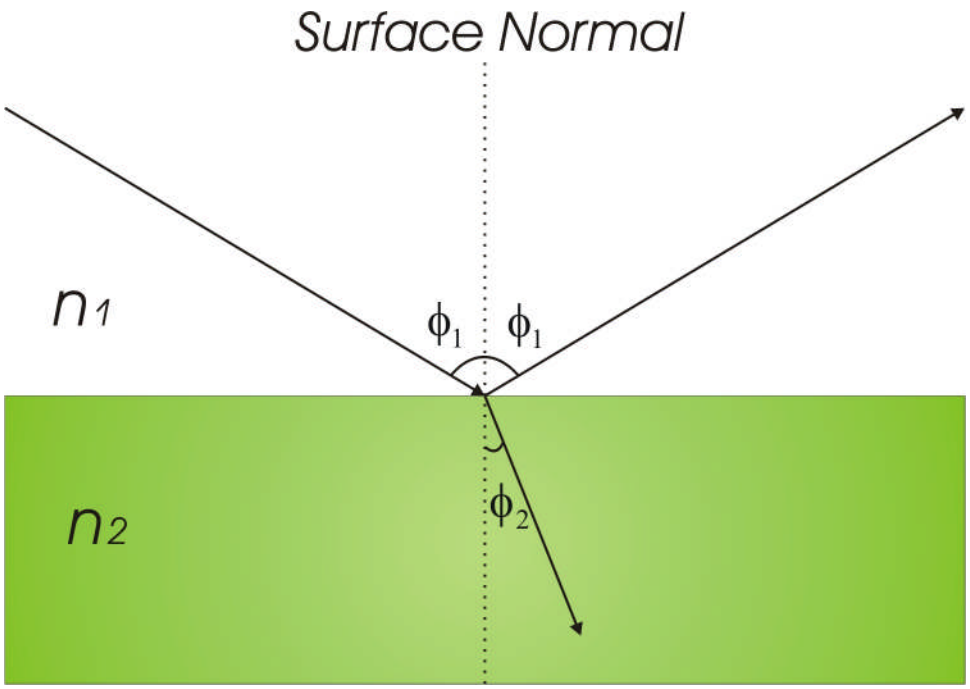

Figure 2.9 Geometry of reflection and refraction when light is incident from medium with refractive index n_1 into a substrate with refractive index n_2.

If the imaginary part of the complex index is non-zero, the amplitude of the wave will decay exponentially as it propagates.

$$E \propto \exp\left(-\frac{2\pi kz}{\lambda}\right) \tag{2.37}$$

where *k* is the extinction coefficient. This extinction coefficient expresses the degree of damping as it propagates in the z-direction. This wave will decay to $1/e$ (36.7%) of its original amplitude after it propagates a distance D_p known as the penetration depth given by:[10]

$$D_p = \frac{\lambda}{2\pi k} \tag{2.38}$$

The dielectric function of a material is comprised of both the index of refraction and extinction coefficient by the expression,

$$\varepsilon = \tilde{N}^2 = (n - ik)^2 = n^2 - i2nk - k^2 \tag{2.39}$$

If the dielectric function is separated into real and complex components then

$$\begin{aligned} \varepsilon &= \varepsilon_1 - i\varepsilon_2 \\ \varepsilon_1 &= n^2 - k^2 \\ \varepsilon_2 &= 2nk \end{aligned} \tag{2.40}$$

Though *n* and *k* are usually referred to as optical constants, however this is somewhat misleading since *n* and *k* are dispersive, as well as being temperature dependent.

2.4.3 Reflection and Refraction at the Interface of Two Isotropic Media

Figure 2.10 depicts the reflection and refraction of a monochromatic polarized light upon interaction with the bare surface of a homogeneous material.

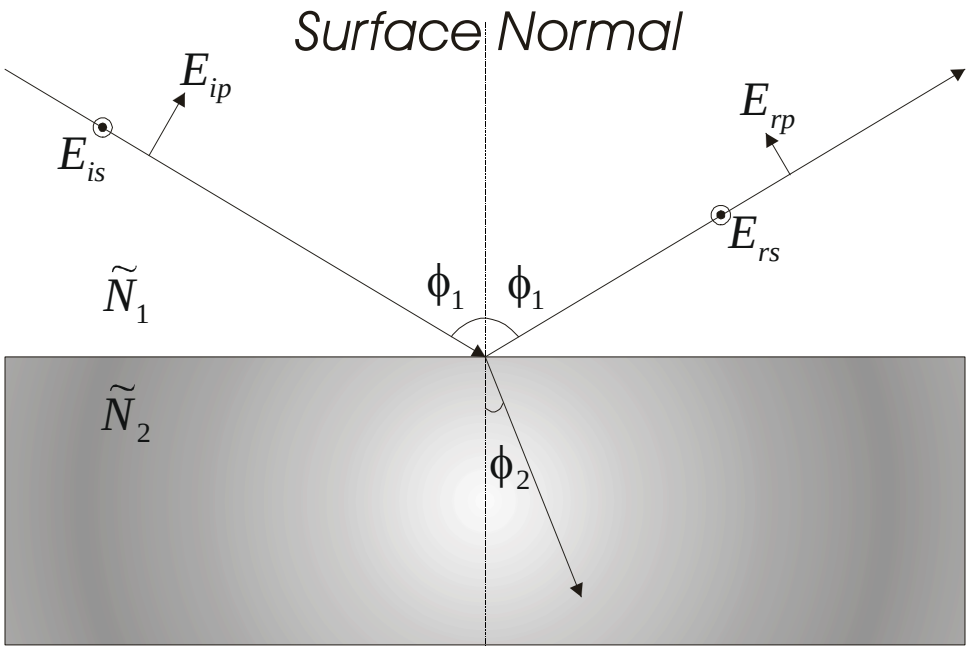

Figure 2.10 Geometry of reflection and refraction when a monochromatic polarized light is incident between two isotropic media $\tilde{N}_1$ and $\tilde{N}_2$.

The angle of incidence is represented by ϕ_1 (as is the angle of reflection), while the angle of refraction is ϕ_2. The behavior of light at the interface of a medium, and within the medium, is determined by the complex index of refraction ($\tilde{N}$) of the medium. Dielectrics are non-absorbing and thus $k = 0$, dielectrics are also referred to as transparent materials for this reason. Snell's law relates the angles of reflection and refraction to the complex indices of refraction as written in Equation 2.41.

$$\tilde{N}_1 \sin\phi_1 = \tilde{N}_2 \sin\phi_2 \tag{2.41}$$

For dielectrics ($k = 0$), Snell's law reduces to Equation 2.42.

$$n_1 \sin\phi_1 = n_2 \sin\phi_2 \tag{2.42}$$

The amplitude of the reflected wave (E_r) in Figure 2.10 is related to the incident wave (E_i) via the Fresnel reflection coefficient. As shown in Equations 2.43 and 2.44, the Fresnel reflection coefficient is different for the *p* and *s* components as indicated by the superscripts.

$$r_{12}^{p} = \frac{E_{rp}}{E_{ip}} = \frac{\tilde{N}_2 \cos\phi_1 - \tilde{N}_1 \cos\phi_2}{\tilde{N}_2 \cos\phi_1 + \tilde{N}_1 \cos\phi_2} \tag{2.43}$$

$$r_{12}^{s} = \frac{E_{rs}}{E_{is}} = \frac{\tilde{N}_1 \cos\phi_1 - \tilde{N}_2 \cos\phi_2}{\tilde{N}_1 \cos\phi_1 + \tilde{N}_2 \cos\phi_2} \tag{2.44}$$

The numbered subscripts denote the medium of origin from Figure 2.10. The complex reflection coefficient (ρ) is then calculated from the Fresnel reflection coefficients as in Equation 2.45.

$$\rho = \frac{r_{12}^{p}}{r_{12}^{s}} = \frac{\left(\dfrac{\tilde{N}_2 \cos\phi_1 - \tilde{N}_1 \cos\phi_2}{\tilde{N}_2 \cos\phi_1 + \tilde{N}_1 \cos\phi_2}\right)}{\left(\dfrac{\tilde{N}_1 \cos\phi_1 - \tilde{N}_2 \cos\phi_2}{\tilde{N}_1 \cos\phi_1 + \tilde{N}_2 \cos\phi_2}\right)} \tag{2.45}$$

As discussed in section 2.3.2, ρ is also related to Δ and Ψ, Equation 2.45 can be expanded as shown in Equation 2.46.

$$\rho = \frac{r_{12}^{p}}{r_{12}^{s}} = \tan\Psi e^{i\Delta} = \rho\left(\tilde{N}_1, \tilde{N}_2, \phi_1, \lambda\right) \tag{2.46}$$

Equation 2.46 is the fundamental equation of ellipsometry, since it relates the two experimental measurable values (Δ and Ψ) to the properties of the material ($\tilde{N}_1, \tilde{N}_2$) being studied. The complex reflection coefficient is also related to $\hat{\varepsilon}$ as in Equation 2.47.

$$\hat{\varepsilon} = \sin^2\phi_1 + \sin^2\phi_1 \tan^2\phi_1 \left(\frac{1-\rho}{1+\rho}\right)^2 \tag{2.47}$$

2.4.4 Reflection and Refraction at Multilayer System

It will be more complex when the sample consists of a substrate with one or more films. This creates multiple interfaces where reflection and refraction take place as depicted in Figure 2.11. The Fresnel reflection coefficient (*r*) is replaced by the total reflection coefficient (*R*). Equations 2.48 and 2.49 define the total reflection coefficients for the *p* and *s* components, respectively,

$$R^{p} = \frac{r_{12}^{p} + r_{23}^{p} e^{-i2\beta}}{1 + r_{12}^{p} r_{23}^{p} e^{-i2\beta}} \tag{2.48}$$

$$R^{s} = \frac{r_{12}^{s} + r_{23}^{s} e^{-i2\beta}}{1 + r_{12}^{s} r_{23}^{s} e^{-i2\beta}} \tag{2.49}$$

where the exponential term, β, is a measure of the phase shift due to the different path lengths of the reflected and refracted beams.

$$\beta = 2\pi\left(\frac{L}{\lambda}\right)\tilde{N}_2 \cos\phi_2 \tag{2.50}$$

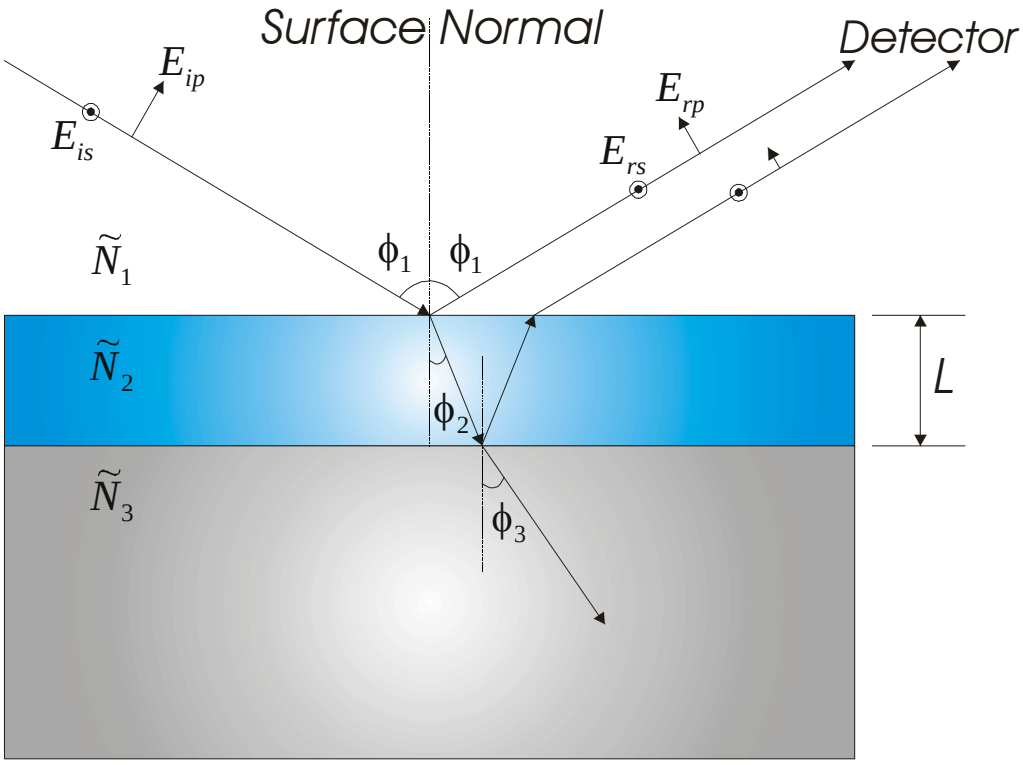

Figure 2.11 Geometry of reflection and refraction when a monochromatic polarized light is incident on a film-covered substrate with the complex index of refraction $\tilde{N}_1$, $\tilde{N}_2$ and $\tilde{N}_3$.

The Fresnel reflection coefficients contained in Equations 2.48 and 2.49 are calculated in a similar manner as Equations 2.43 and 2.44, and are defined below.

$$r_{12}^{p} = \frac{\tilde{N}_2 \cos\phi_1 - \tilde{N}_1 \cos\phi_2}{\tilde{N}_2 \cos\phi_1 + \tilde{N}_1 \cos\phi_2} \tag{2.51}$$

$$r_{23}^{p} = \frac{\tilde{N}_3 \cos\phi_2 - \tilde{N}_2 \cos\phi_3}{\tilde{N}_3 \cos\phi_2 + \tilde{N}_2 \cos\phi_3} \tag{2.52}$$

$$r_{12}^{s} = \frac{\tilde{N}_1 \cos\phi_1 - \tilde{N}_2 \cos\phi_2}{\tilde{N}_1 \cos\phi_1 + \tilde{N}_2 \cos\phi_2} \tag{2.53}$$

$$r_{23}^{s} = \frac{\tilde{N}_2 \cos\phi_2 - \tilde{N}_3 \cos\phi_3}{\tilde{N}_2 \cos\phi_2 + \tilde{N}_3 \cos\phi_3} \tag{2.54}$$

Now, the total reflection coefficients are used to calculate ρ, analogous to the bare surface example, and are once again related to Δ and Ψ (Equation 2.55).

$$\rho = \frac{R^p}{R^s} = \tan\Psi e^{i\Delta} = p(\tilde{N}_1, \tilde{N}_2, \tilde{N}_3, L, \phi_1, \lambda) \tag{2.55}$$

The fundamental equation of ellipsometry is thus obtained, where ρ is now a function of the complex index of refraction of the film ($\tilde{N}_2$), as well as the film thickness (L), in addition to the ambient and substrate materials properties ($\tilde{N}_1, \tilde{N}_3$) and experimental (ϕ_1, λ) parameters. Furthermore, the dielectric response function is replaced by the pseudo-dielectric response function $\langle\hat{\varepsilon}\rangle$ (Equation 2.56), since the probe beam measures the combined effect of the film-substrate system.

$$\langle\hat{\varepsilon}\rangle = \sin^2\phi_1 + \sin^2\phi_1 \tan^2\phi_1 \left(\frac{1-\rho}{1+\rho}\right)^2 \tag{2.56}$$

For each additional film that may be present, additional terms are added in order to calculate the appropriate ρ.

The task now becomes extracting the desired materials properties from the measured Δ and Ψ values via the complex reflection coefficient. Since ellipsometry involves the measurement of two known values, the extraction of two of the unknown properties is straightforward. For example, in the case of a single homogeneous film on a homogeneous substrate, the complex indices of refraction of the film and substrate are often known, or can be found in the literature. The ambient is typically air ($n=1, k=0$), and the angle of incidence and the wavelength are known. Therefore, the film thickness is the only unknown parameter. The extraction of the film thickness is accomplished by the use of an optical model in a software package such as WVase by J.A. Woollam Co.[11]

2.4.5 Heterogeneous Systems and Effective Medium Approximation

Often times, the film and/or substrate are not homogeneous in nature. Consequently, the indices of refraction are not known, and hence the dielectric response function is unknown and must be approximated. In this case, effective medium approximations are used to treat the heterogeneous material as a combination of homogeneous materials to yield a pseudo-dielectric response function. In general, an effective medium approximation (EMA) has the form given in Equation 2.57,

$$\frac{\langle\hat{\varepsilon}\rangle - \hat{\varepsilon}_h}{\langle\hat{\varepsilon}\rangle + 2\hat{\varepsilon}_h} = \sum_{j=1}^{m} f_j \frac{\hat{\varepsilon}_j - \hat{\varepsilon}_h}{\hat{\varepsilon}_j + 2\hat{\varepsilon}_h} \tag{2.57}$$

where $\langle\hat{\varepsilon}\rangle$ is the pseudo-dielectric response function of the heterogeneous material, $\hat{\varepsilon}_h$ is the dielectric response function of the host material, $\hat{\varepsilon}_j$ is the dielectric response function of the

homogeneous components, and f_j is the volume fraction of each component. Each component is treated as a sphere that is large enough to retain the dielectric response function of the bulk material, yet is smaller than the wavelength of the probe light beam. Several EMA's are used to model various types of heterogeneous materials as discussed below.

The Lorentz-Lorenz EMA is obtained by treating the host material as vacuum ($\hat{\varepsilon}_h = 1$), as in Equation 2.58.[12,13]

$$\frac{\langle\hat{\varepsilon}\rangle - 1}{\langle\hat{\varepsilon}\rangle + 2} = \sum_{j=1}^{m} f_j \frac{\hat{\varepsilon}_j - 1}{\hat{\varepsilon}_j + 2} = f_1 \frac{\hat{\varepsilon}_1 - 1}{\hat{\varepsilon}_1 + 2} + f_2 \frac{\hat{\varepsilon}_2 - 1}{\hat{\varepsilon}_2 + 2} \tag{2.58}$$

The constituents (1 and 2 above) are considered to be heterogeneously mixed in the host vacuum, with material 1 having a volume fraction equal to f_1, and material 2 equal to f_2. More commonly, the host material is not vacuum. In this case, the general form of the Maxwell-Garnett EMA is obtained (Equation 2.59).[14]

$$\frac{\langle\hat{\varepsilon}\rangle - \hat{\varepsilon}_h}{\langle\hat{\varepsilon}\rangle + 2\hat{\varepsilon}_h} = \sum_{j=1}^{m} f_j \frac{\hat{\varepsilon}_j - \hat{\varepsilon}_h}{\hat{\varepsilon}_j + 2\hat{\varepsilon}_h} = f_1 \frac{\hat{\varepsilon}_1 - \hat{\varepsilon}_h}{\hat{\varepsilon}_1 + 2\hat{\varepsilon}_h} + f_2 \frac{\hat{\varepsilon}_2 - \hat{\varepsilon}_h}{\hat{\varepsilon}_2 + 2\hat{\varepsilon}_h} \tag{2.59}$$

If one of the components in the Maxwell-Garnett EMA acts as the host (material 1, for example), then the EMA in Equation 2.60 is generated.

$$\frac{\langle\hat{\varepsilon}\rangle - \hat{\varepsilon}_1}{\langle\hat{\varepsilon}\rangle + 2\hat{\varepsilon}_1} = \sum_{j=1}^{m} f_j \frac{\hat{\varepsilon}_j - \hat{\varepsilon}_1}{\hat{\varepsilon}_j + 2\hat{\varepsilon}_1} = f_2 \frac{\hat{\varepsilon}_2 - \hat{\varepsilon}_1}{\hat{\varepsilon}_2 + 2\hat{\varepsilon}_1} \tag{2.60}$$

Maxwell-Garnett EMAs are most effective for approximating heterogeneous materials in which the host component completely surrounds the remaining components.[14] The final EMA that will be discussed is the Bruggeman EMA (BEMA), in which the host material is assigned the dielectric response function of the heterogeneous material in question.[15] This is referred to as the self-consistent model and has the form of Equation 2.61.

$$\frac{\langle\hat{\varepsilon}\rangle - \langle\hat{\varepsilon}\rangle}{\langle\hat{\varepsilon}\rangle + 2\langle\hat{\varepsilon}\rangle} = 0 = \sum_{j=1}^{m} f_j \frac{\hat{\varepsilon}_j - \langle\hat{\varepsilon}\rangle}{\hat{\varepsilon}_j + 2\langle\hat{\varepsilon}\rangle} = f_1 \frac{\hat{\varepsilon}_1 - \langle\hat{\varepsilon}\rangle}{\hat{\varepsilon}_1 + 2\langle\hat{\varepsilon}\rangle} + f_2 \frac{\hat{\varepsilon}_2 - \langle\hat{\varepsilon}\rangle}{\hat{\varepsilon}_2 + 2\langle\hat{\varepsilon}\rangle} \qquad (2.61)$$

2.4.6 Model Optimization

The parameter used to determine the quality of the match between the calculated and the experimental data is the mean-squared error (MSE) and is given in Equation 2.62.[16]

$$MSE = \frac{1}{2N - M} \sum_{i=1}^{N} \left[\left(\frac{\Psi_i^{cal} - \Psi_i^{\exp}}{\sigma_{\Psi,i}^{\exp}} \right)^2 + \left(\frac{\Delta_i^{cal} + \Delta_i^{\exp}}{\sigma_{\Delta,i}^{\exp}} \right)^2 \right] \qquad (2.62)$$

where N is the number of (Ψ, Δ) pairs, M is the number of variable parameters in the model, and σ is the standard deviation on the experimental data points. Therefore, data points with large standard deviations are not weighted as heavily as those with a tight distribution. Better fits between modeling and experimental data will have positive values approaching zero.

Once the best-fit parameters have been obtained it is necessary to evaluate the standard 90% confidence limit (SCL) and correlation matrix values. The value expressed in the SCL can be understood as how sensitive the parameter is to the fit. Correlation matrix values tell us how "independent" fit parameters are. Correlation values of unity indicate strong correlation between fit parameters. Practically this means that the parameters can both vary and give the same quality fit.

Thus far we have demonstrated what and how ellipsometry measures, and also the way to construct optical models and perform theoretical calculations, if we have previous information about the sample from other sources. Through the comparison of model calculations with highly accurate ellipsometric measurements, optical or other physical properties about the system under study can be obtained.

2.5 References

1. E.A. Irene, Thin Solid Films **233**, 96 (1993).

2. C. Lopez, Ph.D. dissertation, University of North Carolina at Chapel Hill, 2005.

3. E.A. Irene and J.A. Woollam, Mater. Res. Soc. Bulletin **20**, 24 (1995).

4. E.A. Irene and R.W. Collins, in *Mater. Res. Soc. Short Course on Ellipsometry Fundamentals and Applications* (1995).

5. R.M.A. Azzam and N.M. Bashara, in *Ellipsometry and Polarized Light*, (Elsevier Science Publishers B.V., The Netherlands, 1989)

6. D.S. Kliger, J.W. Lewis, and C.E. Randall, in *Polarized Light in Optics and Spectroscopy*, (Academic Press, Boston, MA, 1990).

7. W.L.L. Lai, Ph.D. dissertation, University of North Carolina at Chapel Hill, 1999.

8. J. Brewer, Ph.D. dissertation, University of North Carolina at Chapel Hill, 2003.

9. L. Spanos, Ph.D. dissertation, University of North Carolina at Chapel Hill, 1994.

10. H.G. Tompkins and W.A. McGahan, in *Spectroscopic Ellipsometry and Reflectometry- A User's Guide*, (John Wiley & Sons, New York, NY, 1999).

11. http://www.jawoollam.com/tutorial_6.html.

12. L. Lorenz, Ann. Phys. (Liepzig) **11**, 70 (1880).

13. H.A. Lorentz, in *Theory of Electrons*, 2nd Edition, (Teubner, Liepzig, 1916).

14. *SCI Filmwizard Getting Started Manual- Professional Version*, (Scientific Computing International, Encinitas, CA, 1994).

15. D.A.G. Bruggeman, Ann. Phys. (Liepzig) **24**, 636 (1935).

16. Y. Gao, Ph.D. dissertation, University of North Carolina at Chapel Hill, 2000.

CHAPTER 3 – ORGANIC SEMICONDUCTORS AND ORGANIC THIN FILM TRANSISTORS

3.1 Overview

Organic materials are found throughout everyday life in applications ranging from packaging to videotape, and from furniture to clothing. This is because they can be readily shaped and manufactured, and their properties can be tailored to a particular application. Conventional plastics are electrical insulators, but the discovery of a remarkable class of polymers that can conduct electricity has opened a new era of plastics science and technology.[1] Since then, organic semiconductors have been the subject of intense research because of their promising applications in electronic and optoelectronic devices.[2] Although organic electronics are still far from (and actually not expected to be) replacing the high-end semiconductor devices, they are very promising in applications where flexibility, reduced cost, and ease of production are needed which cannot be provided by the current silicon based devices. Generally organic semiconducting materials are readily processed from solution, and have exceptional scope for molecular engineering to enable their properties to be tailored. They can be used to make a wide range of semiconducting electronic devices such as thin film transistors (TFT's), light-emitting diodes, solar cells and even lasers.[3] Organic electronic devices generally employ thin films of the semiconductor material as the

active region (where charge is carried) shown in Figure 1.2. And the device performance largely depends on the active film quality. Organic semiconductors can be small monomeric molecules such as pentacene and anthracene, or large macromolecules such as polyacetylene or poly(*p*-phenylenevinylene). Likewise, organic semiconductors can be categorized into classes of amorphous, crystalline, or a combination of both depending on their molecular structure, electronic structure, and the conditions under which the films are prepared. Figure 3.1 shows the schematic diagrams of these different classes of organic semiconductors.

In this Chapter, the molecular structure and formation of electronic states for organic semiconductors will be discussed. The fabrication and performance comparison of variable configurations of organic thin film transistors (OTFT's) are explained. Performance parameters such as charge mobility, turn on/off ratio, and leakage currents will be presented along with several theories on charge transport in organic semiconductors. The electronic measurements will be discussed together with the explanation of the custom built probe station.

3.2 Organic Semiconducting Materials

Semiconducting properties associated with organic materials usually derive from conjugated conformation in carbon-containing compounds, i.e. the extended π-orbitals or delocalized electrons from $sp^2 + p_z$ hybridization. The delocalized π-electrons will fill up a whole band. This π-bands in the organic semiconductor are normally called molecular orbitals. The filled π-band is called the Highest Occupied Molecular Orbital (HOMO), and the empty/anti π-band is called the Lowest Unoccupied Molecular Orbital (LUMO). Figure 3.2 illustrates the formation of this molecular orbitals using polyethylene as the example.

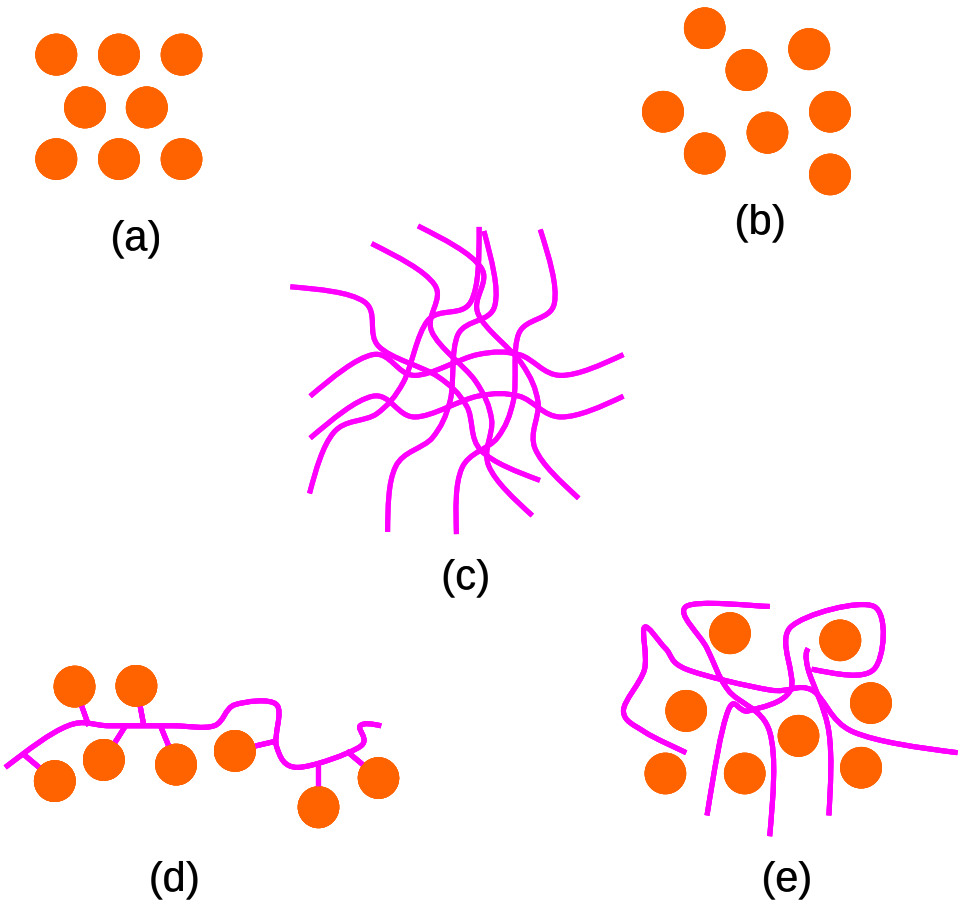

Figure 3.1 Schematic diagrams of different classes of organic semiconducting materials. (a) molecular crystalline e.g. pentacene at low temperature, (b) molecular amorphous e.g. NDA-N1, (c) conjugated polymer e.g POMA, (d) polymer with pendant active group e.g. PVK polyvinyl carbazole, and (e) molecularly doped polymer e.g. POMA doped with cresol of HCl.

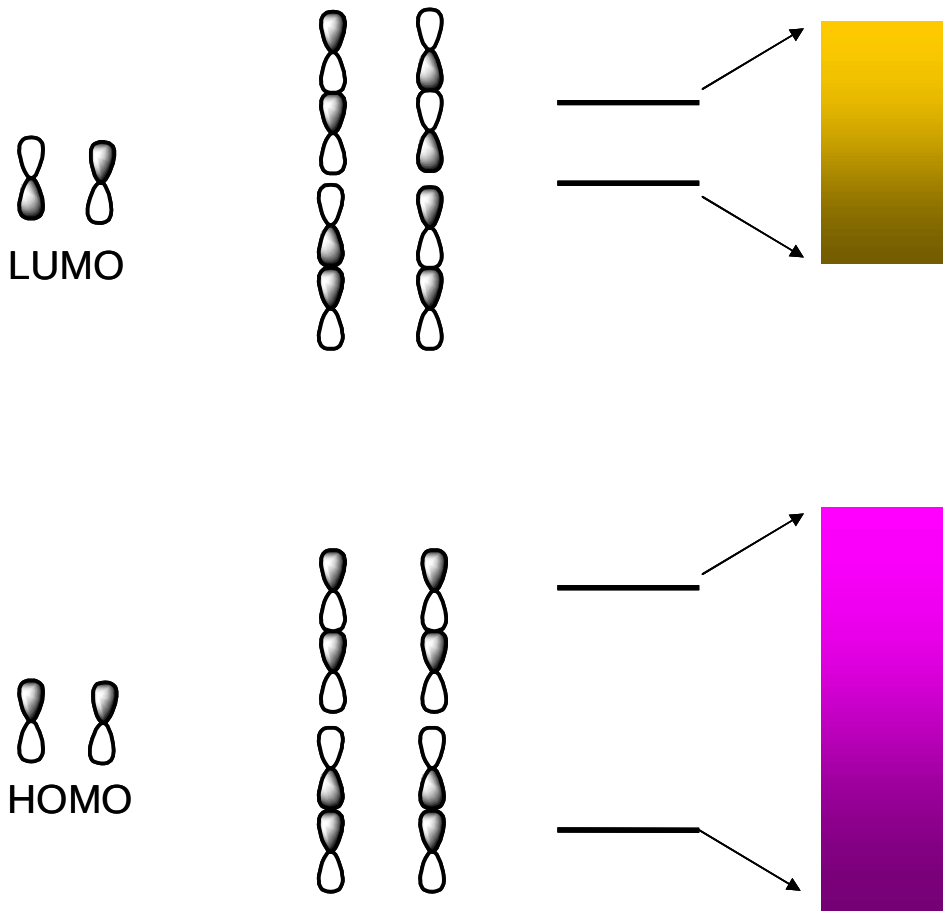

Figure 3.2 Illustration of bonding and anti-bonding orbital interaction of HOMO and LUMO orbitals of a segment of polyethylene molecule.

The electronic transport over macroscopic distances requires mutual overlap of the π-bands between adjacent molecules. The scope for introducing electronic charges is restricted by the high ionization potential and low electron affinity for this high energy gap semiconductor. As the length of the conjugated sequence is increased, the energy gap between HOMO and LUMO decreases. Some typical organic semiconductors are pentacene, polyacetylene, poly(*p*-phenylene), polyaniline, polypyrrole, and polythiophene, whose molecular structures are illustrated in Figure 3.3.

3.3 Charge Transport in Organic Semiconductors

In metals and conventional semiconductors, charge transport occurs in delocalized states, and is limited by the scattering of the carriers, mainly on phonons, that is, thermally induced lattice deformations. For example charge carriers in crystal silicon move as Bloch waves in highly delocalized planes and wide bands and the charge mobility is as high as 10^3 $cm^2V^{-1}s^{-1}$. At very low temperature the charge mobility for organic semiconductors can also approach 10 $cm^2\,V^{-1}s^{-1}$ (e.g. pentacene at ~ 17 K). This high mobility suggests that the charge transport in organic semiconductors at low temperature is similar to that in inorganic semiconductors.[4] However, with increased temperature, the effective band widths are progressively reduced by lattice vibration and strong phonon-charge carrier coupling.[5,6] The van der Waals force, the most significant intermolecular interaction in organic films, is only 40 KJ/mol whereas the lattice vibration can be higher than 50 KJ/mol, which prevents molecular chain alignment and prevent long range lattice formation.[7] Therefore, the band like charge transport model is no longer valid and the charge delocalization is often restricted to single units.

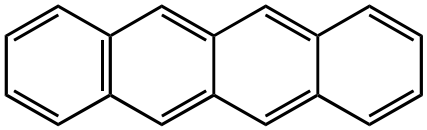

Pentacene

Polyacetylene

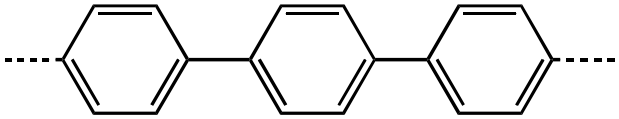

Poly(*p*-phenylene),

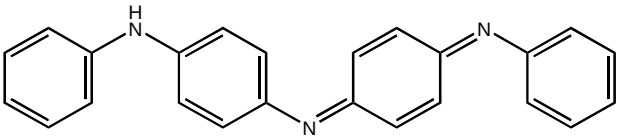

Polyaniline

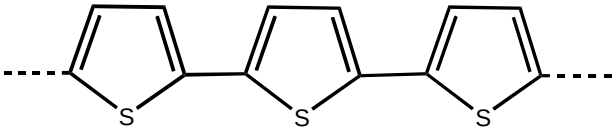

Polypyrrole

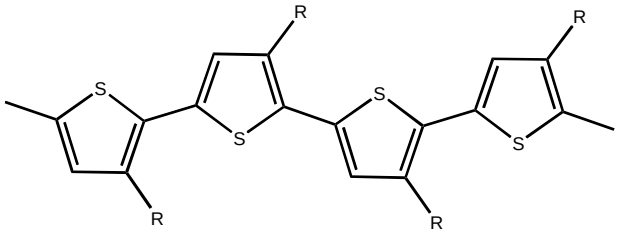

Polythiophene

Figure 3.3 Examples of some well-known organic semiconducting materials.

Most organics are amorphous and at best polycrystalline. The impurities and disorder present in amorphous solids effectively reduces the charge mobility to 10^{-4} to 10^{-2} $cm^2V^{-1}s^{-1}$ range as the charges are trapped and scattered. Alternative charge transport mechanisms are necessary to explain the phenomena. Hopping transport of charges between localized states is thus proposed. In this section, several charge transport models are discussed; they are band transport, hopping transport, field-dependent transport, and multiple trapping and release transport.

3.3.1 Band Transport

The band transport model is generally applied for charge transport in inorganic crystal semiconductors, where a regularly spaced tightly bound lattice forms a band structure and the charge carriers are delocalized over a large area with little hindrance.[8] Some organic semiconductors can also form orderly molecular arrangement and show comparable charge transport. For example, mobility of ~ 1 $cm^2 V^{-1} s^{-1}$ has been reported for pentacene at room temperature, which increases considerably to values as high as 10^2 $cm^2 V^{-1} s^{-1}$ at 1.7 K. This power law dependence of mobility on temperature ($\mu \propto T^{-n}$) and the observation of a quantum Hall effect presents a good argument that structured organic materials at low temperature can demonstrate band like conduction.

The schematic diagram for delocalized band transport is shown in Figure 3.4. Charge carriers will be scattered when they come in contact with defects, or as-shown lattice vibrations, which will reduce the charges moving in forward direction. At low temperature there will be less molecular vibrations and low chance of charge scattering. Consequently, the carrier mobility, μ shows dependence on temperature ($\mu \propto T^{-n}$). At room temperature,

band transport is difficult because of increased molecular lattice vibration, which causes the charge carriers to scatter significantly.

3.3.2 Hopping Transport

In most amorphous organic films, the charge carriers are strongly localized in potential wells. In these materials, the hopping of localized charges between these potential wells has been reported as a main mechanism of charge transport.[9] A main difference between the delocalized and localized transport is that, in the former, the transport is limited by phonon scattering, whereas in the latter, it is phonon assisted. Accordingly, the charge mobility decreases with temperature in conventional semiconductors, while the reverse being true in most organic materials. The sources of the aforementioned potential wells can be either extrinsic or intrinsic. The grain boundaries, packing imperfections, impurities in lattice and interfacial states are considered extrinsic causes of localization. Intrinsic cause arises from polarons, which are formed when a moving charge polarizes the lattice around it. The resulting lattice polarization acts as a localization site and hinders the movement of the charge, thus decreasing the charge mobility.[5]

Figure 3.5 shows a diagram of various trapping sites in an organic semiconductor. The molecular vibrations in the solid provide the activation energy for the charge carriers indicated by the red dots to hop from one shallow trap site to an adjacent trap site in the direction of the electric field. Temperature affects the mobility positively by several orders of magnitude because the charge transport is assisted by the lattice vibrations.[7] This process of thermally activated tunneling from an occupied site to an empty was initially described by Mott as phonon assisted hopping (Equation 3.1).[10]

$$\mu = \mu_0 \exp[-(T_0 / T)^{1/\alpha}] \qquad (3.1)$$

where α is an integer ranging from 1 to 4. When $\alpha = 4$, typical Arrhenius behavior is observed in many thermally activated processes, which suggests that thermal energy assists the charges to hop between localized sites in the direction of the electric field.

With further increase in temperature, the number of molecules with adequate energy required for activation of the charge carriers to hop increases (the energy distribution curve in the Boltzmann's distribution shifts to the right). Miller and Abraham developed Mott's ideas and proposed Equation 3.2 to account the hopping rate between an occupied site *i* and an adjacent unoccupied site *j*:[11]

$$v_{ij} = v_0 \exp(-2\gamma R_{ij}) \begin{cases} \exp\left(\dfrac{E_i - E_j}{k_B T}\right) & E_i > E_j \\ 1 & E_i < E_j \end{cases} \qquad (3.2)$$

where v_0 is the frequency of hopping corrected by the tunneling probability and the probability of absorbing thermal energy, $E_i - E_j$ is energy difference between the two sites and R_{ij} is the physical separation between the two sites. The wave function overlap between the two sites is γ^{-1} and, and k_B is the Boltzmann's constant. This model addresses hopping mechanism of charge transport between three dimensional shallow impurity states in a compound with weak lattice coupling such as amorphous semiconductors.[12] The density of these shallow trap sites can be increased by annealing the organic film which improves molecular alignment and results in improved mobility. This effect will be presented in Chapter 5 where the optimization of OTFT performance is discussed.

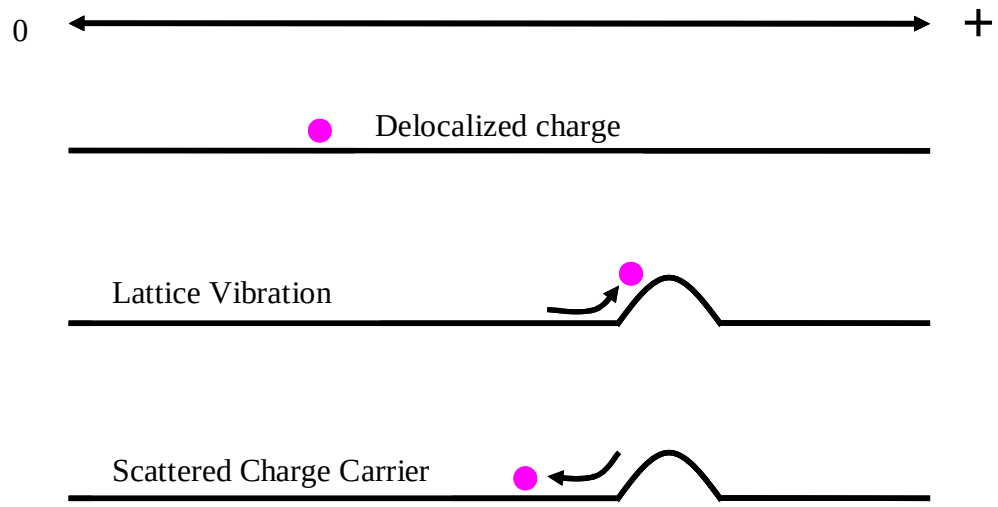

Figure 3.4 Delocalized charge in a crystal lattice, and charge scattering due to lattice vibration.

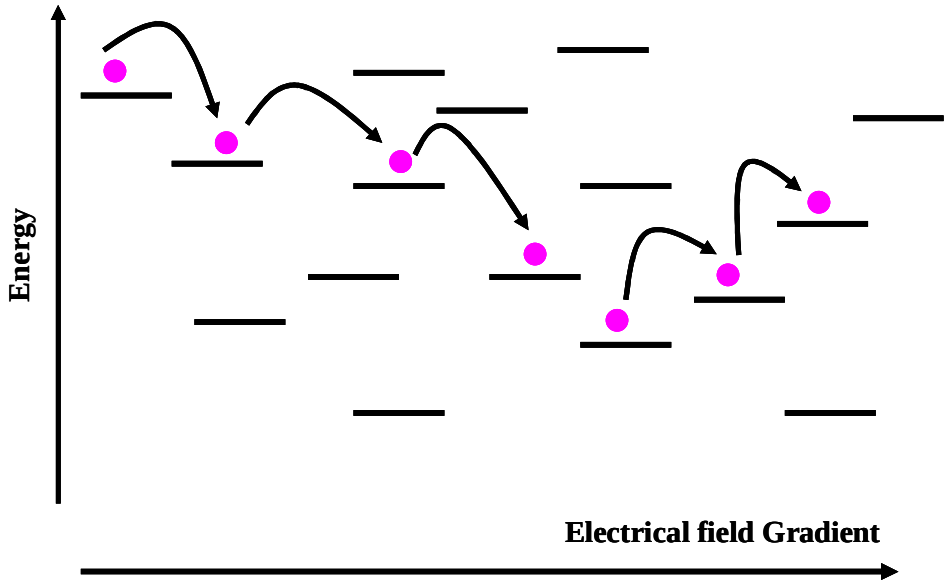

Figure 3.5 Phonon assisted hopping of charges between localized sites.

3.3.3 Field-Dependent Transport

A general feature of charge transport in organic materials is that the mobility becomes field dependent at high electric field (in excess of 10^5 V/cm). This phenomenon occurs through a Poole-Frenkel mechanism[13], in which the coulombic potential near the localized levels is modified by the applied field in such a way as to increase the tunnel transfer rate betweens sites. The general dependence of the mobility is given by Equation 3.3:

$$\mu(E) = \mu(0)\exp\left(\frac{q}{k_B T}\beta\sqrt{E}\right) \tag{3.3}$$

Where $\mu(0)$ is the mobility at zero field, $\beta = (e/\pi\varepsilon\varepsilon_0)^{1/2}$ is the Poole-Frenkel factor, and E is the magnitude of the electric field.

3.3.4 Multiple Trapping and Release

Multiple Trapping and Release (MTR) model was first described in 1970 by Comber *et at.*[14] MTR was widely used to account for charge transport in amorphous silicon. It combines the band transport and hopping transport, where a narrow delocalized band is associated with a high concentration of localized levels that act as traps as shown in Figure 3.6. The delocalized bands are formed by the $\pi - \pi$ band overlap in the semiconductor.[15] Likewise, the grain boundaries, impurities, and interface states form the traps. As a charge carrier travels, it continuously interacts with these trap sites, and is released to the delocalized band through thermal activation. In this model, two assumptions are usually made: the carriers arriving at a trap are instantaneously trapped with a probability close to one and the release of trapped carriers is controlled by a thermally activated process. The resulting

effective drift mobility μ_{eff} in the delocalized band by an expression of the form in Equation 3.4:[16]

$$\mu_{eff} = \mu_0 \alpha \exp\left(\frac{-E_a}{kT}\right) \tag{3.4}$$

where E_a is the energy difference between the trap level and the delocalized band edge and α is the ratio of the density of charge carriers at the delocalized band to density charge carriers in the trapped states.

The schematic diagram in Figure 3.6a illustrates a simple MTR transport. In this model, when the gate voltage is applied to the OTFT, the charge carriers are accumulated at the interface of the gate dielectric and the semiconductor. As the energy level of the charge carriers are raised, which raises the Fermi level (E_F), the lower energy trap sites of the semiconductor are filled, thereby initially reducing the number of charge carriers. When multiple trapping sites are available as shown in Figure 3.6b, the charge carriers can interact with a wide range of trapping sites. Therefore, the free carrier available then becomes a direct function of gate voltage V_G, which can also provide the activation energy for the carriers to be released and transported to the delocalized band. With the increase in V_G, as more and more charges start accumulating in the interface, they start occupying trap sites at relatively high energies. These additional charges at higher energy levels will require less activation energy to hop to a neighboring trap sites and into the delocalized area. This mechanism results in a higher mobility with increasing gate voltage and higher temperature.

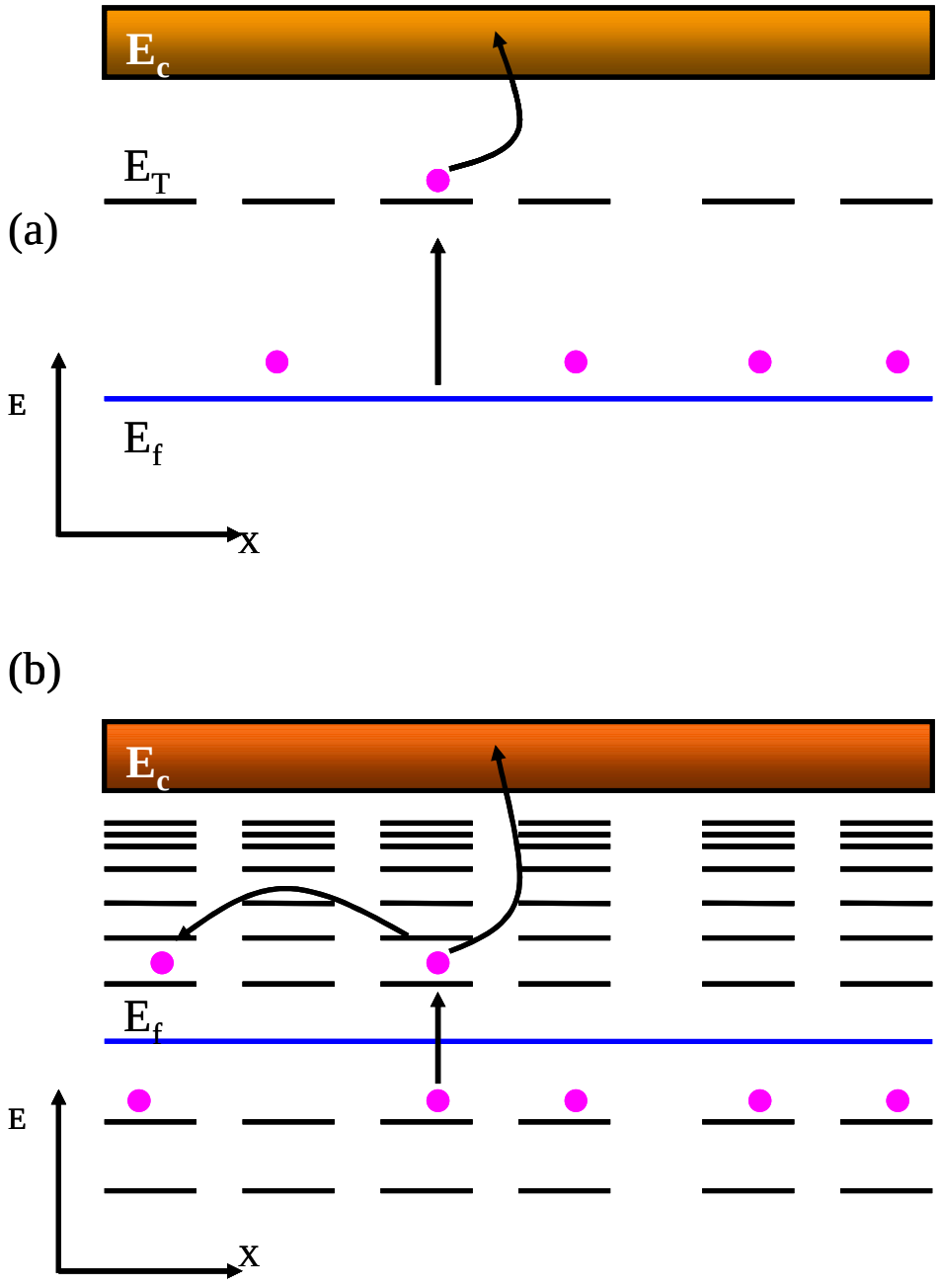

Figure 3.6 Schematic illustration of (a) single trap, and (b) multiple traps in organic semiconducting materials.

3.4 OTFT Operation and Modeling

3.4.1 OTFT Design and Geometry

The common device configurations used in OTFT's will be discussed in this section. The working technology of a traditional MOSFET and OTFT has been discussed in Chapter 1. Typically, an OTFT is constructed using an inverted gate stack, and the two design structures of OTFT are shown in Figure 3.7. The bottom-contact architecture is shown in Figure 3.7a and the top-contact structure is shown in Figure 3.7b. The bottom contact is fabricated by first depositing the source and drain lines on an oxide substrate, and the semiconductor film is then deposited on this structure. This design is easy to fabricate and the resistance for charge transport between source and the drain is minimized. However, it is difficult to measure the film thickness on the source and drain structures. In the top contact structure, the substrate oxide is coated with film, and then the metal lines for the source and drain contacts are deposited by vacuum evaporation as quickly as possible to prevent the semiconductors from decomposing at high temperatures. The deposited film thickness is easy to be measured. In this design, the shortest distance for charge transport between the source and drain will be obtained if the charge carriers move at the air-semiconductor interface in Figure 3.7b. However, the charge carriers travel from source to drain by forming a channel at the semiconductor-dielectric interface where the electric field is the greatest. The charges thus have to travel an added distance as indicated by the trajectory of the blue dots shown in Figure 3.7b. This added distance increases the resistance for charge transport. The details of device performance for bottom-contact and top-contact will be discussed in Chapter 5.

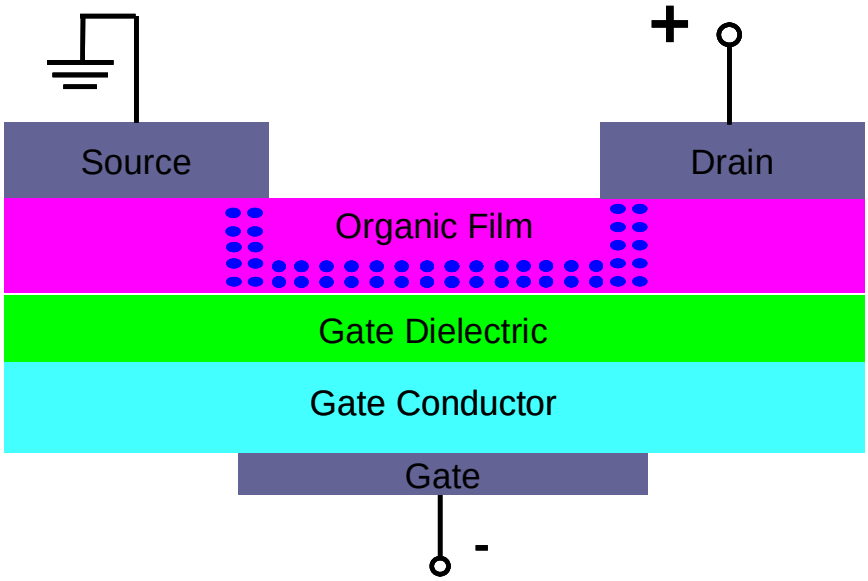

(a)

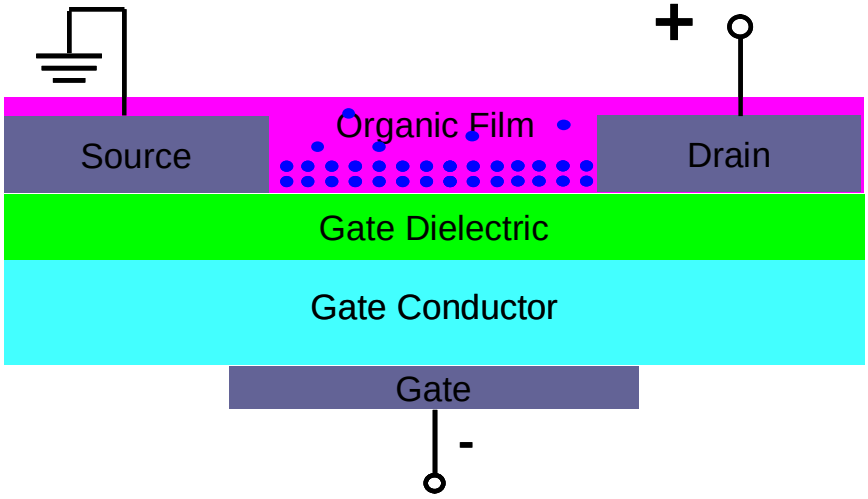

(b)

Figure 3.7 Common configurations of OTFT designs with (a) bottom-contact and (b) top-contact designs.

The deposition of the semiconductor is the determining step of the OTFT fabrication, especially when using a thermally oxidized silicon wafer as substrate, where the rest of the process is controlled by conventional techniques. Several deposition methods such as electropolymerization, spin-casting, vacuum evaporation, and Langmuir-Blodgett techniques have been used to make organic semiconductor films. In this study, spin-casting was chosen with its convenience and resulting smooth films.

3.4.2 Principles of Operation

An overall view relative to the operation of both MOSFET and OTFT has been discussed in Chapter 1. Here details of observations during the OTFT operation and the molecular contribution in the active layer will be presented. In order to better understanding the charge transport process in OTFT's, we start the discussion with organic films aligned well with one another. The electric field from applied gate potential will alter the Fermi level, E_F of HOMO, which changes the energy of the charge carriers, and thus affects the inter-chain charge transport. Figure 3.8 shows a schematic diagram of how the gate potential affects the concentration of charge carriers in the semiconductor (an example of P-channel organic material is used). When no gate voltage is applied, as in Figure 3.8a, a flat band situation is observed where no charges flow between the source and the drain. E_F is aligned with the source and the drain, but the conducting states between HOMO and LUMO are energetically far from the Fermi level. When negative gate voltage applied, the HOMO level is increased and closer to the Fermi level, which forms a channel and permits charge to flow from source to drain as shown in Figure 3.8b. In addition to the gate voltage, the increase in drain voltage, as shown in Figure 3.8c, acts as a driving force for the charges to flow between drain and the source.

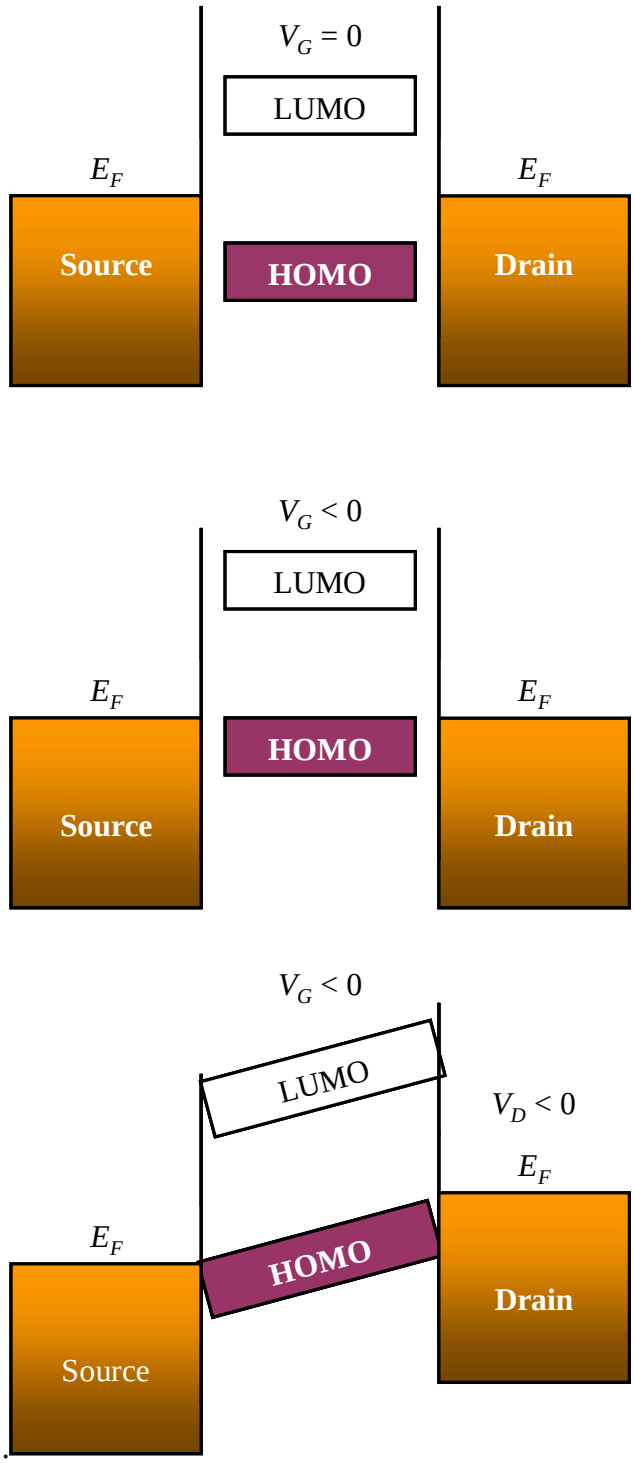

Figure 3.8 Schematic illustration of OTFT operation when applying (a) zero gate voltage, (b) negative gate voltage, and (c) drain voltage together with negative gate voltage.

A typical I-V plot obtained during the electronic measurement of a P-channel OTFT is shown in Figure 3.9. It consists of linear regime and saturation regime. When negative gate voltage is applied, the electric field across the dielectric draws the majority carriers to the interface of semiconductor and the gate dielectric layer. When the gate voltage is increased, more charges accumulate at the interface of the dielectric and the semiconductor, increasing the width of the channel. These charges form a P-channel illustrated by a white band in Figure 3.10a, which permits charge flow between source and the drain. The current follows Ohm's law and is proportional to V_D. As the gate voltage increases further, a pinch-off region is observed followed by a saturation level. At pinch-off voltage, a depletion region starts to form around the electrode as the charges density approaches zero (Figure 3.10b), and reaches zero at saturation (Figure 3.10c). Once the saturation region is reached, the increase in drain voltage does not cause increase in current.

The $I-V$ characteristics can be calculated in the gradual channel (or Shockley) approximation, based on the assumption that the electric charge density related to a variation of the electric field along the channel is much smaller than that related to a variation across the channel, namely $\left|\partial E_x / \partial x\right| << \left|\partial E_y / \partial y\right|$, where *E* is the electric field, and *x* and *y* the directions parallel and perpendicular to the dielectric-semiconductor interface, respectively. This condition is generally fulfilled when the channel length *L* is much larger than the dielectric thickness. A typical linear region is experienced in the region where $V_{SD} < V_G$ and the drain-source current I_{SD} can be calculated through Equation 3.5: [17]

$$I_{SD} = \frac{W}{L} C_{Die} \mu \left(V_G - V_T - \frac{V_{SD}}{2} \right) V_{SD} \qquad (3.5)$$

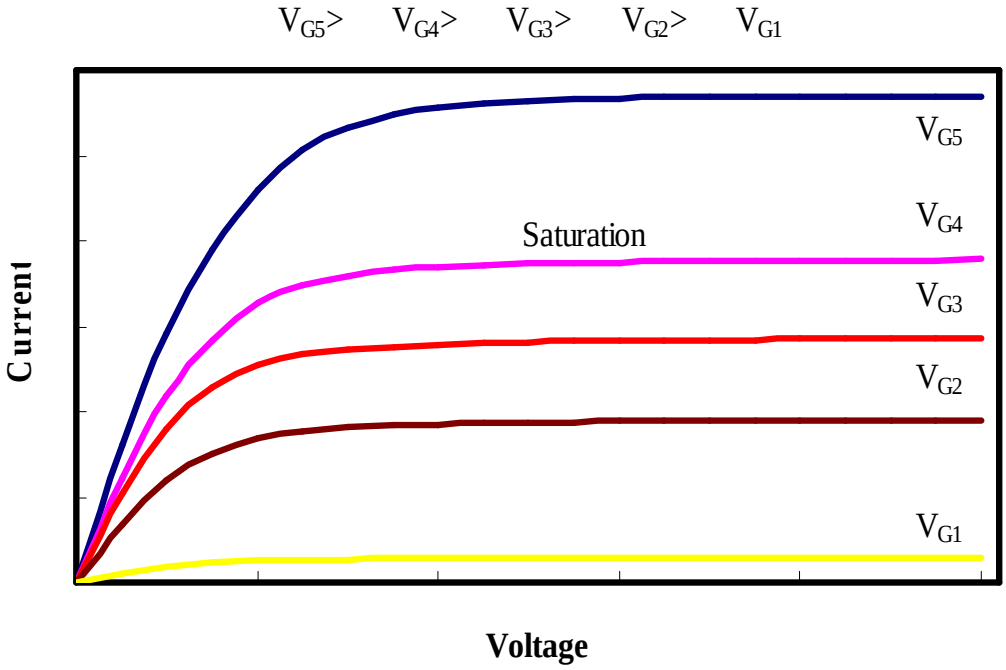

Figure 3.9 Typical drain-current-voltage characteristic of OTFT's

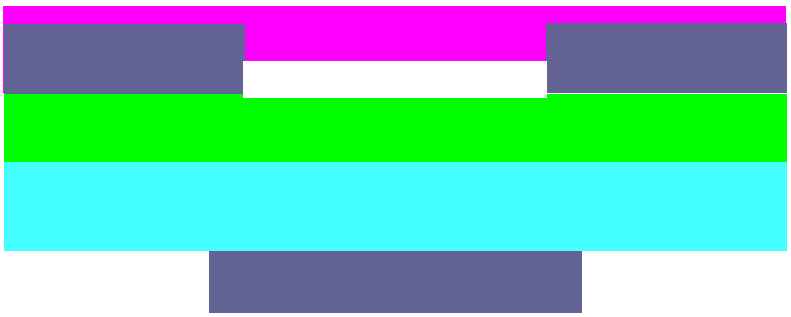

(a) Linear Region $V_D < V_G$

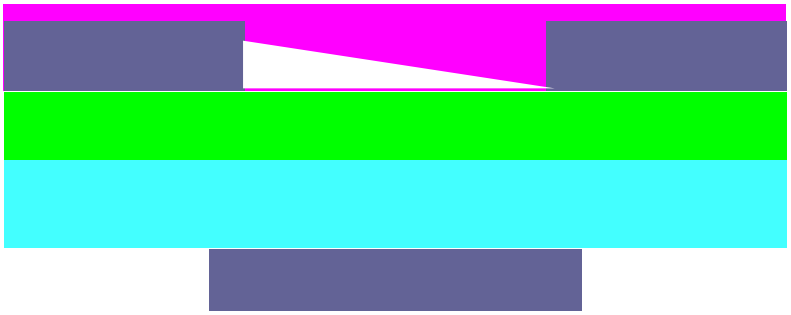

(b) Pinch-off Region $V_D \sim V_G$

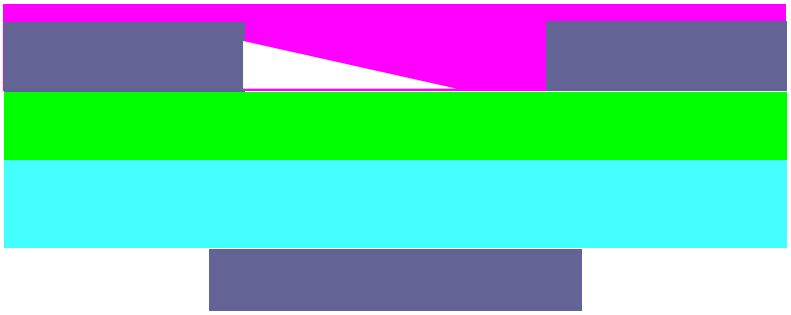

(c) Saturation Region $V_D > V_G$

Figure 3.10 Illustration of different regimes during an OTFT operation. (a) linear region, (b) pinch-off region, and (c) saturation.

where C_{Die} is the dielectric capacitance (per unit area), W and L are the width and length of the channel, μ is the charge mobility in the semiconductor, and V_T is the threshold voltage which accounts for the voltage dropped across the dielectric layer due to interface states and impurities and is also the point turn on point of the device. A pinch off is observed when V_{SD} approaches V_G and a saturation occurs when $V_{SD} > V_G$. In the saturation region of the plot, V_{SD} is replaced by $V_G - V_T$ which results in Equation 3.6:

$$I_{SD} = \frac{W}{2L} C_{Die} \mu (V_G - V_T)^2 \tag{3.6}$$

where there is almost no voltage dependence on current in this region.

3.4.3 Performance

Since the first report in 1987,[18] the performance of OTFT's has continuously improved. There are several parameters that are used to gauge the performance. The charge mobility, μ describes how charge carriers move within the active layer under the influence of the electric field. The switching speed of an OTFT is dependent on mobility and therefore high mobility is desired. Because charges transport by hopping between localized sites, the mobility is typically in the range of 10^{-5} to 10^{-1} $cm^2 V^{-1} s^{-1}$ for OTFT's. For comparison, amorphous silicon has a mobility of 0.1-1 $cm^2 V^{-1} s^{-1}$, and single crystalline silicon has a mobility of 1400 $cm^2 V^{-1} s^{-1}$. The field effect mobility in an OTFT is calculated from Equation 3.7:

$$\mu = \frac{L}{W C_{Die} V_{SD}} \left(\frac{\partial I_{SD}}{\partial V_G} \right) \tag{3.7}$$

where μ is the field effect mobility, *W* is the channel width, *L* is the channel length, $\frac{\partial I_{SD}}{\partial V_G}$ is the slope in the turn-on curve, and C_{Die} is dielectric capacitance per unit area.

Many factors affect the mobility of charge carriers and performance of OTFT's. It has been reported that increasing the substrate temperature during organic film deposition, doping and post-annealing are helpful for higher charge mobility.[19] In this study, we have considered alternate gate dielectric layers for the OTFT's, and post fabrication treatments such as annealing to improve the mobility of the OTFT. The gate material which capacitively couples the active semiconductor layer and the contact metal electrodes play a vital role in the performance of OTFT. A dependable gate material should have low defect densities, a smooth surface with very little roughness and form sharp interfaces that facilitates good morphology of the subsequent active layer deposition. Annealing also improves mobility by bringing the hopping sites closer together by densification.[14] The details of this study will be presented in Chapter 5.

The turn on/off ratio is indicative of the switching performance of an OTFT, and is defined as the ratio of current flowing between the source and the drain in the "on" and the "off" states. A low current is desired in the off state to minimize or eliminate leakage current in the inactive state. An on/off ratio as high as 10^6 have been reported for some OTFT's, but a much lower value is usually observed.[12]

3.4.4 Electrical Measurements

The electrical measurements were carried out using a Keithley 236 Source Measure Unit and an additional power supply was used to supply the gate voltage. The custom probe station was facilitated with two probe manipulators from Signa Corporation connected to the

source and drain electrodes. Software to automate the data collection process was LabVIEW™.

The vacuum enabled chuck was used to hold the sample firmly on the station, and to act as the gate electrode during the measurement. Figure 3.11 shows the schematic diagram of the vacuum chuck. The reverse side of silicon substrate was sanded with a diamond scriber to remove SiO_2 layer and GaIn eutectic coating was applied with a Q-Tip™ to make an ohmic contact between the device and the gate electrode.

The voltages reported here are source-drain voltage and source-gate voltages, with the source electrode grounded. Software assisted averaging of multiple data sets was carried out.

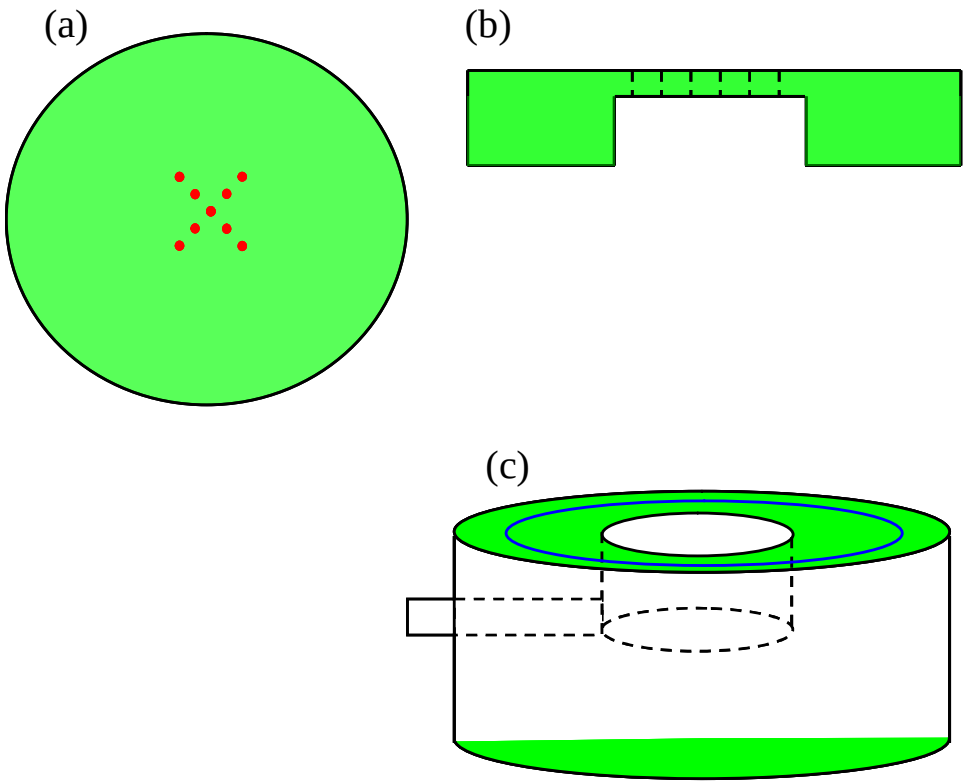

Figure 3.11 Schematic diagram of a vacuum enabled chuck (a) top view of brass plate with 0.5 mm holes drilled, (b) cross-section view of the brass chuck showing 0.5 mm hole and a cavity, and (c) Teflon base bored in the center, an outlet drilled to for vacuum tubing, and an o-ring ensuring the tight fit between the brass top and Teflon base.

3.5 References

1. C.K. Chiang, C.R. Fincher Jr., H. Shirakawa, E.J. Louis, S.C. Gau, A.G. MacDiarmid, Phys. Rev. Letter., **39**, 1098 (1977).

2. S. R. Forrest, Chem. Rev. **97**, 1793 (1997).

3. W. Riess, H. Riel, T. Beierlein, W. Brutting, P. Muller, P.F. Seidler, IBM J. res. & Dev. **45**, 77 (2001).

4. C.D. Dimitrakopoulos, P.R.L. Malenfant, Adv. Mater. **14** (2), 99 (2002).

5. J. Cornil, D. Beljonne, J.P. Calbert, J.L. Bredas, Adv. Mater. **13** (14), 1053 (2001).

6. M.M. Ling, Z.N. Bao, Chem. Mater. **16** (23), 4824 (2004).

7. I.D.W. Samuel, Poly. Elec. **358** (1765), 193 (2000).

8. J. Veres, S.D. Ogier, S.W. Leeming, D.C. Cupertino, S.M. Khaffaf, Adv. Funct. Mater. **13** (3), 199 (2003).

9. P. Granholm, J. Paloheimo, H. Stubb, Phys. Stat. Solid. **205** (1), 315 (1998).

10. G. Horowitz, Adv. Mater. **10** (5), 365 (1998).

11. F. Garnier, Photo. & Optoelectro. Poly., **672**, 420 (1997).

12. W.J. Feast, J. Tsibouklis, K.L. Pouwer, L. Groenendaal, E.W. Meijer, Polymer, **37** (22), 5017 (1996).

13. J. Frenkel, Phys. Rev. **54**, 647 (1938)

14. P.G.L. Comber, W.E. Spear, Phys. Rev. Lett. **25** (8), 509 (1970).

15. S.Y. Jung, Z. Yao, Appl. Phys. Lett., **86** (8), 2005

16. G. Horowitz, R. Hajlaoui, H. Bouchriha, R. Bourguiga, M. Hajlaoui, Adv. Mater. **10** (12), 923 (1998).

17. D.K. Schroder, Semiconductor material and device characterization. (Wiley: New York, 1990).

18. H. Koezuka, A. Tsumura, T. Ando, Synth. Met. **18**, 699 (1987).

19. F. Garnier, Chem. Phys. **282**, 253 (1998).

CHAPTER 4 – OPTICAL CHARACTERIZATION

4.1 Introduction

In Chapter 1 of this dissertation the relation of optical properties of organic semiconductors to the device properties was mentioned. In practice, a knowledge of the complex refractive index ($\tilde{N} = n + ik$ where *n* is the refractive index and *k* the absorption index) for an organic thin film, and the relationship of $\tilde{N}$ to aromatic $\pi - \pi$ band transitions are crucial for understanding and optimizing the performance of these devices.[1] For instance, the electroluminescence quantum efficiency of an organic LED is related to the refractive index *n*.[2] Oftentimes organic thin films are optically anisotropic, particularly polymer thin films, and the optical anisotropy can impact the optical and electronic properties.[3,4]

Katz *et al* reported[5] that low molecular weight naphthalenetetracarboxylic diimide derivatives were suitable as stable N-type organic semiconductors even in the presence of air, while previous N-type organic semiconductor devices failed because oxygen reactions limited the lifetime of these devices. Their naphthalene based imides with terminal fluorinated tails showed high electron mobilities (> 0.1 $cm^2V^{-1}s^{-1}$) and excellent turn on/off current ratios (> 10^5). Based on these results we have selected a compound recently prepared that has the suitable electronic groups indicated by Katz et al but also has groups that should

further enhance the compounds stability. This compound is a new naphthalene derivative and is called as NDA-n1 or NDA-n2 (see Chapter 1).

In this chapter, the optical properties of NDA-n2 and NDA-n1 thin films were investigated using variable angle SE over the photon energy range 1.5-4.5 eV. UV-Vis spectroscopy was used as complementary technique for SE. From the optical characterization the complex dielectric function and an assessment of the arrangement of molecules in the thin films were obtained. The morphology and roughness of film surface were measured by AFM and simulated by Bruggeman EMA layer. A detailed procedure for the detection of optical anisotropy in thin films is presented.

4.2 Experimental Details

The experimental procedure for optical characterization is illustrated in a chart as shown in Figure 4.1. The silicon wafers used in the study were commercially available P-type single crystalline silicon of (100) orientation with a resistivity of ~ 2 Ω-cm (Virginia Semiconductor, Inc.). The Corning fused silica was bought from Corning Company. The starting NDA solid was synthesized in a one-step procedure. The appropriate dianhydride and aryl-amine were stirred in glacial acetic acid for 2 h at room temperature, followed by refluxing for 12 h. The final products were crystallized from the reaction mixture and were further recrystallized from either dichloromethane or 1,2-dichlorobenzene. Details with respect to synthetic procedures and product work-up have been previously reported.[6]

NDA's thin films were deposited on substrates by spin coating from solutions using dichloromethane as the solvent. The spin speeds ranged from 1000 to 5000 rpm and the weight concentration was around 0.15%.

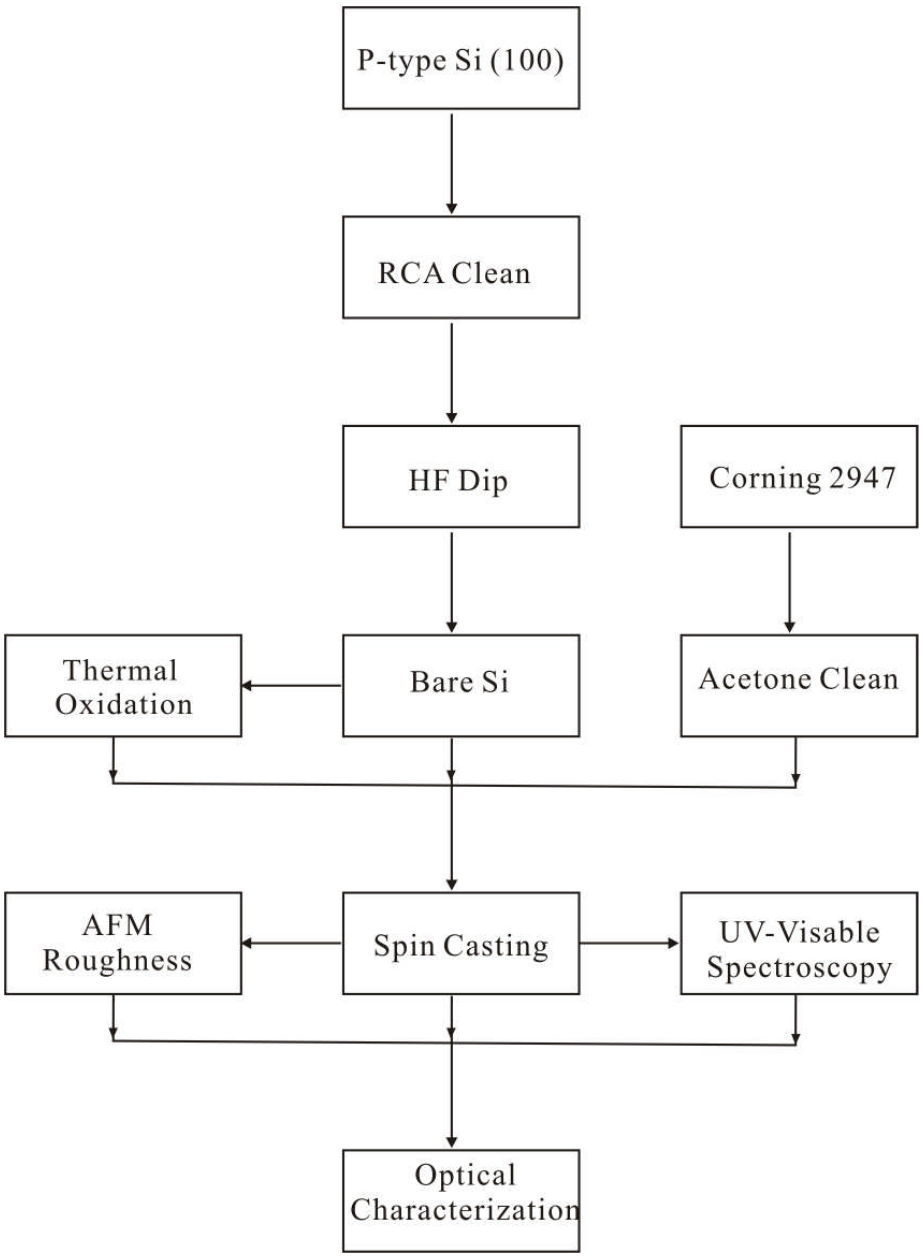

Figure 4.1 Flow chart of experimental procedures.

The substrates included Corning 2947 fused silica, single crystal silicon and SiO_2 coated silicon substrates. All substrates were cleaned prior the deposition. The single crystal silicon substrate was cleaned using the standard RCA procedure followed by a 10 s dip in HF[7] and blown dry in pure nitrogen obtained from boil-off of liquid nitrogen. The SiO_2 substrates were obtained by dry oxidation of the aforementioned cleaned silicon wafers at 1000 °C in a high purity oxygen flow. The Corning 2947 fused silica substrates were cleaned using acetone.

Variable angle spectroscopic ellipsometry over the photon energy range 1.5-4.5 eV in steps of 20 meV was performed in air using a custom made rotating analyzer ellipsometer (RAE). Also used in this study was a J.A. Woollam M88 spectroscopic ellipsometer, and a Gartner single wavelength (λ = 632.8 nm, 1.96 eV) nulling ellipsometer. All ellipsometers have a beam size of several mm in diameter.

As discussed in Chapter 2, Ellipsometry measures the change of the polarization state of the polarized light upon reflection from a surface. The measurables, Ψ and Δ are related to the complex reflection coefficient ρ and Fresnel coefficients $\tilde{R}_p$ and $\tilde{R}_s$ by Equation 4.1:[8]

$$\rho = \frac{\tilde{R}_p}{\tilde{R}_s} = \tan(\Psi)e^{i\Delta} \qquad (4.1)$$

Likewise, the dielectric response function ε, and pseudo dielectric function $<\varepsilon>$, a composite dielectric function of a multi-film stack upon a substrate are both obtained from Equation 4.2:

$$\varepsilon \; or \; \langle\varepsilon\rangle = \varepsilon_1 + i\varepsilon_2 = \sin^2\phi\tan^2\phi\left(\frac{1-\rho}{1+\rho}\right)^2 \qquad (4.2)$$

The parameterization of the optical functions is based on the fact that the dielectric function $\varepsilon(E)$ is related to band-to-band transitions that could be expressed by different oscillators, although it should be pointed out that there is no simple correlation between the energies of optical transitions and oscillator resonance energies in the oscillator model.[9] Because the Visible-Ultraviolet absorption spectra of the films showed multiple adjacent and broad absorption bands, the optical functions for NDA's thin films are simulated by an oscillator model using the combination of Tauc-Lorentzian and Gaussian oscillators. Details of the model will be discussed in the next section and the oscillator model for NDA's thin films uses one Tauc-Lorentzian oscillator and three Gaussian oscillators to yield good fits that are physically consistent with experimental optical absorption results presented below. The quality of the fit of the data to the model is expressed by the mean square error (MSE) as follows:[10]

$$MSE = \frac{1}{2N - M} \sum_{i=1}^{N} \left[\left(\frac{\Psi_i^{\mathrm{mod}} - \Psi_i^{\mathrm{exp}}}{\sigma_{\Psi i}^{\mathrm{exp}}} \right)^2 + \left(\frac{\Delta_i^{\mathrm{mod}} - \Delta_i^{\mathrm{exp}}}{\sigma_{\Delta i}^{\mathrm{exp}}} \right)^2 \right] \qquad (4.3)$$

A MSE value of 0 indicates a perfect correspondence of measured and model calculated results. Another important factor that impacts the fit is the correlation among the parameters. This is particularly problematic when using purely mathematical models. Multiple samples are used to minimize the correlation influence and several other techniques such as manual null ellipsometry and UV-Vis spectra are used to give complementary support to the models used.

A manual nulling ellipsometer equipped with He-Ne laser source is used to determine the film thickness and refractive index at 1.96 eV. The $\Psi - \Delta$ trajectory at this energy is calculated and compared with the RAE results. Ultraviolet and Visible (UV-Vis) absorption

spectra of NDA-n2 thin film in the photon energy range 1.5 – 5.0 eV are obtained from thin film deposited on fused silica slides (Corning 2947) using a Perkin Elmer Lambda 40 UV-Vis spectrometer. The film morphology and surface roughness are determined using atomic force microscopy (AFM). The Bruggeman EMA (BEMA), in which the host material is assigned the dielectric response function of the heterogeneous material in question, is referred to as the self-consistent model and was used to simulate the surface roughness.

The optical properties of NDA-n1 were determined using the same procedure as the aforementioned method. With identical conjugated core group and similar molecular structure, a model with the combination of one Tauc-Lorentzian oscillator and three Gausssian oscillators was proposed to simulate the refractive index of NDA-n1. The optical properties of other two organic dielectrics Polyethylene PE and polyvinylidene fluoride P(VDF-TrFE) are also presented, which would be used for film thickness determination in Chapter 5.

4.3 Results and Discussion

4.3.1 Film Preparation

The NDA's thin films were deposited by solution spin casting using dichloromethane as solvent. The parameters that will affect the film properties include the choice of solvent, the concentration of solution, the spin speed (RPM) as well as the interaction among the polymer, solvent and the substrates. As shown in Table 4.1, a significant difference in the NDA-n2 film thickness was found depending on the substrate being either bare silicon or SiO_2 where the spin casting conditions were otherwise the same (RPM and concentration). The possible reason for thicker films on SiO_2 substrate comes from its higher surface energy

compared with HF-dip Si surface. The surface energy for freshly HF dipped silicon (hydrogen terminated) is significantly smaller than that of SiO_2 as shown in Table 4.2.[11] Therefore the NDA-n2 solution wets the H-terminated Si surface far less than the SiO_2 surface. Considering that for spin casting, only small amount (20 μL) of of NDA-n2 solution was dispensed at the center of the spinning wafer (2 cm^2 area), the NDA-n2-substrate interaction dictates the amount of solution that adheres to the substrate surface and therefore determines the film thickness. The thickness value of SiO_2 does not have to be large, even a thin native oxide (~1 nm), that grows in air after the HF dip increases the NDA-n2-surface energy (hydrophilicity) and permits wetting and thicker polymer films. Another factor that affects the film thickness and uniformity is spin speed, which is also shown in Table 1. In this experiment, spin speed between 3000 and 5000 RPM will get uniform film with appropriate thickness. With spin speed lower than 3000, the film was too rough, while it was too thin if spin speed was higher than 5000 RPM.

4.3.2 Optical Modeling

A representative UV-Vis absorption spectrum of an NDA-n2 thin film deposited on fused silica is shown in Figure 4.2. The solution spectrum obtained in this study is essentially the same as in previous published results[6] and shows substantially the same absorption bands albeit shifted, sharper and more Lorentzian in shape than for the solid film. The absorption at 4.51 eV is attributed to the $\pi - \pi$ band transition associated with the aryl-ether flexible tail, while the absorptions of 3.30, 3.48 and 3.64 eV are from the $\pi - \pi$ transition in the naphthalene-tetracarboxylic diimide conjugated core.

Table 4.1. Concentration, spin speed, and POMA film thickness for silicon and SiO_2 substrates

Spin Speed (RPM)	Substrate	NDA-n2 Thickness (nm)
4000	SiO_2	27.3±1.7
4000	Si	16.2±1.5
3000	SiO_2	36.8±2.2
3000	Si	19.5±1.4
2000	SiO_2	41.5±1.6
2000	Si	22.7±2.1
1000	SiO_2	44.3±1.8
1000	Si	27.9±5.2

Table 4.2. Comparison of surface energies for silicon, SiO_2, and H-terminated silicon

Substrate	Surface Energy (dynes/cm^2)	Surface Energy (Pascal)
Si	1100	110
SiO_2	2000	200
Si H-terminated	27	2.7

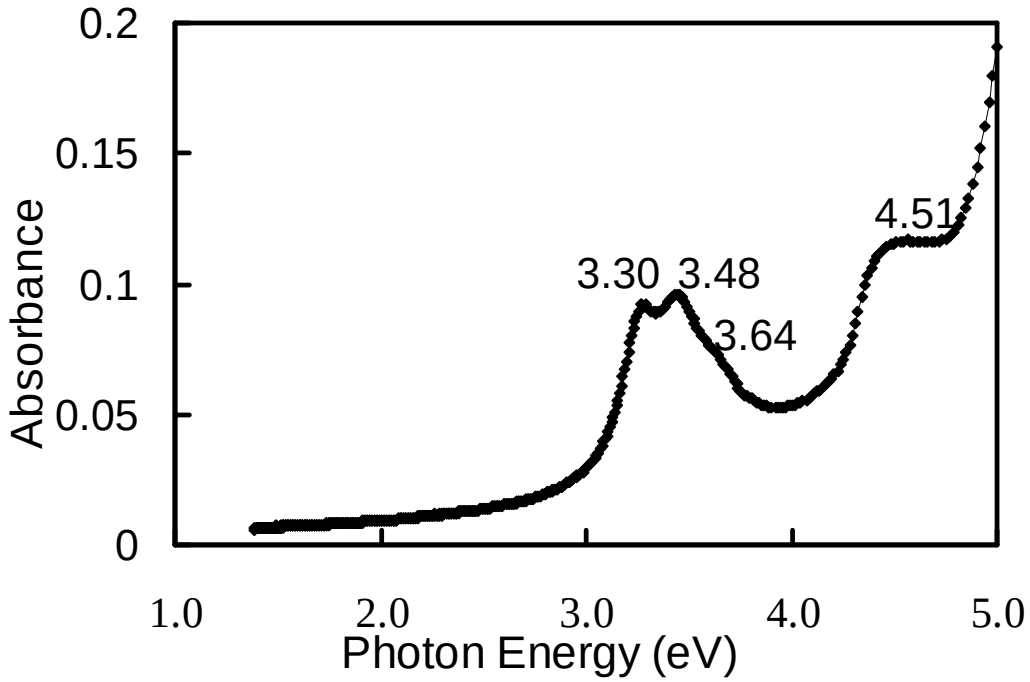

Figure 4.2 UV-Vis Absorption Spectrum of NDA-n2 thin film.

Rather than attempting to obtain *n*, *k* and film thickness *L* directly from a single optical model that includes the above determined optical absorption, our modeling strategy first uses the low optical energy range below 3 eV where $k \approx 0$ to determine the film thickness and refractive index *n*, and then using the *L* determined as input a more general optical model is developed. This strategy reduces the number of unknowns that are to be fitted across the photon energy range studied. For finding *L* a single film model is used with data below 3 eV where the transparent film is approximated using the Cauchy formula of the form:[12]

$$n(\lambda) = A + \frac{B}{\lambda^2} + \frac{C}{\lambda^4} \tag{4.4}$$

where *A*, *B*, and *C* are fitting parameters. In this low photon energy regime the only unknown parameters are the film thickness *L* and the dispersion of the refractive index, $n(E)$ or $n(\lambda)$. The SE data are then sufficient to accurately extract the thickness and refractive index *n* in this transparent region using a nonlinear regression analysis. The values of $n(E)$ from this Cauchy model in the transparent range are shown as the solid line in Figure 4.3.

In order to confirm the results above from the Cauchy model, an accurate single wavelength manual nulling ellipsometer equipped with a quarter wave plate was used to obtain $\Psi - \Delta$ data from multiple NDA-n2 samples. The data are compared with a calculated $\Psi - \Delta$ trajectory shown in Figure 4.4 with the step thickness of 2 nm with *n* at 1.96 eV (632.8 nm) as obtained from the Cauchy model. It is seen that the agreement is visually good, and a quantitative comparison of the thicknesses is given in Table 4.3 which shows better than 10% agreement over the thickness range.

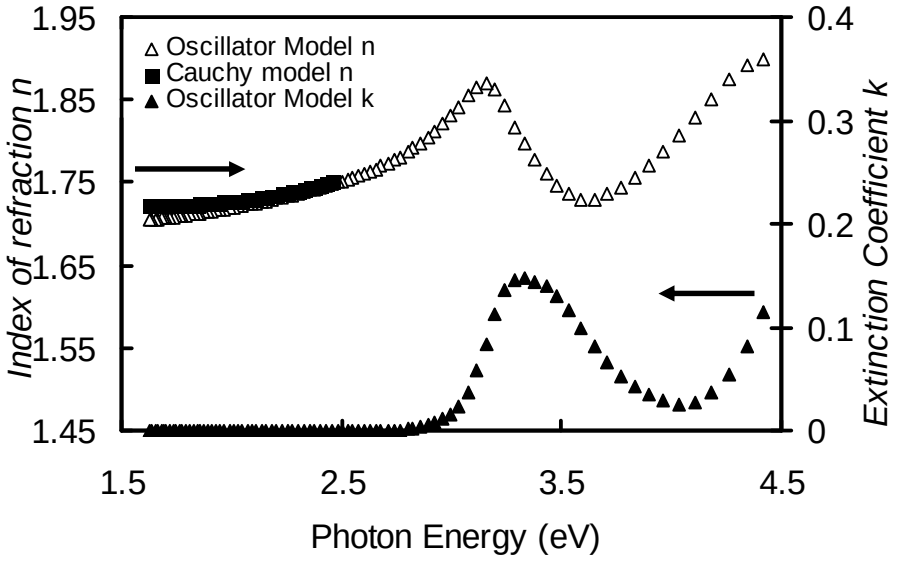

Figure 4.3 Optical properties (*n* and *k*) of NDA-n2 thin film obtained from the Cauchy model in the transparent region along with results from the oscillator model over the entire range.

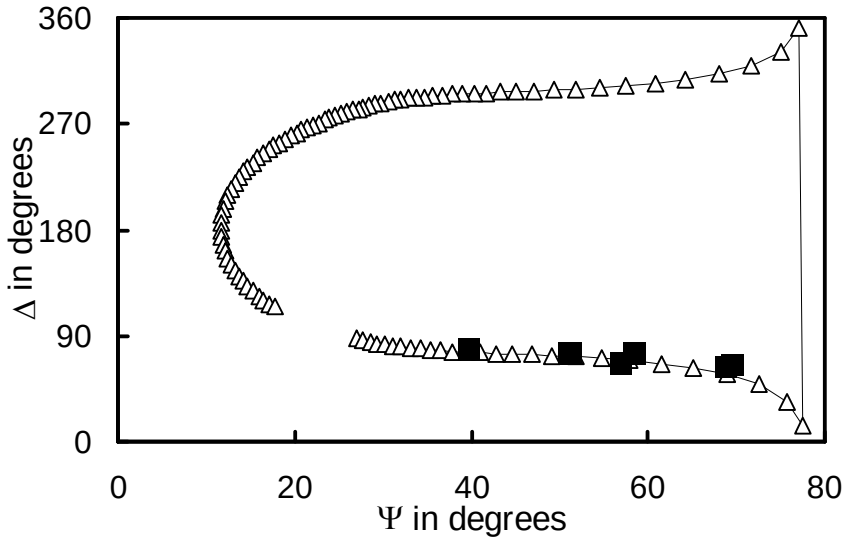

Figure 4.4 Calculated $\Psi - \Delta$ film thickness trajectory ($\phi = 70^{\circ}$, 1.96 eV light, $n = 1.72$, $k = 0$ from transparent region of Figure 4) with data (filled squares) from null Ellipsometry.

The UV-visible spectrum in Figure 4.2 displays one broad band and several adjacent absorbances. Therefore it is reasonable to use Tauc-Lorentzian and Gaussian oscillator model to simulate the optical properties. Tauc-Lorentzian and Gaussian oscillators describe ε_2 with the form given by equations (1) and (2), respectively:[13]

$$\varepsilon_2 = \frac{A(E - E_g)^2}{E^2 - E_c{}^2 + C^2} \tag{4.5}$$

$$\varepsilon_2 = Ae^{-(\frac{E-E_c}{Br})^2} - Ae^{-(\frac{E+E_c}{Br})^2} \tag{4.6}$$

where *A* is the oscillator amplitude, E_c is the resonance energy of the oscillator in eV, *Br* is a broadening term in eV, E_g is the band gap of the film in eV, and *C* is a fitting term in eV. The real part of the dielectric function ε_1 is obtained from ε_2 using the Kramers-Kronig integrals. The use of the Tauc-Lorentzian oscillator was proposed by Jellison *et al*[13] and is suitable for the interpretation of interband absorption of amorphous thin films. Gaussian oscillators are used for the simulation of broad band absorptions. In order to cover the entire photon energy range investigated using SE and to be consistent with the measured absorption spectrum, an oscillator model with a Tauc-Lorentzian oscillator and three Gaussian oscillators was chosen. With the thickness determined using the Cauchy model, approximate optical constants are obtained over the entire energy range including both the transparent and absorption regions using a point by point fit from the lowest photon energy to the highest photon energy. Then the oscillator model mentioned above is used to refine the optical constants and insure Kramers-Kronig consistence in the refined optical constants. The parameters for the four oscillators for the oscillator model are given in Table 4.4, where the each fitting parameter has been defined above using Equations 4.5 and 4.6.

Table 4.3 $\Psi - \Delta$ from Cauchy model and thickness from Cauchy model and $\Psi - \Delta$ trajectory

Ψ(°)	Δ(°)	Thickness (nm)	
		Cauchy Model	Trajectory
39.58	78.91	25.1	25.8
50.98	76.13	31.4	34.5
58.38	76.10	39.2	40.1
68.81	71.06	45.8	47.2
69.45	64.03	54.0	50.3

Table 4.4 Parameters of Tauc-Lorentzian oscillator and Gaussian oscillators used for the oscillator model

	A	E_c (eV)	Br (eV)	C (eV)	E_g (eV)
Tauc-Lorentz Oscillator	4.0691	3.2179		0.2964	2.716
Gaussian Oscillator 1	0.15028	3.4306	0.3311		
Gaussian Oscillator 2	0.15695	3.5273	0.62352		
Gaussian Oscillator 3	0.69332	4.6735	0.57374		

The optical properties (*n* and *k*) are shown in Figure 4.3. An example of the use of this oscillator model with an independent NDA-n2 sample is shown in Figure 4.5 with data well fit by the model and a low MSE value of 5. The resonance energies of the Tauc-Lorentzian oscillator and three Gaussian oscillators are at 3.21, 3.43, 3.52, and 4.67 eV, respectively with the lower energy oscillator most likely corresponding to the $\pi - \pi$ band transition in the naphthalene-tetracarboxylic diimide conjugated core, and the band transition associated with the aryl-ether flexible tail. The higher energy oscillators may include characteristic functional group transitions and also the high energy continuum associated with the conduction band of solids. Thus the high energy oscillators are not directly related to specific molecular structural characteristics. The refractive index *n* obtained from Cauchy model and Oscillator model are compared in the transparent region in Figure 4.3 with the largest difference of about 0.017, indicating that the Cauchy and Oscillator model agrees well in their overlap spectral regions.

4.3.3 Film Roughness

The film surface morphology was examined using AFM. Figure 4.6a and b is an AFM image of SiO_2 substrate prior film deposition and the NDA-n2 thin film with the 1×1 μm^2 scan size and 10 nm/div in z direction. It shows that the spin coated NDA-n2 films displays RMS surface roughness of about 0.25 nm, which is less than 1% of the total thickness of the thin film, and indicates that surface roughness will exert little influence on the film optical properties. This conclusion is also verified by the use of a Bruggeman effective medium approximation (BEMA) layer that accounts for the surface roughness.

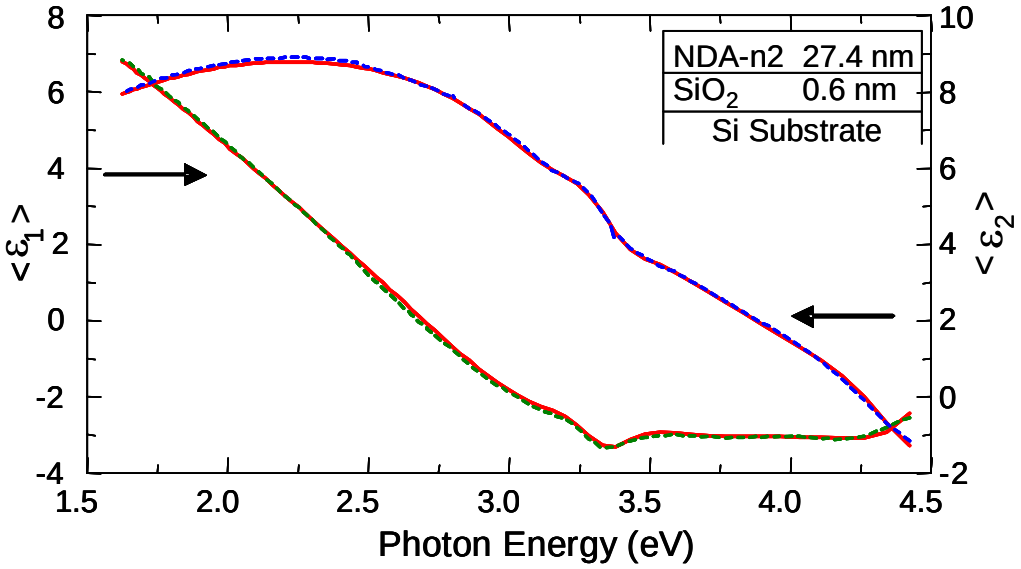

Figure 4.5 Fit of NDA-n2 thin film on single crystal silicon substrate data to the oscillator model for NDA-n2. The inset displays the film structure and thickness obtained from the fit.

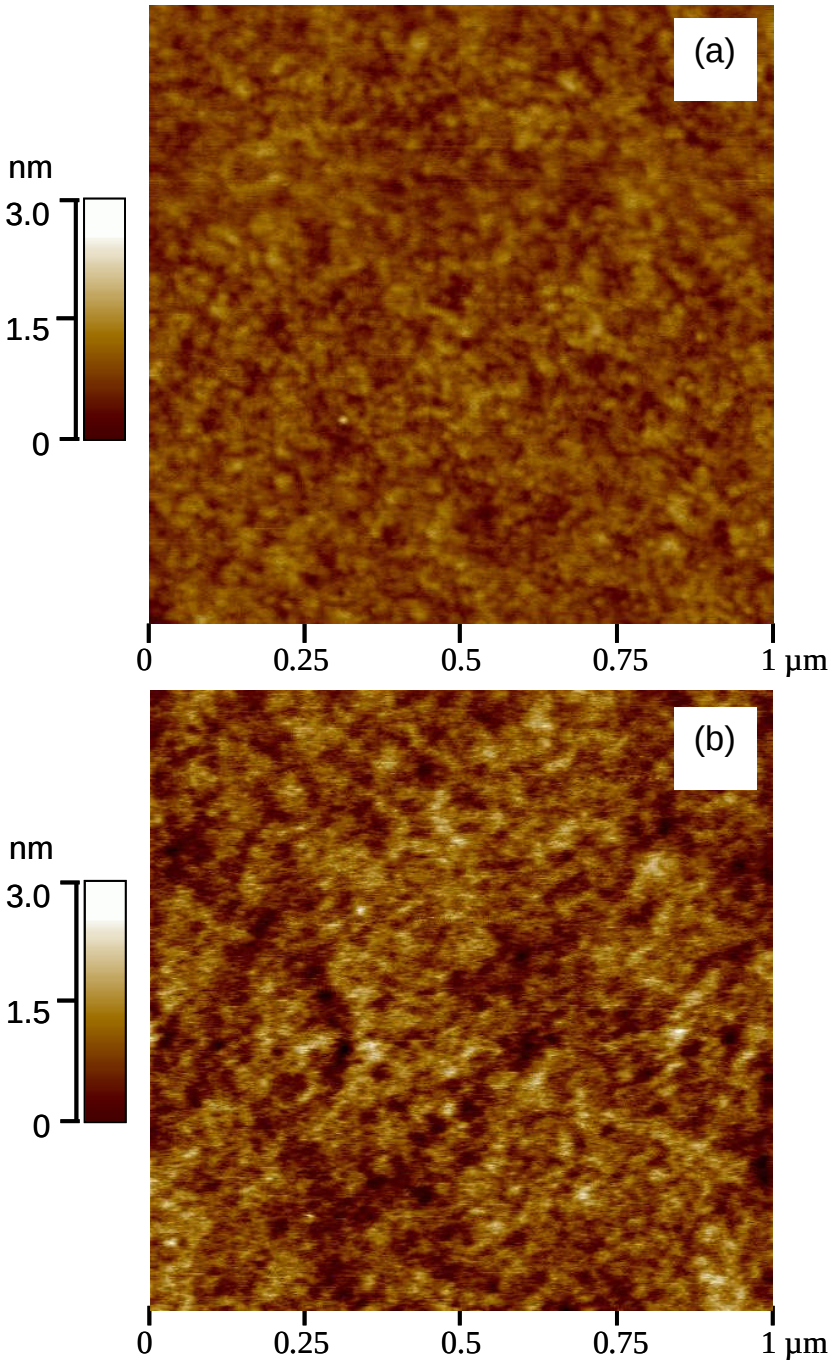

Figure 4.6 AFM image of (a) SiO_2 substrate prior deposition, RMS roughness = 0.14 nm, and (b) NDA-n2 thin film, RMS roughness = 0.25 nm.

The AFM roughness data was incorporated into our optical model as a BEMA layer, which is shown in Figure 4.7a. With the added BEMA layer, the new optical system is used to see whether the fit accuracy can be improved, where Fig. 4.7b is the obtained Tauc-Lorzentizan and Gaussian oscillator model without the BEMA layer. With the respective MSE values of 5 and 4 being almost the same, it is concluded that the roughness layer does not need to be included in the optical properties determination. Here a short summary is that very smooth films can be prepared by solution spin casting, which will be crucial for the OTFT device fabrication.

4.3.4 Optical Anisotropy

It has been reported for a number of spin cast polymer films that the polymer chains lie in the plane of the film and lead to optical anisotropy[14,15] as depicted in Fig. 4.8. While in the present study we are not dealing with polymer films it is possible that the NDA-n2 molecules are oriented and lead to optical anisotropy.

Possible NDA-n2 film in-plane anisotropy was investigated using SE by rotating the sample in the plane of the film and the SE data was obtained at the same angle of incidence and on the same spot on the film. The result is shown in Fig. 4.9, where the sample was rotated to three angles (0°/60°/150°) at the incidence angle $\phi = 70^{\circ}$. The three sets of nearly identical data indicate that there is no significant in-plane anisotropy. The molecules in the plane of the film are essentially randomly arranged.

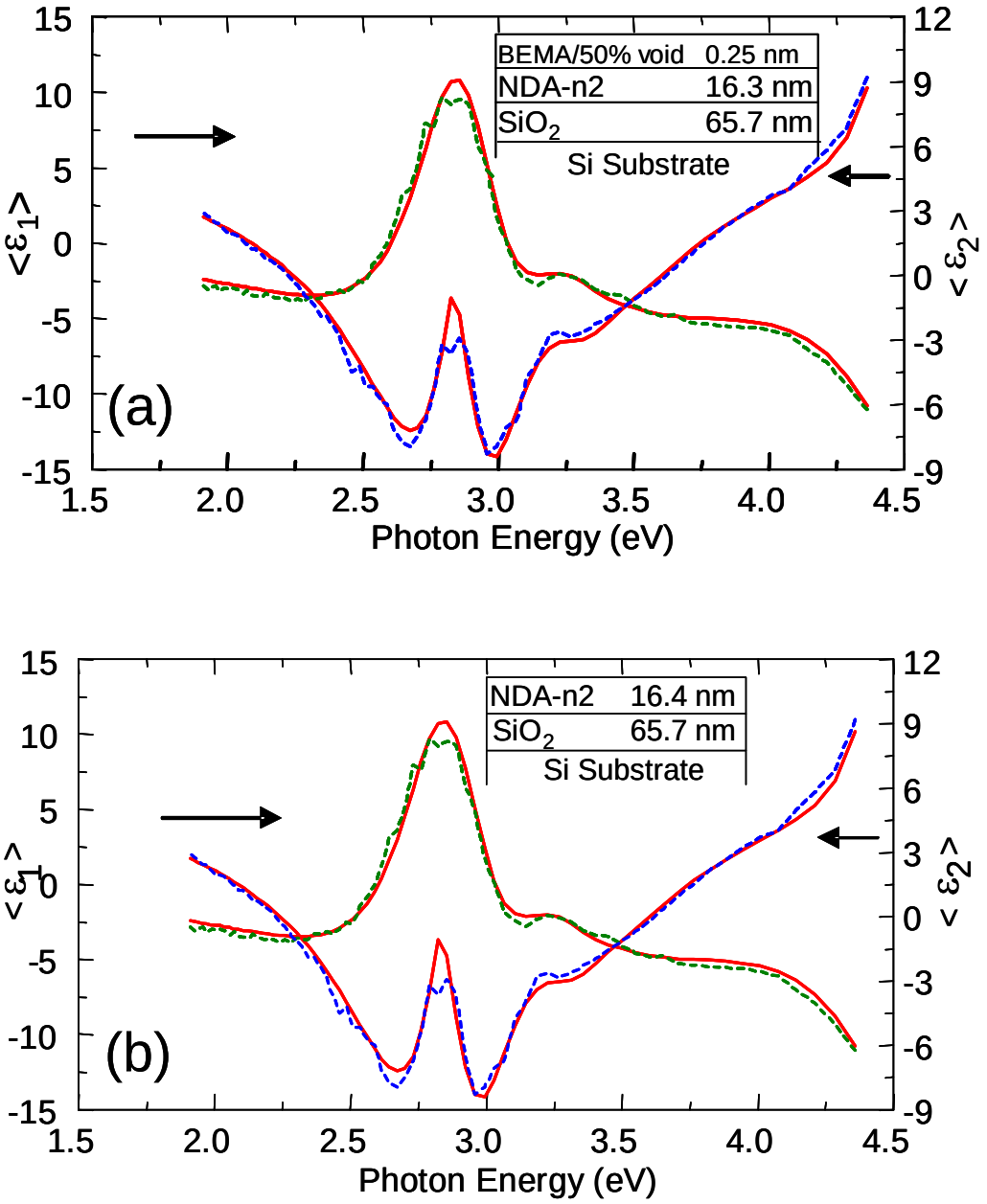

Figure 4.7 NDA-n2 thin film on SiO_2 substrate using oscillator model (a) with and (b) without BEMA layer. The insets display the film structure and thickness obtained from the fit.

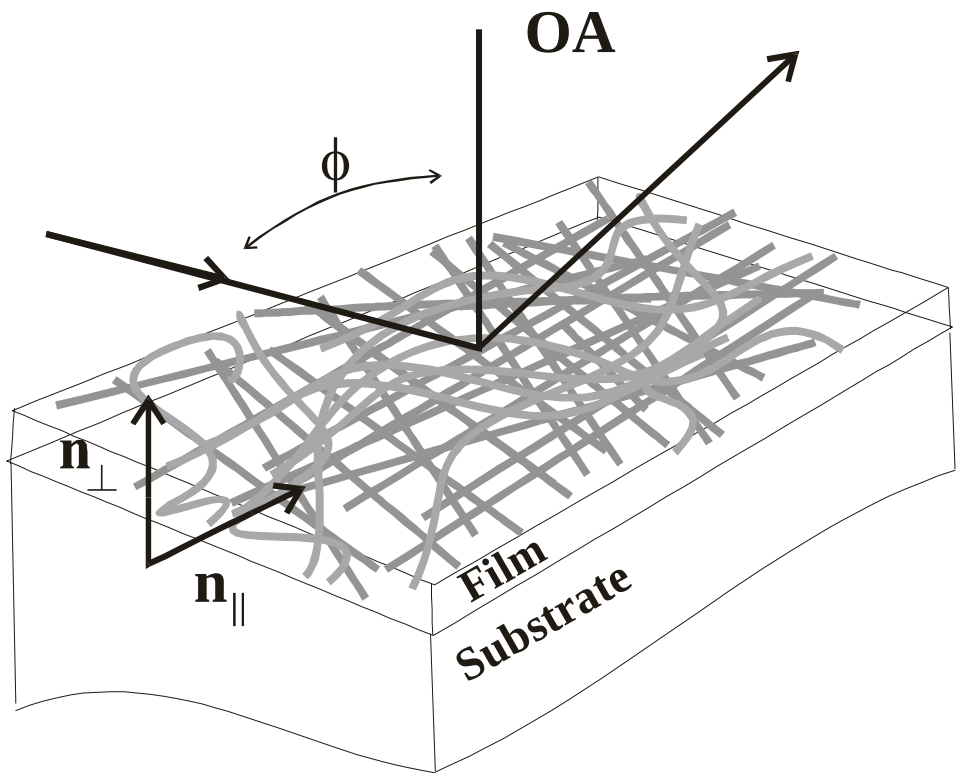

Figure 4.8 Schematic of uniaxial anisotropic polymer film: OA is the optic axis, $n_{\perp}$ and $n_{//}$ are the out of plane and in plane refractive indices, respectively.

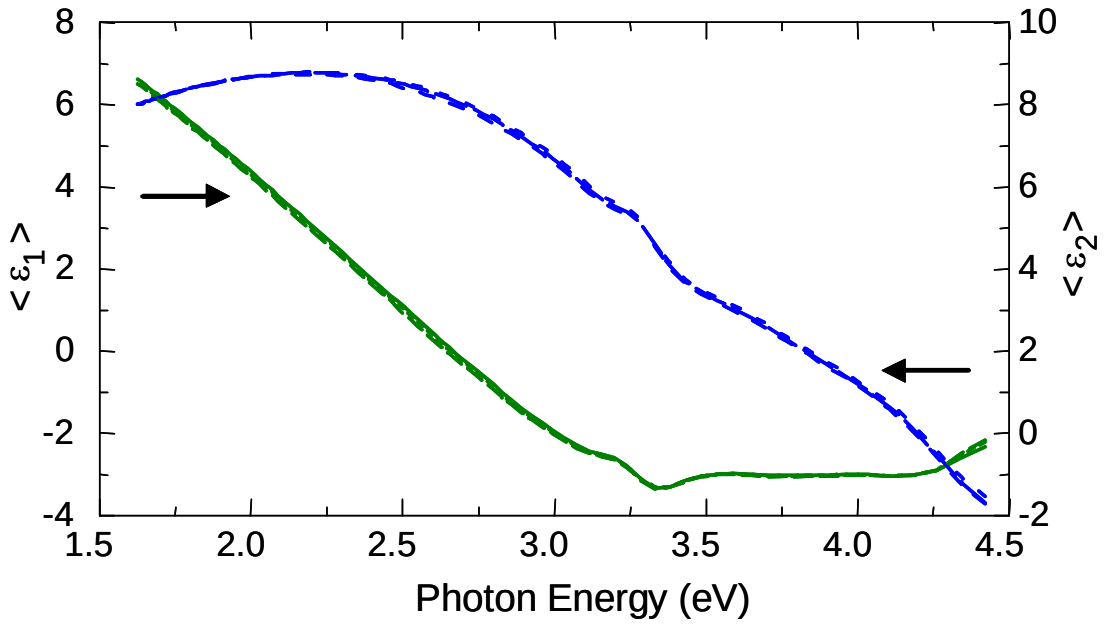

Figure 4.9 Results of in plane sample rotation at 0°, 60°, 150°.

To resolve any out of plane anisotropy, the Ψ and Δ data were obtained using SE at ϕ of 65°, 70° and 75°. In order to determine whether the sensitivity of SE was suitable in the ϕ range used, $\Psi - \Delta$ trajectories at these three angles were calculated using the oscillator model described above at the mid range photon energy of 1.96 eV and is shown in Fig. 4.10. The trajectories show good sensitivity over the three ϕ used in this study. The SE data obtained at each ϕ were fit to the single film model discussed above and shown in the inset in Fig. 4.11, and also shown in the Figure are the resulting *n*'s and *k*'s at each ϕ. The small and non-systematic differences in *n* and *k* indicate that there is no significant out of plane optical anisotropy in the spin cast NDA-n2 film.

An explanation for the lack of significant difference in *n* and *k* at lower energies and within 10° change in ϕ could be due to small molecular weight and the film thickness. As NDA-n2 is a small molecular organics, its short chain is less likely to be influenced by the forces exerted on them during spinning. In the literature, only polymers with very high molecular weight exhibit prominent anisotropy.[16]

4.3.5 Optical Properties of NDA-n1

We already discussed the optical characterization of NDA-n2 thin films in details. In this section the optical properties of NDA-n1 films will be summed in comparison with NDA-n2. Figure 4.12 is UV-Vis spectrum for NDA-n1 and NDA-n2 films, where the films were spin cast on fused quartz substrate at 3000 rpm and the solutions were 0.15% in dichloromethane.

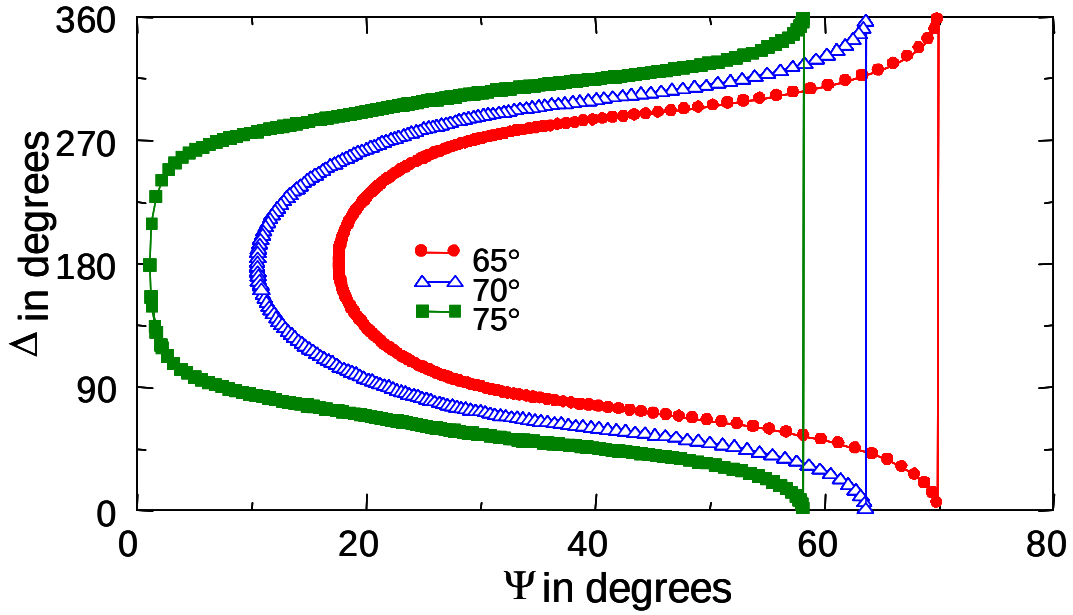

Figure 4.10 Calculated $\Psi - \Delta$ trajectory for NDA-n2 of varying thickness on a Si substrate at multiple angles at 1.96 eV with *n*, *k* values supplied from the oscillator model.

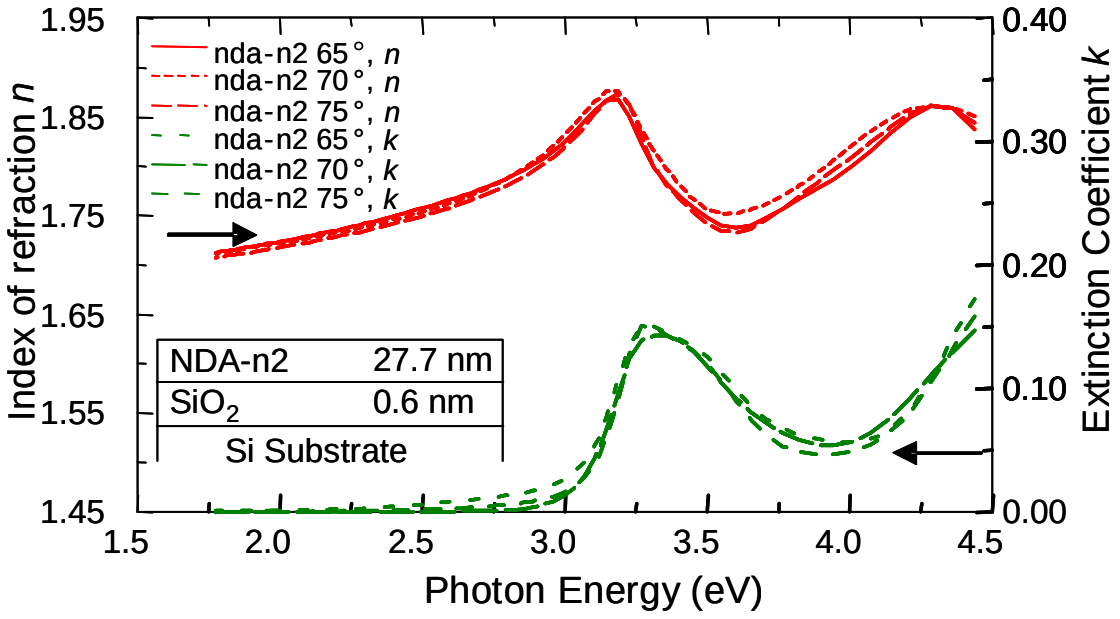

Figure 4.11 Optical properties (*n* and *k*) for NDA-n2 at multiple incident angles. The inset displays the film structure and thickness obtained from the fit.

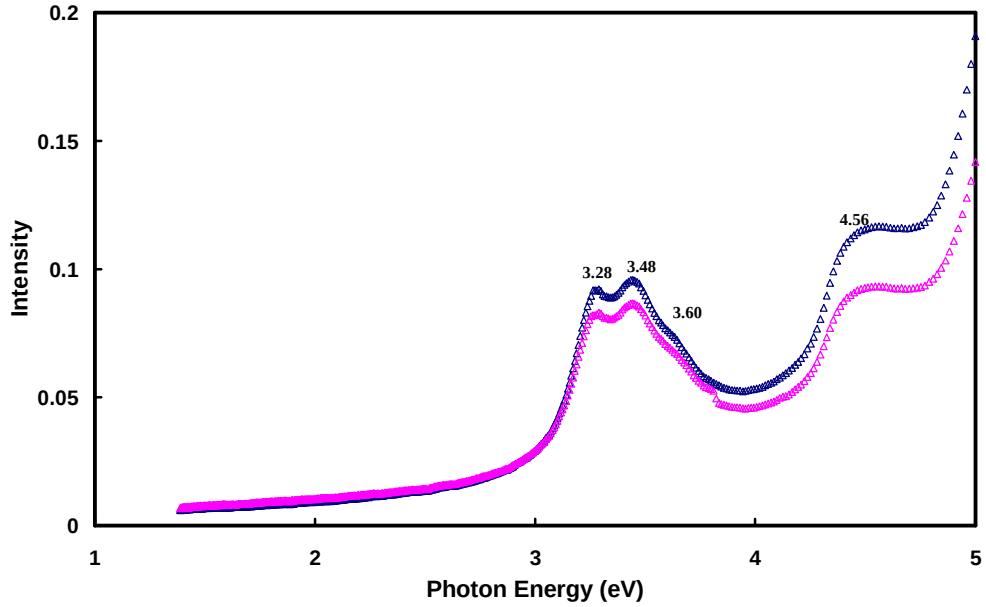

Figure 4.12 UV-Vis spectrum of NDA-n1 and NDA-n2 film on fused quartz substrate.

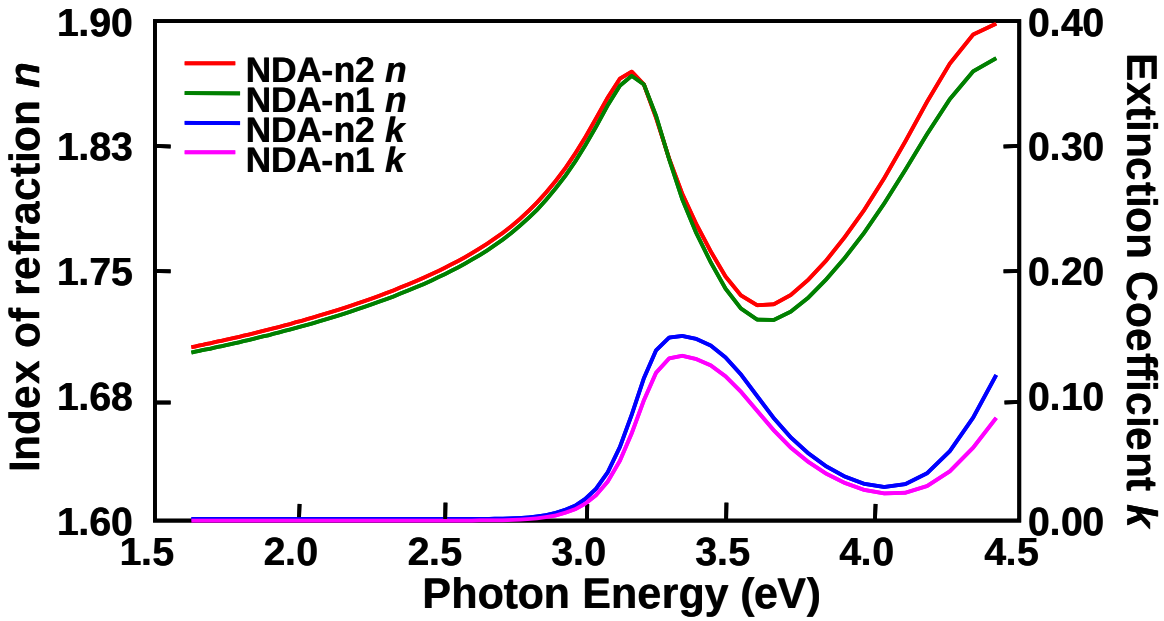

Figure 4.13 Refractive index (*n* & *k*) of NDA-n1 and NDA-n2 extracted from SE measurement.

The absorbance for NDA-n1 at high energy (4.56 eV) was much weaker than that of NDA-n2 while the difference of absorbances at low energy was not so obvious. As discussed in Section 4.3.1 for NDA-n2 film, the absorbance at 4.56 eV was from aryl-ether flexible tail. NDA-n2 has a longer aryl-ether chain and correspondingly there has stronger absorbance. Because of the identical conjugated core group and similar molecular structure, the absorbances around 3.5 eV is almost the same. The optical properties of NDA-n1 films were then extracted from SE measurement. The same Tauc-Lorentzian oscillator and Gaussian oscillator model was proposed to fit SE result. The obtained refractive index (*n* & *k*) is shown in Figure 4.13 together with that of NDA-n2. Only some small shifts in absorbance and film densification are found. As good fit was made for this model and agreed well with the structure information, this model is believed to reflect the physical truth and will be used for NDA-n1 film thickness determination.

4.3.6 Optical Properties of PE and P(VDF-TrFE)

In the next Chapter, two polymeric gate dielectrics polyethylene PE and polyvinylidene fluoride P(VDF-TrFE) will be used for device studies. Here we briefly introduced the optical properties of these two spin-cast films, which would be used for film thickness determination. The optical properties of PE and P(VDF-TrFE) were characterized and modeled using Cauchy model (Equation 4.4) as no apparent absorbance was observed during transmission UV-Vis spectroscopy of the film on fused quartz substrate. The extracted optical properties (refractive index) are given in Figure 4.14 a and b for PE and P(VDF-TrFE), respectively.

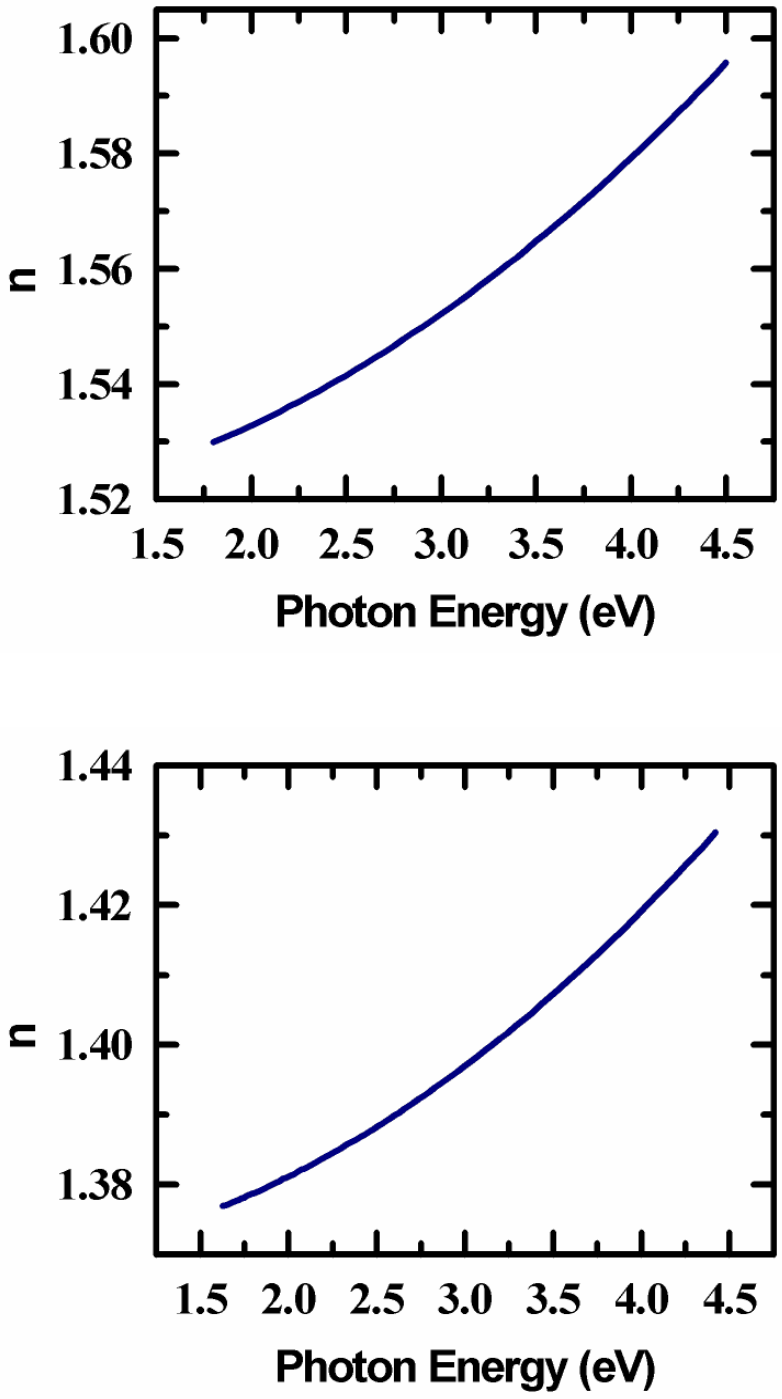

Figure 4.14 Extracted optical properties (here refractive index n) of (a) PE where extinction coefficient $k = 0$, and (b) P(VDF-TrFE) where $k = 0$.

4.4 Conclusions

The optical functions of NDA's thin films were determined using variable angle spectrocopic ellipsometry. A Tauc-Lorentzian and Gaussian oscillator model was used to yield a good regression analysis fit and the optical properties obtained from the model are consistent with independent optical absorption measurements and are Kramers-Kronig consistent. Spin casting the NDA's films resulted in smooth optically isotropic films, which would be crucial for the fabrication of OTFT devices.

4.5 References

1. H. Lin, C. Lin, H. Chang, Y. Lin, C. Wu, J. Appl. Phys., **95**, 881 (2004).

2. W.M.V. Wan, R.H. Friend, N.C. Greenham, Thin Solid Films, **363,** 310 (2000).

3. N.C. Greenham, R.H. Friend, D.D.C. Bradley, Adv. Mater., **6**, 491 (1994).

4. S.M. Pyo, S.I. Kim, T.J. Shin, Y.H. Park, M. Ree, J. Polym. Sci.: Part A: Polym. Chem., **37**, 937 (1999).

5. H.E. Katz, A.J. Lovinger, J. Johnson, C. Kloc, T. Siegrist, W. Li, Y.Y. Lin, A. Dodabalapur, Nature, **404**, 478 (2000).

6. T.J. Dingemans, S.J. Picken, N.S. Murthy, P. Mark, T.L. StClair, E.T. Samulski, Chem. Mater., **16**, 966 (2004).

7. S. Wolf, R.N. Tauber, *Silicon Processing for the VLSI Era*, (Lattice Press, Sunset Beach, CA, 1990).

8. H.G. Tompkins, *A User's Guide to Ellipsometry*, (Academic Press, San Diego, CA, 1993).

9. M. Losurdo, G. Bruno, E.A. Irene, J. Appl. Phys., **94**, 4923 (2003).

10. A.H. Mueller, N.A. Suvorova, E.A. Irene, J. Appl. Phys., **93**, (2003).

11. F. Fowkes, *Contact Angle Wettability and Adhesion*. American Chemical Society: Washington DC, 240 (1964).

12. F.L. Pedrotti, L.S. Pedrotti, *Introduction to Optics*, (Prentice Hall, Upper Saddle River, NJ, 1993).

13. G.E. Jellison, F.A. Modine, Appl. Phys. Lett., **69**, 371 (1996).

14. Y. Geng, S.W. Culligan, A. Trajkovska, J.U. Wallace, S.H. Chen, Chem. Mater. **15**, 542 (2003).

15. H.J. Egelhaaf, J. gierschner, D. Oelkrug, Synth. Met. **83**, 221 (1996).

16. U. Zhokhavets, G. Gobsch, H. Hoppe, N.S. Sariciftci, Synth. Met. **143** (1), 113 (2004).

CHAPTER 5 – CHARACTERIZATION AND OPTIMIZATION OF NDA'S BASED THIN FILM TRANSISTORS

5.1 Introduction

In Chapter 3 many details about organic thin film transistors (OTFT's) were discussed. The inherent advantages of the organic devices are their ease and low cost of fabrication, and the possibility for use with flexible and large area substrates. The OTFT is therefore an important device for organic electronics, and the device performance primarily depends on the charge carrier mobility. At present, the main limitations for widespread application of OTFT technology are their low charge carrier mobility and the difficulty in developing stable N-channel devices. Recorded OTFT mobilities are generally several orders of magnitude lower than that for single crystalline Si, Ge, and GaAs.[1] For example the highest reported mobility for organic semiconductors is 10 $cm^2V^{-1}s^{-1}$ for pentacene at 17 K while 1400 $cm^2V^{-1}s^{-1}$ for electrons in crystal silicon at room temperature. The charge transport in OTFTs depends on the degree of ordering of the molecules and/or polymer chains in the solid state, the grain boundaries, and the density of defects that are present in the system. The structural or energetic disorder in amorphous organic films severely restricts the charge movement in OTFT as charges are not delocalized.[2] In this way, charge transport

is governed by "hopping" of charge carriers between localized potential wells in response to an electric field.[3] A variety of factors and preparation conditions will affect the mobility of charge carriers and performance. On the other hand, the use of complementary logic elements (requiring both N and P-channel devices) is expected to be crucial to achieving low-power, high-speed performance. Stable organic P-channel semiconductors are easily available, but practically organic semiconductor materials that yield useful N-channel OTFT's have proved difficult to develop, reflecting the unfavorable electrochemical properties of known, electron-demanding organics. Low molecular weight naphthalenetetra-carboxylic diimide derivatives have been reported as stable N-type organic semiconductors.[4] The solubility of the derivatives enables spin casting film preparation and simplifies the fabrication of OTFT's.

The overall device performance of an OTFT critically depends on the properties of the gate dielectric.[5] The polar Si-OH bonds typically found on the surface of SiO_2 quench electrons in the conduction channels.[6] Polymeric insulators have been used as gate dielectrics in OTFT's. These polymeric materials can be solution processed and make smooth films on slica substrates. Detailed studies have shown that the first few monolayers of organic semiconductors on polymeric dielectrics are highly ordered and therefore can allow high field effect mobility.[7,8] Therefore the choice of the gate insulators has become a crucial step in OTFT device fabrication.

In this Chapter, the fabrication of NDA's based OTFT is described and the device performance was characterized and optimized. The optical properties of NDA's films were investigated in Chapter 4. The reasons for choosing NDA's were their high chemical stability, easy solution processability and possible N-channel operation. We have selected

three gate dielectrics with different dielectric constants for OTFT's, and also considered post fabrication treatments such as annealing to improve the mobility of OTFT's.

5.2 Experimental Procedures

Device fabrication began with heavily doped silicon wafers that serve to support the device and to act as the gate electrode for the OTFT's. After the standard RCA clean procedure[9] followed by a 10-s dip in HF in water solution (47% HF) the silicon substrates were blown dry in pure nitrogen obtained from boil-off of liquid nitrogen. After cleaning the silicon wafers to be used for OFET's with SiO_2 as the gate dielectric were oxidized at 1000 °C in a high-purity oxygen flow. The source and drain electrodes were deposited by Au evaporation using a line pattern mask. The channel length L is 75 μm and the channel width W is 5 mm, giving a W/L ratio of 67. The thickness of gold lines was around 200 nm. The NDA films were spin cast from solutions that were 0.15% by weight using dichloromethane as the solvent and at spin speeds of about 3000 rpm for all NDA films. Two polymeric insulators, polyethylene (PE) with static dielectric constant $K = 2.3$ and polyvinylidene fluoride (P(VDF-TrFE)) with $K = 7.5$, were selected to replace SiO_2 as the gate dielectric layers. The molecular structure of PE and P(VDF-TrFE) are shown in Figure 5.1b and c, respectively. Both PE and P(VDF-TrFE) are insoluble in dichloromethane, the solvent used for NDA spin casting. The solvent used for PE was decahydronaphthalene (98%, mixture of *cis* and *trans*) and the solution weight concentration was 2% that was made by heating to 110 °C and spin cast at room temperature at 3000 rpm. Because no smooth film could be made for PE on bare silicon, the film was prepared on a 0.7 nm SiO_2 substrate. P(VDF-TrFE) films were spin cast using methylethylketone (MEK) as solvent. The weight concentration

was 2% and the film was spin cast in a N_2 hood in 20% humidity. The fabricated OTFT structures are shown in Figure 5.2, where it is seen that the inverted gate structure was used and (a) has bottom source and drain contacts and (b) displays top source and drain contacts. Figure 5.2c is a top view of top-contact OTFT and show the indication of W and L. A custom-built probe station using HP 4284A and Keithley 236 was employed for the steady-state electronics measurements. The devices were annealed in a temperature controllable high vacuum system Figure 5.3 to study the temperature effects. Together with the system is a self-assembled rotation analyzer ellipsometer for in-situ measurement to obtain the change information of film thickness and optical properties. The thickness of the gate dielectrics and the NDA's films on top of the dielectric layers were measured by spectroscopic ellipsometry (SE). In Chapter 4 and in a published study[10] the spin cast process and the optical properties for NDA's films were reported.

The thermogravimetric analysis (TGA) of NDA-n1 was carried out using TA instruments high resolution thermogravimetric analyzer model 6220. TGA measures changes in weight of a sample with increasing temperature. Moisture content and presence of volatile species can be determined. Once the temperature range of thermal stability of the NDA-n1 was determined, the annealing of NDA-n1 films was carried out in the vacuum chamber with *in-situ* ellipsometry capabilities shown in Figure 5.3. During annealing, the NDA's films were exposed to various temperature settings and for various durations at 10^{-6} Torr. The SE measurements were carried out during the annealing process to obtain change in film thickness and optical properties of NDA's films.

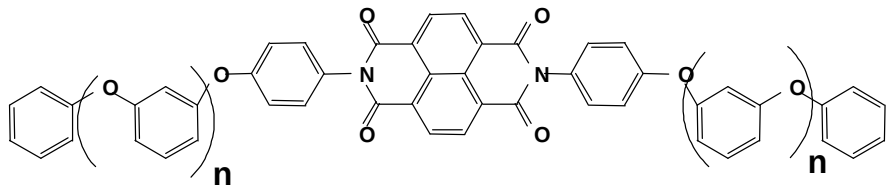

(a)

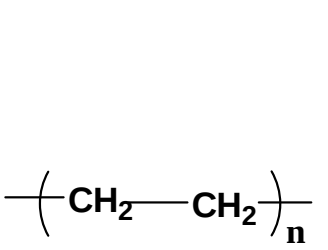

(b)

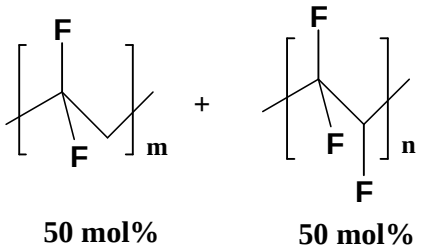

(c)

Figure 5.1 Molecular structures of (a) NDA, where n=1, called NDA-n1, n=2, called NDA-n2, (b) polyethylene (PE), and (c) P(VDF-TrFE).

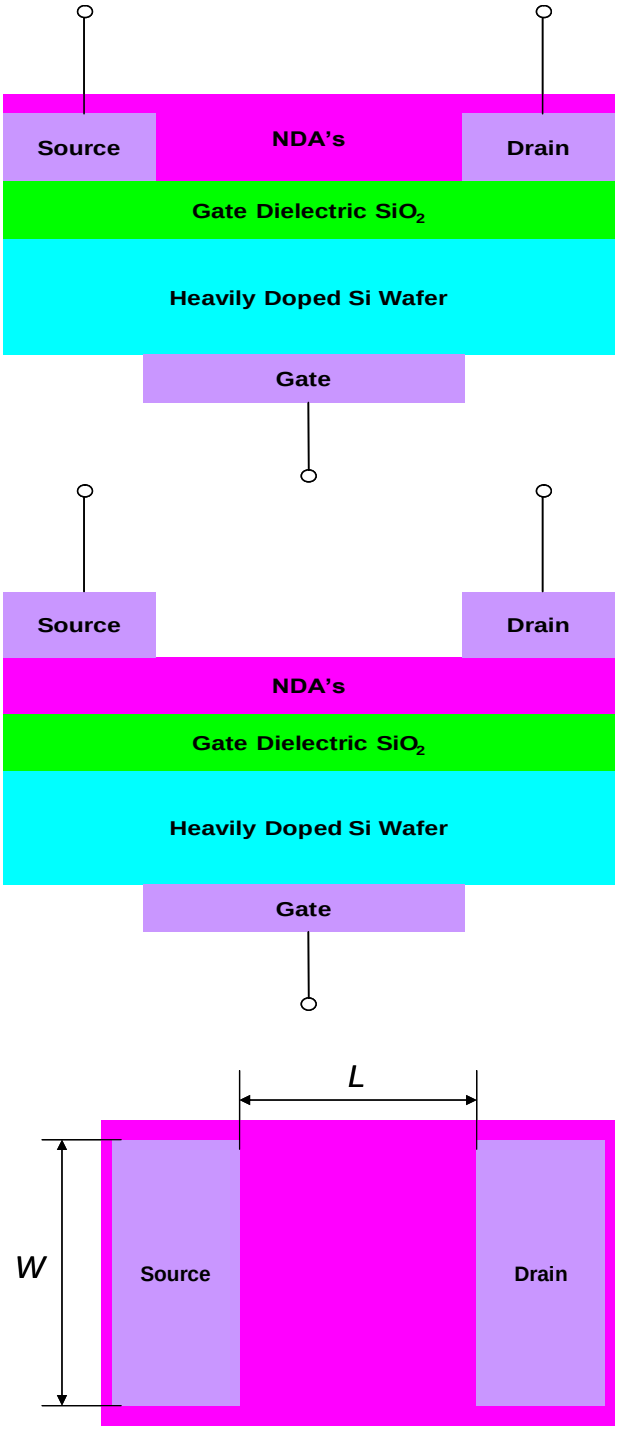

Figure 5.2 (a) Cross section view of the bottom-contact OTFT, (b) cross section view of top-contact OTFT, and (c) top view of gold line patterns used in this study where *L* is the channel Length 75 μm and *W* is the channel width 5 mm.

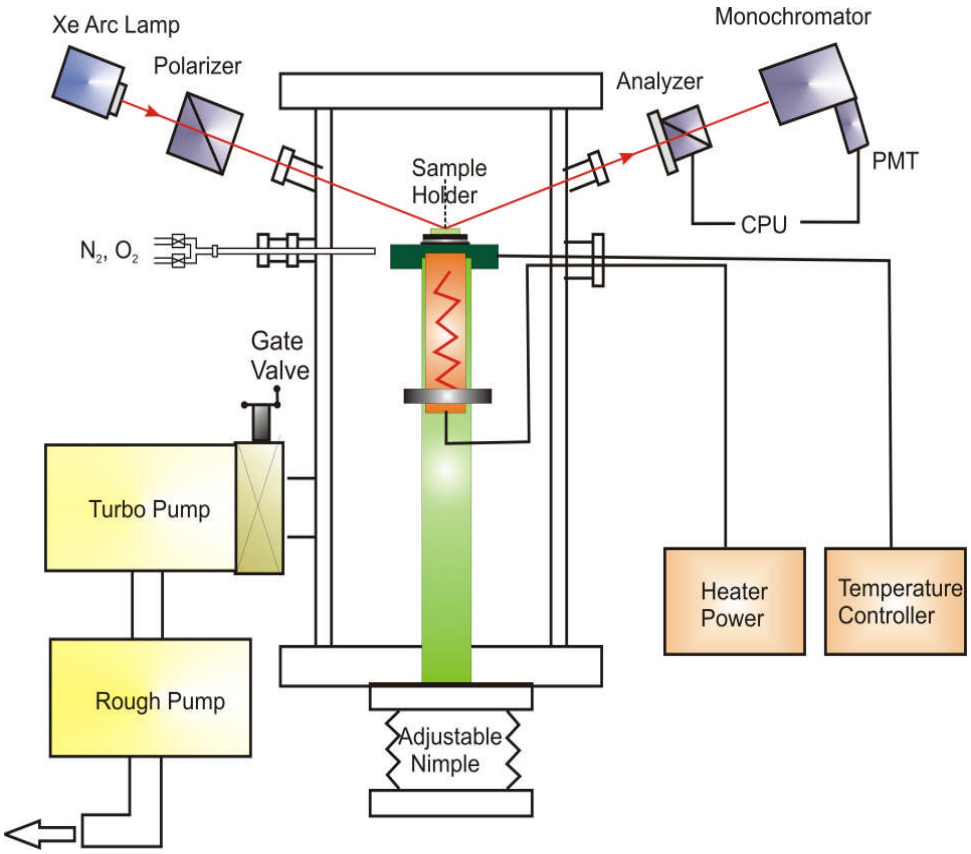

Figure 5.3 Custom built vacuum chamber with *in-situ* ellipsometer for annealing experiments.

5.3 Results and Discussions

5.3.1 OTFT with SiO_2 Gate Dielectric Layer

The channel type of NDA's films was first determined using the bottom contact inverted gate OTFT shown in Figure 5.2a. The transfer characteristic plots for NDA-n2 and NDA-n1 with a 110 nm SiO_2 are shown in Figure 5.4a and b, respectively. The measurements were carried out in laboratory ambient in ascending V_G mode with an integration time of 1 s by averaging 5 data points. Though still in the linear region, both devices increased source to drain current I_{SD} when gate potential V_G was negative and became larger as V_G increased. It can be concluded that both NDA-n1 and NDA-n2 exhibit P-channel semiconducting properties. This is opposite to the report by Katz et. al.,[4] where their organic material in a similar device with the same functional group was N-channel. Specifically the NDA compounds used in the present study have the same naphthalene based conjugated functional group and the aryl-ether group was used to replace those fluorinated terminal groups used by Katz et al. It can also be seen that significantly different I_{SD} values are obtained for the two devices: I_{SD} for NDA-n1 in the range of 10^{-8} A and NDA-n2 is in the range of 10^{-10} A, i.e. with shorter side chains NDA-n1 based OTFT exhibits two orders of magnitude higher current than NDA-n2 while the device dimensions are almost the same. The carrier mobility in the linear region can be calculated by Equation 5.1:[11]

$$\mu(V_G) = \frac{L}{WC_{Die}V_{SD}}\left(\frac{\partial I_{SD}}{\partial V_G}\right) \qquad (5.1)$$

where C_{Die} is the capacitance of gate dielectric and all other terms are already discussed previously. The calculated mobilities for NDA-n1 and NDA-n2 are 10^{-3} and 10^{-7} $cm^2V^{-1}s^{-1}$, respectively, which are given in Table 5.1 and thus there is a four-order of magnitude

difference. It meant that charge carriers moved much faster in NDA-n1 film. As said NDA-n1 has shorter flexible tail group compared with NDA-n2, so it should be the aryl-ether group that makes charge carrier movement more difficult.

The devices were then annealed in a 10^{-6} Torr vacuum system at 60 °C for 3 h. Improved performance was obtained for both devices. Figure 5.5a and b show the transfer characteristics for both devices after annealing. Higher currents and larger slopes for I_{SD}-V_G were obtained. The mobility in the linear region was calculated using Equation 5.1 again and was 10^{-2} $cm^2V^{-1}s^{-1}$ for NDA-n1 and 10^{-3} $cm^2V^{-1}s^{-1}$ for NDA-n2 (Table 5.1). Annealing improved the charge carrier mobility by 3 orders for NDA-n2 and 1 order for NDA-n1, respectively. However, the mobility for NDA-n1 based OTFT is still two orders of magnitude higher than that for NDA-n2 based OTFT. As discussed above, the shorter aryl-ether tail group of NDA-n1 helped the charge movement in the conducting channel formed along the interface. Details of the annealing effects will be discussed in next section. As NDA-n1 based OTFT showed better device performance compared with NDA-n2 based OTFT, the later experiments were primarily based on NDA-n1.

Table 5.1 Mobilities for NDA's based OTFT with SiO_2 gate dielectric.

Organics Semiconductor	Mobility ($cm^2V^{-1}s^{-1}$)	
	As-deposited	Annealed
NDA-n1	10^{-3}	10^{-2}
NDA-n2	10^{-7}	10^{-4}

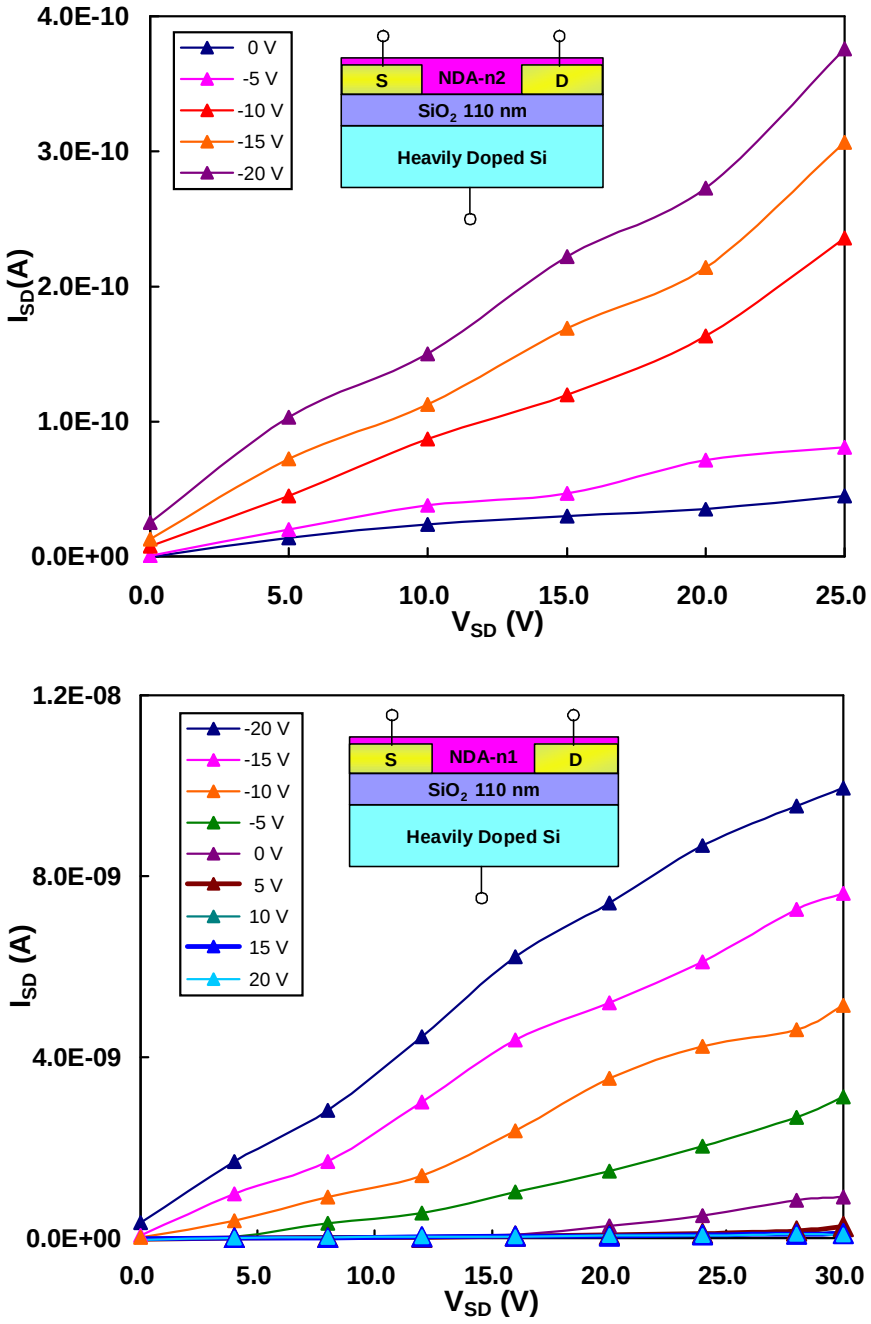

Figure 5.4 Transfer characteristics for device with (a) NDA-n2 film, and (b) NDA-n1 film as organic semiconductor layer and SiO_2 as gate dielectric. All measurements were carried out at ambient condition. The data shown are taken in ascending V_G mode with an integration time of 1 s by averaging 5 points.

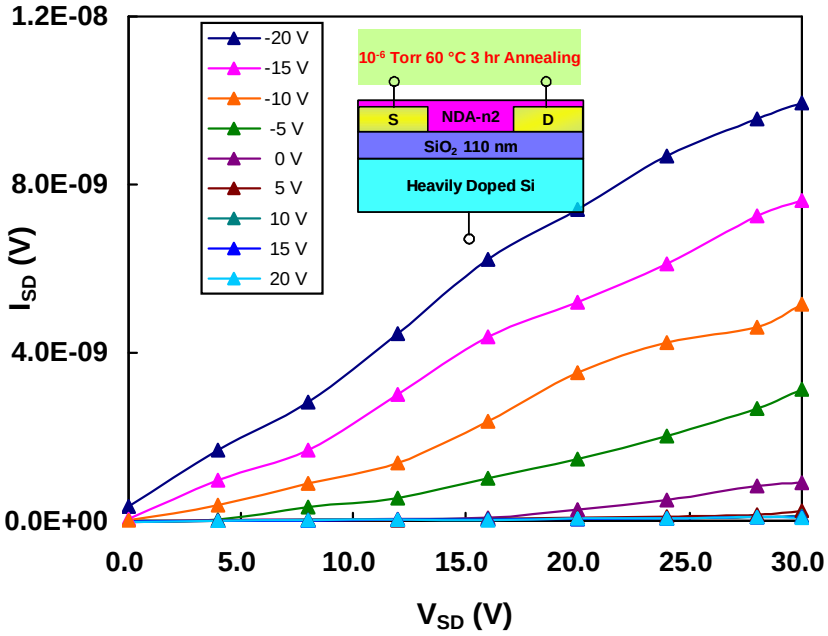

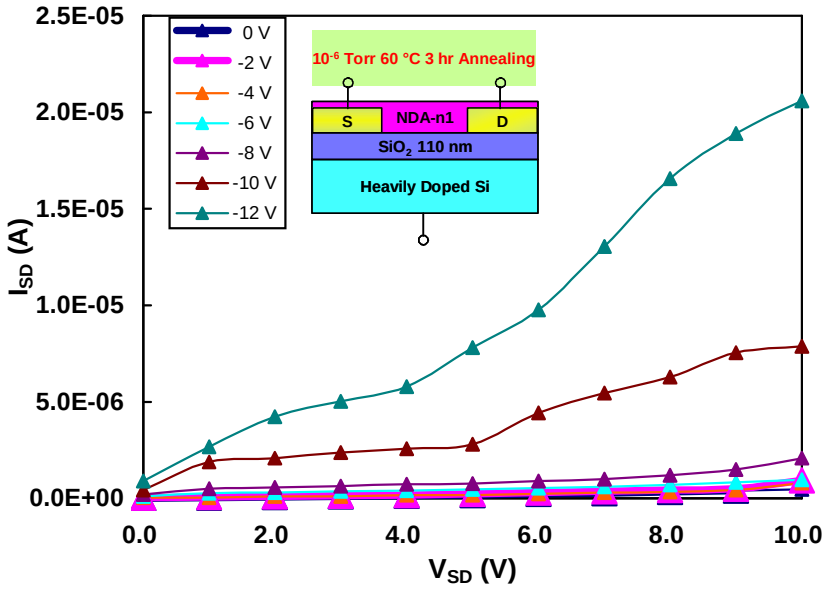

Figure 5.5 Transfer characteristics for device with (a) NDA-n2 film, and (b) NDA-n1 film as organic semiconductor layer and SiO_2 as gate dielectric after 10-6 Torr 60 °C 3 hr annealing.

5.3.2 Top-Contact Versus Bottom-Contact OTFT's

In chapter 3, we have discussed details of common configurations of OTFT's: top-contact and bottom-contact. Their structures are shown in Figure 5.2a and b, respectively. The difference in configuration is whether the drain and source electrodes are on the top or bottom of the organic seimiconductor film layer. And a key difference during operation is that there is a greater distance for charge carrier transport and thus a larger resistance for top-contact structure. There are also some literature reports on this issue. For example, Katz[4] report that top-contact would be superior to bottom-contact design. Therefore it is important to determine which configuration should be used for our NDA's films. The transfer characteristics for bottom-contact OTFT based on NDA-n1 has been shown in Figure 5.4b (as-deposited) and Figure 5.5b (after annealing at 10^{-6} Torr 80 °C for 3 hr). The corresponding results for top-contact OTFT are shown in Figure 5.6a and b, respectively. Since there were different SiO_2 gate dielectric film thichknesses (110 nm for bottom contact and 30 nm for top contact), the current I_{SD} cannot be directly used to compare the device performance. The carrier mobilities were calculated using Equation 5.1 and compared in Table 5.2.

Table 5.2 Mobilities for NDA-n1 based OTFT with bottom and top contact structure

	Mobility ($cm^2V^{-1}s^{-1}$)	
	As-deposited	Annealed
Bottom contact	2×10^{-3}	1×10^{-2}
Top Contact	8×10^{-4}	2×10^{-3}

For the as-deposited NDA-n1 OTFT, the mobility was 10^{-3} $cm^2V^{-1}s^{-1}$ for bottom-contact and 8×10^{-4} $cm^2V^{-1}s^{-1}$ for top-contact. After annealing the mobility improved to 10^{-2} $cm^2V^{-1}s^{-1}$ and 2×10^{-3} $cm^2V^{-1}s^{-1}$, for bottom and top contact devices, respectively. Before annealing, there was no significant difference between the two configurations, which because of the path differences for carriers is not easily explained. However after annealing a significant mobility improvement was found for bottom-contact while top-contact remained almost unchanged. One possible explanation can be attributed to the gold evaporation that causes heating of the sample as the heat of condensation is released. For the top-contact samples the heating due to Au deposition occurs on top of the NDA film while for the bottom-contact structure the Au is deposited before spin casting the NDA film. Thus the NDA-n1 film might already be annealed during the gold deposition. This annealing enhancement can compensate for the longer charge transport distance for top-contact OTFTs and re-annealing does not further improve the performance. In our study the mobility for bottom-contact after annealing was one order of magnitude higher compared with the top-contact.

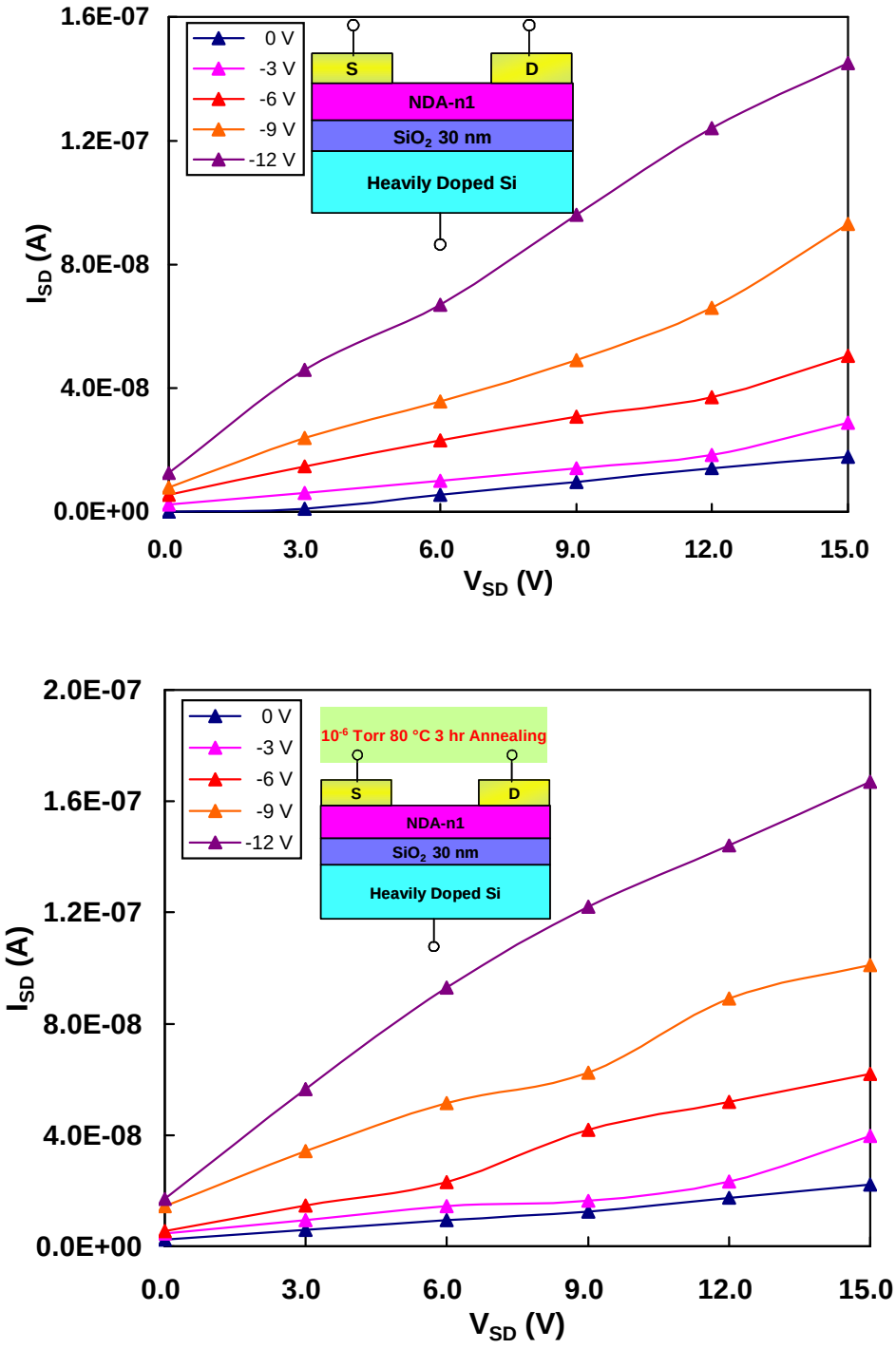

Figure 5.6 Transfer characteristics for top contact OTFT based on NDA-n1 as organic semiconductor layer and SiO_2 as gate dielectric (a) as-deposit, and (b) after 10^{-6} Torr 80 °C 3 hr annealing.

5.3.3 Effect of Thermal Annealing

As already discussed, annealing significantly improved OTFT's performance. Thermal annealing at moderately high temperature and vacuum helps remove moisture, solvent, and other smaller molecules trapped in the film during the spin casting process, and also prevent oxidation of the film during the process. Moderate heating also provides energy for molecular relaxation and reorganization to a thermodynamically stable state thus improving molecular alignment and ordering.[1] This process could reduce the density of trap sites and eliminate deep traps from the system resulting in improved mobility of the OTFT. In order to further understand this phenomenon and thermal stability of the NDA's film, thermo-gravimetric analysis (TGA) was carried out. A typical TGA thermograph of weight loss versus time for the NDA-n1 film obtained in our investigation is shown in Figure 5.7. In the TGA curve, an initial gradual weight loss of 4-5 % observed at 70 - 150 °C can be explained by the loss of moisture and solvents (dichloromethane) present in the film. A sharper decline in weight is observed at temperatures above 250 °C indicating deterioration of the sample. Compared with the original compounds, the meta-substituted aryl-ether flexible tails are likely disrupting the intra-molecular packing order as was previously reported[12], while the relatively high temperature helped the molecules pack more efficiently. The vacuum chamber with *in-situ* rotating analyzer ellipsometer (Figure 5.3) as described in Chapter 2 was used to observe a gradual change in optical properties and film thickness of NDA-n1 on native SiO_2 substrates. Figure 5.9a shows the decreasing film thickness of NDA at various annealing temperature settings. During spin casting of NDA film, shearing forces can disentangle the molecular chains and orient them in patterns that may not be the most efficient for charge transport.[13] These twisting in the π-bonded phenyl rings is decreased

when the film is annealed at temperatures around 60-80 °C. The consequent alignment of the molecules results into a favorable thermodynamic equilibrium results in reduced thickness. This decrease in thickness is accompanied by the increase in refractive index of NDA-n1 as shown in Figure 5.8b, which confirms densification of the NDA-n1 films during annealing at moderate temperatures. The improvement in mobility after annealing is consistent with improvements expected from a hopping mechanism of charge transport in NDA-n1 films. The deep trapping sites are reduced and both deep and shallow traps sites are brought closer together by densification. In addition, the formation of "crystallites" or metallic islands of up to a few microns in size during annealing of organic semiconductors, which improves charge mobility, have also been reported by Dodabalapur et al.[14]

The moderate temperature annealing also improved device performance. However, if the temperature is too high, the organics might degrade. For example, NDA-n1 will decompose when temperature is higher than 250 °C. Even the temperature is not approaching the degradation temperature, there is still some unfavorable phenomena happening. The improved alignment of NDA-n1 films during the initial stages of annealing which improves the inter-chain hopping parameters is seen to reverse and is even detrimental to the field effect mobility at higher annealing temperatures. For example, annealing NDA-n1 film at temperature higher than 150 °C caused some small cracks in the film.

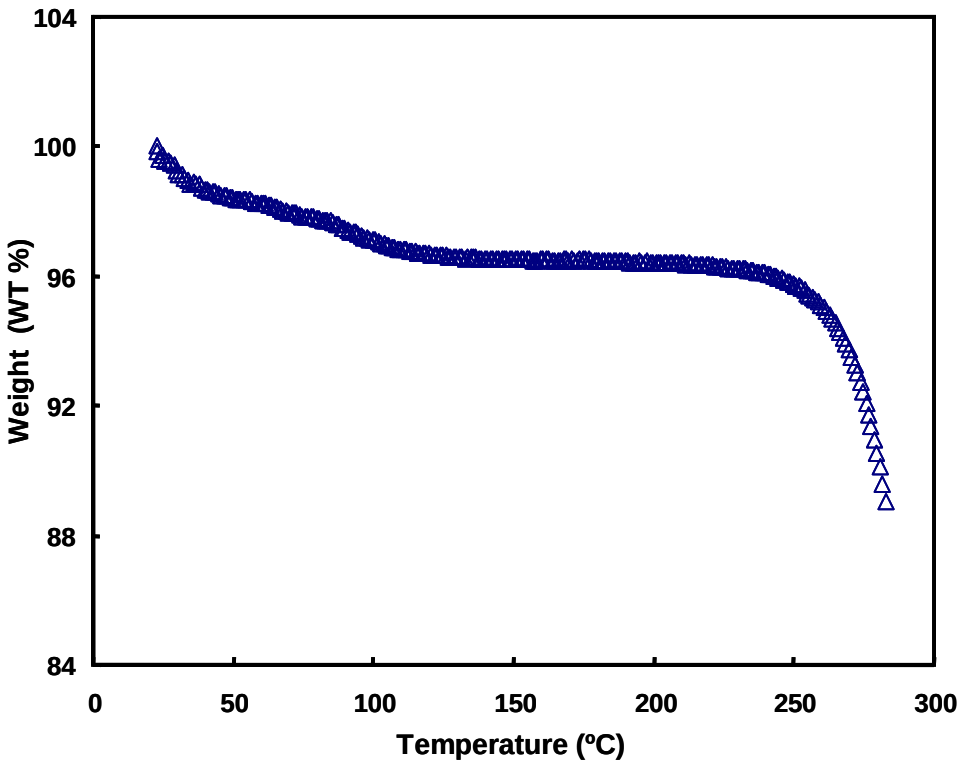

Figure 5.7 TGA Thermograph of NDA-n1 from 30-300 ºC at 10 ºC/minute.

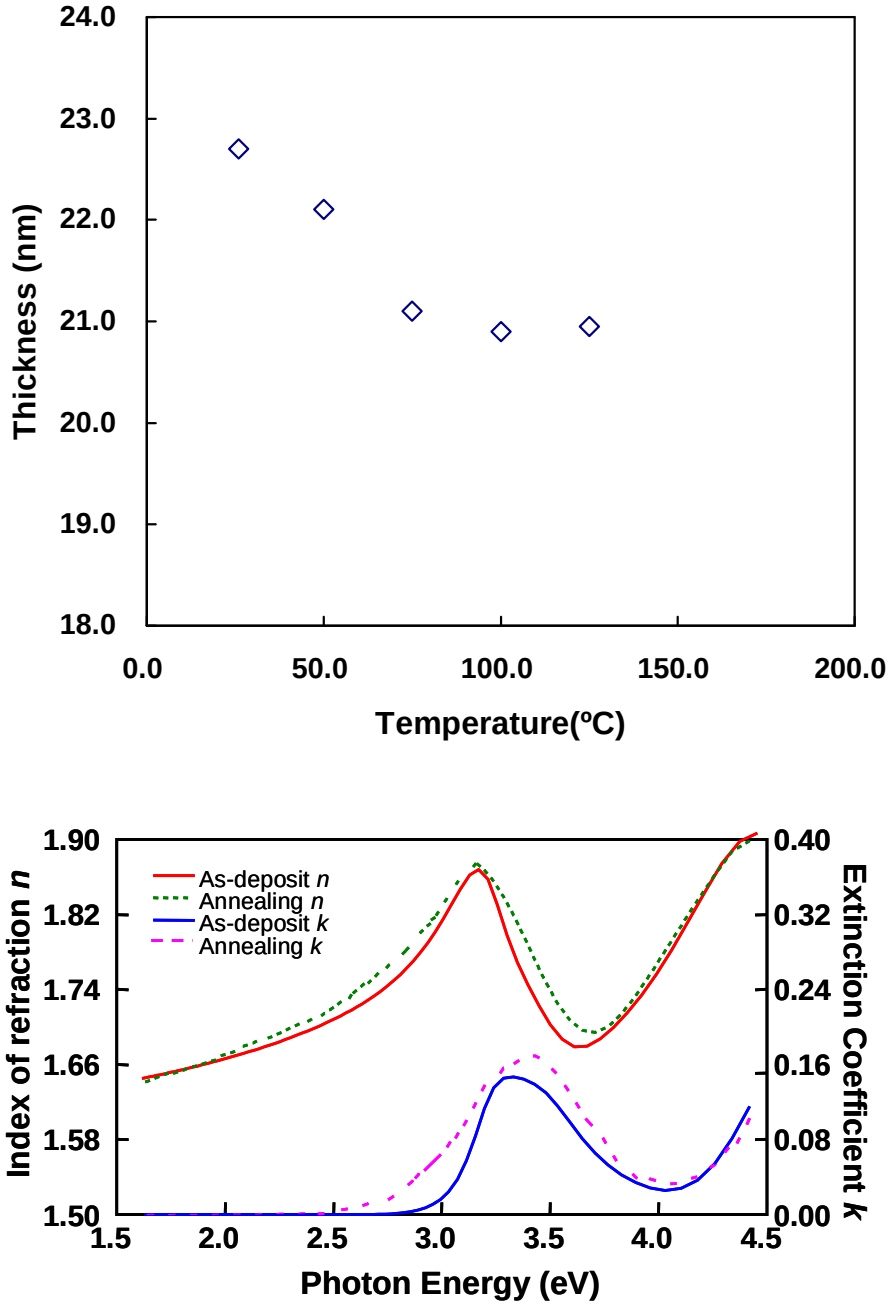

Figure 5.8 Densification of NDA-n1 film on SiO2 substrate under annealing (a) NDA-n1 film thickness obtained from in-situ SE, and (b) NDA-n1 refractive index where solid line is for as-deposit film and dashed line is for annealing at 100 ºC.

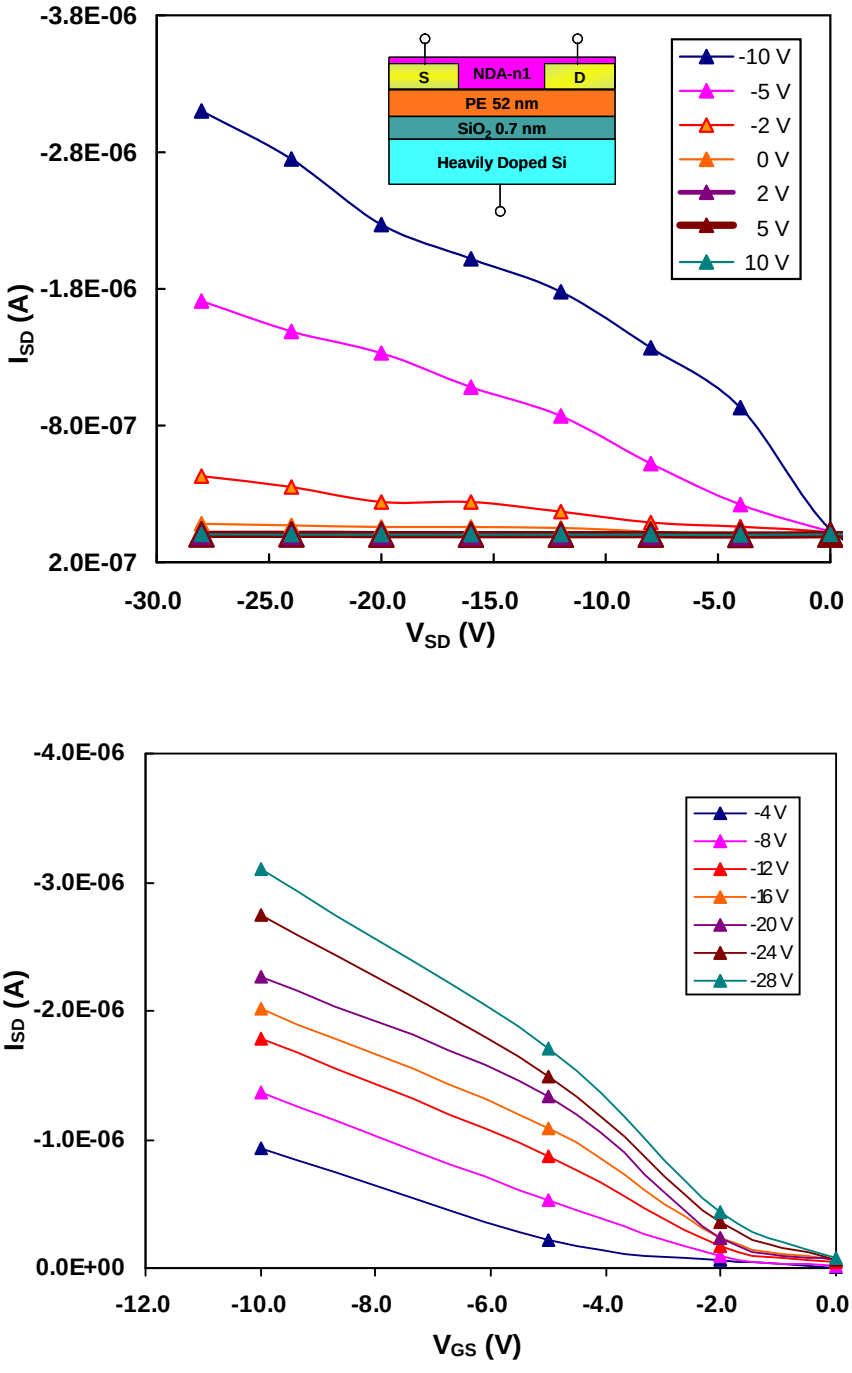

Figure 5.9 (a) Transfer and (b) turn on characteristics for NDA-n1 based OTFT using Polyethylene as gate dielectric. All measurements were carried out at ambient condition. The data shown are taken in ascending V_G mode with an integration time of 1 s by averaging 5 points.

5.3.4 Effect of Gate Dielectric Layer

The gate material which capacitively couples the active layer and the contact metal electrodes play a vital role in the performance of OTFT's. A dependable gate material should have low defect densities, a smooth surface and form sharp interfaces that facilitates good morphology of the subsequent active layer deposition. SiO_2 is frequently used as the gate dielectric in OTFT's. It is convenient to fabricate and is insoluble in organic solvents used for the deposition of organic semiconductor films. However, the silanol groups Si-OH present at the SiO_2 dielectric interface can quench electrons and formed a layer of immobile negative ions that compensates for the gate field.[6] It has been reported that surface treatment of gate dielectric with hexamethyldisilazene[15,16] or octadecyltrichloro-silane[17] improved carrier mobility for polymers with aliphatic side chains due to alignment of these chains on the non-polar substrate. It has also been reported that the polarity of dielectric interfaces is undesirable for OTFTs.[1] For all these reasons we chose alternate organic gate dielectrics to replace SiO_2 as the gate dielectric. The two dielectric candidates chosen for potential replacements for SiO_2 in OTFT's have dielectric constant, K on both sides of SiO_2 ($K = 3.9$) used in OTFT thus far. Medium density polyethylene (PE) with $K = 2.3$ was a low-K, non-polar candidate, and a copolymer of vinylidene fluoride with trifluoroethylene (PVDF-TrFE), a polar organic copolymer with $K = 7.5$, was a high-K candidate for the OTFT fabrication. Smooth interfaces were achieved that was favorable for the formation of highly conductive layers at the interface between dielectric and NDA-n1. The transfer and turn on characteristics for OTFT's fabricated with PE gate dielectric are given in Figures 5.10a and b, while those for P(VDF-TrFE) are given in Figure 5.10a and b, respectively. The carrier mobilities in the linear region were calculated and compared in Table 5.3.

Table 5.3 Mobilities of NDA-n1 based OTFT with different dielectrics

Dielectrics	PE	SiO_2	P(VDF-TrFE)
Dielectric Constant K	2.3	3.9	7.5
Mobility ($cm^2V^{-1}s^{-1}$)	5×10^{-2}	2×10^{-3}	10^{-4}

The highest mobility was 7×10^{-2} $cm^2V^{-1}s^{-1}$ for NDA-n1/PE OTFT, while for NDA-n1/P(VDF-TrFE) OTFT, the mobility was an order of magnitude lower than the mobility for the OTFT with SiO_2 in between, which is in agreement with the findings of Veres *et al.* who have also reported improvement in charge carrier mobility when a non-polar, low-K gate insulator ($K < 3$) was used instead of SiO_2. Thus the choice of gate dielectric is a major factor in OTFT performance with two factors to consider, the K value or polarity and the surface states attributed to the gate dielectric.

When exploring an organic substitute for SiO_2 gate dielectric, a high capacitance dielectric is normally desirable, as it reduces the operating voltage required to turn the device on. P(VDF-TrFE) with K value of 7.5 was chosen for this reason. It has been reported[18] that the polarity of the dielectric interface can affect the local morphology and the distribution of electronic states in the active layer. The hopping sites in organic semiconductors can be considered localized in an amorphous solid. Therefore, the local variation in dipole orientation due to polar high-K dielectric layer can cause energetic disorder and create localized sites making charge transport difficult as demonstrated in Figure 5.11.[19] This presence of increased trapping sites at the interface has been investigated by many workers, who have reported higher temperature activation requirement for charges to hop between the trap sites when polar high-K dielectric layers were used.[18,19]

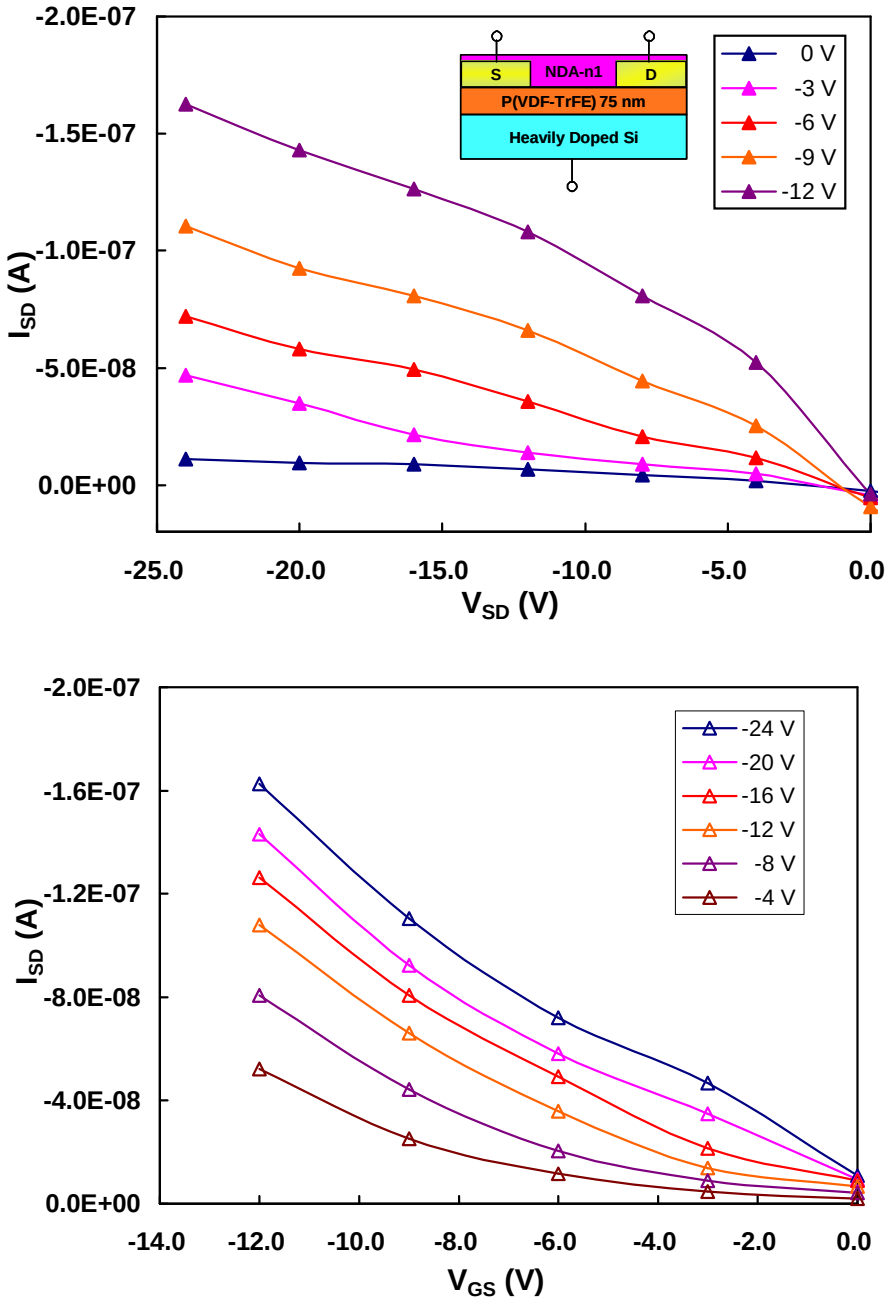

Figure 5.10 (a) Transfer and (b) turn on characteristics for NDA-n1 based OTFT using P(VDF-TrFE) as gate dielectric. All measurements were carried out at ambient condition. The data shown are taken in ascending V_G mode with an integration time of 1 s by averaging 5 points.

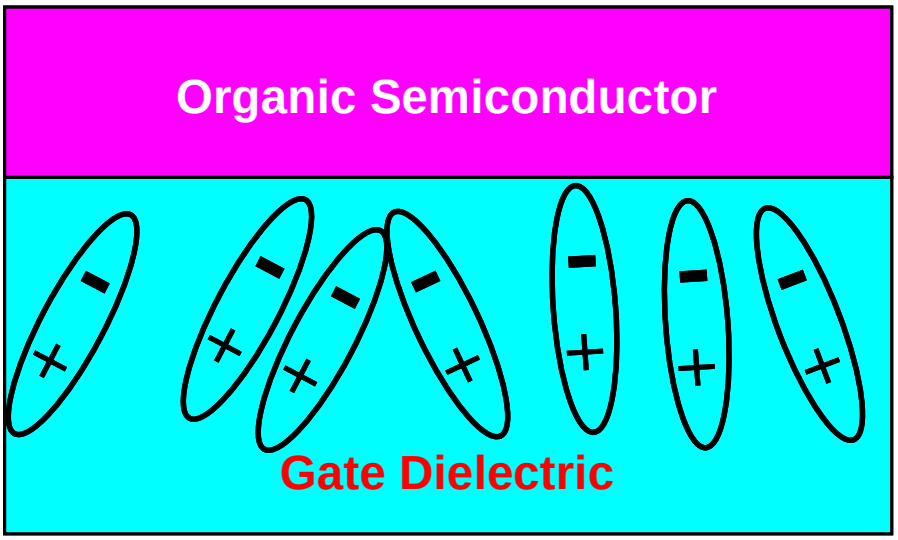

Figure 5.11 The energy disorder at the interface that may lead to an increase of local polarization.

Even though PE dielectric layer has a lower K, the decrease in gate capacitance from low-K dielectric is offset by the increase in mobility. It must be noted that not all low-K insulators (with $K = 2.1 - 2.3$) provide the advantages seen for PE and few other insulating materials. Some porous low-*K* insulating materials containing hydroxyl, acrylate, or ester functional groups are found to be not as effective.[18]

In order to assess the implementation of the best processes on the overall mobility, a combination of the PE gate dielectric and post annealing was used. The aforementioned OTFT based on PE was annealed in 10^{-6} Torr at 80 ºC for 3 hr. The transfer characteristic is shown in Figure 5.12. The calculated mobility is 9×10^{-2} $cm^2V^{-1}s^{-1}$. There is about 2-fold of magnitudes improvement that indicates the enhancement effects of the best processes are not cumulative.

5.4 Conclusions

A detailed study of new P-channel organic semiconductors, NDA-n1 and NDA-n2 is presented. The P-channel conduction comes from the flexible ether-aryl tail group. Temperature dependent studies show that a small densification and molecular re-ordering happened during annealing. The device performance strongly depends on the choice of gate dielectric. Low dielectric constant and the roughness of the interface between the dielectric and organic semiconductor deeply affect the charge carrier mobility. The mutual effects of gate dielectric and post annealing is helpful though it's not linearly combination of separate facts.

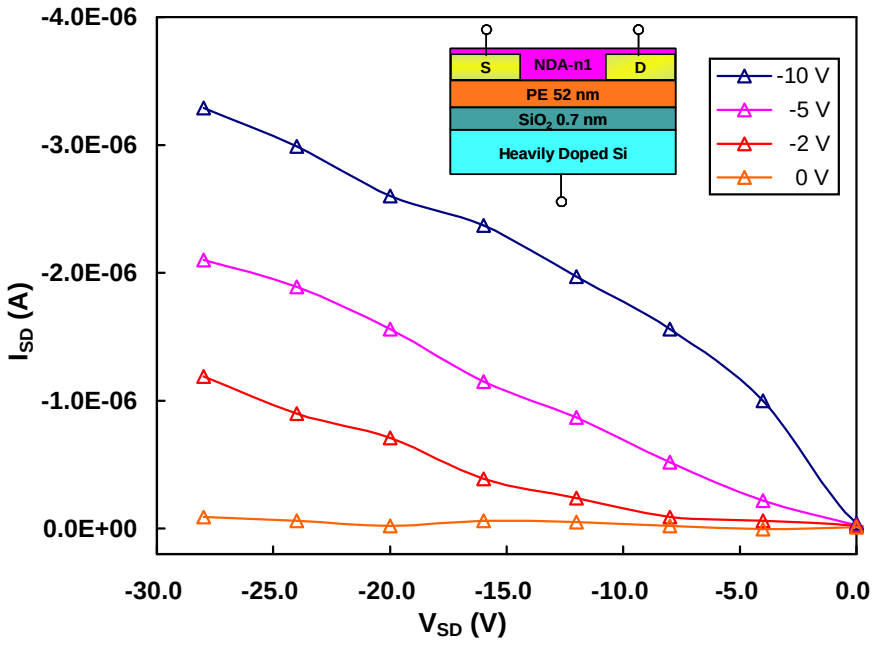

Figure 5.12 Transfer characteristics for NDA-n1 based OTFT using Polyethylene as gate dielectric after 10^{-6} Torr 80 ºC 3 hr annealing. All measurements were carried out at ambient condition. The data shown are taken in ascending V_G mode with an integration time of 1 s by averaging 5 points.

5.5 References

1. G. Horowitz, Adv. Mater. **10** (5), 365 (1998).

2. J.H. Schon, Syn. Met. **122** (1), 157 (2001).

3. P.G.L. Comber, W.E. Spear, Phys. Rev. Lett., **25** (8), 509 (1970)

4. H.E. Katz, A.J. Lovinger, J. Johnson, C. Kloc, T. Siegrist, W. Li, Y.-Y. Lin, A. Dodabalapur, Nature, **404**, 478 (2000).

5. M. Shtein, J. Mapel, J.B. Benziger, S.R. Forrest, Appl. Phys. Lett. **81**, 268 (2002).

6. L.-L. Chua, J. Zaumsell, J. Chang, E.C.-W. Ou, P.K.-H. Ho, E. Sirringhaus, R.H. Friend, Nature, **434**, 194 (2005).

7. F. Dinelli, M. Murgia, P. Levy, M. Cavallini, F. Biscarini, D.M. de Leeuw, Phys. Rev. Lett. **92**, 116802 (2004).

8. W. Michaelis, d. Wöhrle, D. Schlettwein, J. Mater. Res. **19**, 2040 (2004).

9. S. Wolf, R.N. Tauber, *Silicon Processing for the VLSI Era*, (Lattice Press, Sunset Beach, CA, 1990).

10. D. Yang, R.P. Shrestha, T.J. Dingemans, E.T. Samulski, E.A. Irene, Thin Solid Films, In press, (2006).

11. C.D. Dimitrakopoulos, D.J. Mascaro, *IBM J. Res. & Dev.* **45** (1), 11 (2001).

12. T.J. Dingemans, T.L. StClair, E.T. Samulski, NASA ICASE Report (Hampton, VA, 2002).

13. P. Monkman, T.M. Aminabhavi, Introduction to Macromolecular Science (Wiley: New York, 2002)

14. A. Dodabalapur, H.E. Katz, L. Torsi, R.C. Haddon, Science **269** (5230), 1560 (1995).

15. H. Sirringhaus, N. Tessler, R.H. Friend, Science, **280**, 1741 (1998).

16. H. Sirringhaus, P.J. Brown, R.H. Friend, M.M. Nielsen, K. Bechgaard, B.M.W. Langevle-Voss, A.J.H. Spiering, R.A. Janssen, E.W. Meijer, P.T. Herwig, D.M. de Leeuw, Nature, **401**, 685 (1999).

17. J. Collet, O. Tharaud, C. Legrand, A. Chapoton, d. Vuillaume, Mat. Res. Soc. Symp. Proc. **488**, 407 (1998).

18. J. Veres, S.D. Ogier, S.W. Leeming, D.C. Cupertino, S.M. Khaffaf, Advan. Funct. Mater.**13** (3), 199 (2003).

19. J. Veres, S.D. Ogier, G. Lloyd, D. de Leeuw, Chem. Mater., **16** (23), 4543 (2004).

CHAPTER 6 - CONCLUSIONS AND FUTURE DIRECTIONS

6.1 Summary of Results

In this study, the optical and electronic properties of new organic semiconductors, NDA's were characterized and their use to fabricate OTFT's has been investigated. A high vacuum system equipped with a heater and an in-situ RAE was built to monitor the annealing process in real-time. The RAE was assembled at our lab and was automated for data collection with the written software in LabVIEW™. The electronic performance of fabricated OTFT's was measured by a custom-built probe station using assembly of HP 4284A and Keithley 236.

The ellipsometric techniques were discussed in Chapter 2. We began with the nature of polarized light and its matrix representation, then discussed the interaction of polarized light with optical components used for ellipsometer, and finally we talked about details of data collection and extraction of materials properties in ellipsometry. Chapter 3 described the configurations of OTFT's and the charge transport in organic semiconducting films and devices. The organic semiconductors can be small monomeric molecules such as pentacene and anthracene, or large macromolecules such as polyacetylene or poly(o-methoxyanline). The current used charge transport mechanisms were discussed in detail. With exceptions to few organic semiconductors such as pentacene at very low temperatures, the band-like

transport of charges which results in high mobility is rarely seen in amorphous organic semiconductors. More commonly charge transport in organic semiconductors is the hopping and multiple trapping and release. Generic transfer and turn-on characteristic plots obtained during the electrical measurement of an OTFT were presented where the slope of the turn-on characteristics was used to calculate the field effect mobility of OTFT's.

The optical properties of NDA's films on silicon and thermally oxidized SiO_2 substrates were investigated in Chapter 4. An optical model for both NDA-n2 and NDA-n1 was developed respectively that was necessary interpret the ellipsometric measurements in terms of film optical properties and thickness. Furthermore, the optical properties helped gain preliminary insight into the electronic properties of NDA's. In addition to the ellipsometry, various complimentary techniques such as UV-Vis spectroscopy and AFM were used to improve the ellipsometric model and reduce correlation between the parameters being varied during the regression analysis.

Starting from a simple assumption of a Cauchy model, the optical model was developed in complexity to a combination of Tauc-Lorentzizan and Gaussian oscillators to incorporate the absorption peaks observed in the UV-Vis spectra. The film optical anisotropy was detected by rotating the sample around optical axis and variable incidence angle SE. No optical anisotropy was found, indicating no molecular arrange pattern for the spin-cast NDA's film. The roughness information obtained from AFM was incorporated into a BEMA model and obtained insignificant improvement to the model, which indicated surface roughness was very minor to affect the film properties. This will be crucial for the subsequent OTFT fabrication.

With an understanding of the optical properties, NDA's based OTFT's were prepared using different gate dielectrics—SiO_2, PE, and P(VDF-TrFE)—each having a different static dielectric constant—K = 3.9, 2.3, and 7.5, respectively. It was found that the dominant carrier transport was via holes, which resulted in P-Channel OTFT's and was opposite to the previously reported organics with similar conjugated functional group. This deviation was thought to be from the additional aryl-ether groups. The bottom-contact design was proved to help the charge transport in organic films. The post-fabrication annealing studies revealed rapid degradation of NDA's above 150 ºC and was confirmed by TGA thermograph. The annealing at lower temperatures increased the film density and improved the mobility by one order of magnitude, while high temperature annealing was harmful. Low dielectric constant non-polar dielectrics also improved the NDA's based OTFT's mobility by one order of magnitude, though the performance improvement of the combination of annealing and non-polar dielectric was not linearly proportional. These findings are described in Chapter 5.

6.2 Future Directions

OTFT has shown promise in the filed of electronics where light weight, large area and flexible electronics are desirable. In this study, a gradual shift from SiO_2 dielectric to an organic dielectric has been made and heavily doped silicon was primarily used as a substrate/gate conductor. NDA's was initially thought as N-channel semiconductor though results showed the opposite that the NDA's yield P-channel OTFT's.

The optical properties of the spin cast films on NDA's showed slight variation with the change in preparation condition and the underlying substrate. Therefore, a detailed study on optical properties is required when changing preparation conditions as well as the substrates.

Detailed studies of the effect of the morphology of the dielectric and the semiconductor layer on mobility needs further research. The interface between the gold electrode contacts and NDA's, charge injection into the semiconductor from the electrodes are essential in gaining a better understanding of OTFT performance. These details along with study in OTFT's fabricated with piezoelectric and ferroelectric P(VDF-TrFE) dielectric layer will be the future steps of this study.